Science and Technology of a Low-Energy Solar Neutrino Spectrometer (LENS) And Development of the MiniLENS Underground Prototype

Steven Derek Rountree

Dissertation submitted to the Faculty of the
Virginia Polytechnic Institute and State University
in partial fulfillment of the requirement for the degree of

Doctor of Philosophy
in
Physics

Ramaswamy Raghavan, Chair
R. Bruce Vogelaar
Mark Pitt
Leo Piilonen
Tatsu Takeuchi

April 21, 2009
Blacksburg, Virginia

neutrino physics, LENS, scintillation lattice, metal loaded liquid scintillator, Borexino, calibration, radiation

Science and Technology of a Low-Energy Solar Neutrino Spectrometer (LENS) And Development of the MiniLENS Underground Prototype

Steven Derek Rountree

(Abstract)

A real time low energy spectral measurement of the neutrinos coming from the Sun will give us a greater understanding of energy production in the Sun, and the mechanisms of neutrino mixing. We will, for the first time, measure the solar neutrino spectrum for all solar neutrinos <2MeV in particular pp, Be and CNO neutrinos, be able to compare the solar photon derived energy luminosity (L_γ) to the solar neutrino derived energy luminosity (L_ν) independent of any solar model, explore dark energy with respect to mass varying neutrinos, and explore CNO abundances in the Sun. These measurements require new technology in Indium loaded scintillators and large scale detector designs, namely increased spatial resolution through a novel scintillation lattice. I will present the advances we are making to these fields at Virginia Tech as well as neutrino science and the physics of the LENS detector.

Preface

The Sun is one of the best sources for studying neutrinos. It is a flavor pure ν_e source, with a higher flux (6.1 x 10^{14} pp-$\nu/m^2/s$ at the earth [(1)]), larger matter density (solar core density = $150 g/cm^3$ [(2)]), longer base line (mean 149.6 x 10^6 km [(3)]), and lower energy (0 keV to ~18 MeV) than any terrestrial source used so far for ν science in general. These factors make the Sun an excellent source for studying neutrino phenomena and astrophysics. The LENS experiment will take advantage of the charge-current (CC) capture of an electron neutrino on ^{115}In to measure the neutrino spectrum from the Sun with a threshold of 115 keV. [(4)] LENS is unique since it is the only low energy neutrino experiment capable of CC detection in real time so far. The LENS ν_e capture reaction is sensitive to ~95% of the solar neutrino flux. The precision measurement of the solar neutrino spectrum will allow us to compare solar photon derived energy luminosity (L_γ) to solar neutrino derived energy luminosity (L_ν). If $L_\nu / L_\gamma \neq 1.00$ then we must revaluate our current understanding of ν–particle physics, and astrophysics. The plan of this thesis is as follows.

Chapter 1: Neutrino Physics and History will discuss how the neutrino hypothesis came about and the later discovery of the neutrino. Then the Standard Solar Model (SSM), the solar neutrino problem, neutrino flavor oscillation, and neutrino mass discovery will be presented. The chapter will conclude by introducing open questions left in neutrino physics.

Chapter 2: The Low Energy Solar Neutrino Spectrometer (LENS) and Scientific Objectives will give an overview of the LENS detector. This will include discussions on neutrino charged-current capture on ^{115}Indium, ν-capture cross-sections for ^{115}In, and the scientific goals of the experiment.

Chapter 3: Metal Loaded Organic Liquid Scintillator (MLLS) Technology will begin with an introduction to Metal-loaded Liquid Scintillator MLLS technology and those experiments that will be using such technology in the near future. Then the details of LENS MLLS synthesis will be discussed: the quality control criteria of raw materials, front end purification, the main synthesis stages (neutralization and liquid-liquid extraction), MLLS analysis, and possible post synthesis purification / cleaning schemes. Concluding this chapter will be the current status and future development of the LENS MLLS.

Chapter 4: Scintillation Lattice (SL) discusses the scintillation lattice technology being developed for LENS. This is a new technology for large volume detectors with significant improvements in spatial resolution compared to traditional time of flight techniques. The optics will be discussed in length as well as material selection for the lattice.

Chapter 5: Background Events discusses the internal Indium background and internal and external background from Uranium, Thorium, Potassium, and their daughter nuclei.

Chapter 6: Kimballton Underground Research Facility (KURF) presents the newly created (2007) underground laboratory, KURF, near Virginia Tech.

Chapter 7: MiniLENS presents the miniLENS prototype giving a brief overview of the detector and planned phases for the experiment followed by a more in depth discussion of neutrino like event detection, "proxy" events, possible in miniLENS and what we intend to learn from this smaller version of the LENS detector.

Acknowledgements:

I would like to thank my advisor Dr. Ramaswamy Raghavan Professor of physics and Director of the Institute for Particle, Nuclear & Astronomical Sciences at Virginia Tech, for his advice and guidance during my graduate education, and for allowing me take on roles with the LENS Collaboration above and beyond what a graduate student would normally be exposed to. I would also like to thank him for my exposure to the underground physics community by sending me to conferences and DUSEL meetings in Lead, SD. Also, I would like to thank Dr. R. Bruce Vogelaar Professor of physics at Virginia Tech, Project Director of the Kimballton Underground Research Facility near Virginia Tech, and leader of the initiative at Virginia Tech to compete in the DUSEL selection process and Dr. Mark Pitt Professor of physics at Virginia Tech, (both are LENS Collaborators at VT), for their invaluable time spent discussing and working with me on the LENS detector prototypes and for serving on my dissertation committee, and Dr. Vogelaar for allowing me to take a significant role in the development and management of the Kimballton Underground Research Facility (KURF) for the development of miniLENS, and work with the Borexino Calibration group. I thank Dr. Leo Piilonen Professor of physics at Virginia and Dr. Tatsu Takeuchi Associate Professor of physics and Associate Director of the Institute for Particle, Nuclear & Astronomical Sciences at Virginia Tech for serving on my dissertation committee.

The former LENS post-docs Dr. Christian Grieb and Dr. Zheng Chang were of great help when I started working with LENS, I am sorry we were not able to work together longer. Thanks to both of you.

I thank all the LENS Collaborators for their work to make LENS a thriving solar neutrino experiment, and the National Science Foundation for their financial support of LENS.

I would also like to thank all the undergraduates I had the pleasure of mentoring for various projects associated with LENS, Michael Foussekis, Samantha Cavanagh, Micah Eassa, Chris Tolpa, and Shane Seaman.

I would also like to thank those graduate students working with Borexino, whom I worked with side by side on Borexino calibrations, Dr. Steve Hardy, Matt Joyce, and Szymon Manecki.

I would also like to thank all the staff, faculty, and students in the Virginia Tech Physics Department. The community in the department is a great asset which has aided me to no end during my work at Virginia Tech.

Last but not least, I would like to express my deepest gratitude to my parents, Dr. Steven P. Rountree and Mrs. Diane Rountree, and to my sister, Dr. Cindy L. Rountree and her husband Dr. Laurent Van Brutzel, who have provided support throughout my education. They have been a great source of encouragement and inspiration. I would also like to thank my fiancée, Brandie Renee Lemmon, who has been a source of encouragement, support, and sanity for these last couple of years.

Table of Contents

Chapter 1: Neutrino Physics and History

1.1 Neutrino History

Today we know an atom's nucleus is composed of neutrons and protons (which are further composed of quarks); however, this was not always the case. At the beginning of the 20th century the dense positively charged nucleus was first discovered by Ernest Rutherford [5] opening a new and exciting field of physics, nuclear physics. The Rutherford model of the nucleus suggested that the nucleus is composed of protons along with proton-electron pairs (Note: the neutron had not been discovered at this time). The number of protons was determined by the nucleus's charge, and the number of proton electron pairs was determined by the mass of the nucleus. For example— the ^{6}Li nucleus was believed to contain 3 protons and 3 proton-electron pairs. As the fields of radiation physics and nuclear physics progressed (particularly the phenomenon of β-decay), the nuclear model consisting of protons and proton-electron pairs threatened two of the most prized laws in Physics, conservation of energy and conservation of momentum.

1.1.1 Beta decay problem

In 1913 James Chadwick observed a continuous energy spectrum for the electron emitted when a nucleus beta decays (emits an electron). [6] This had profound consequences for conservation of energy and momentum. If conservation of energy and momentum were correct then this two body decay, Figure 1, should emit a mono-energetic electron.

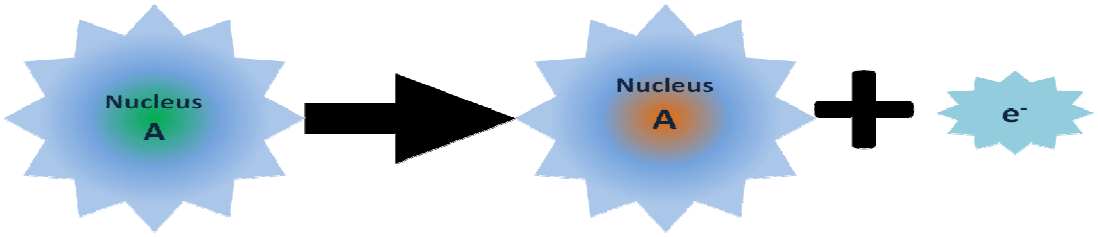

Figure 1 Understanding of Beta-decay at the beginning of the 20th century. Nucleus A emits an electron and becomes nucleus B.

In the following decade the property of particle spin was introduced, and it was found that protons and electrons both have spin ½. This raised yet another issue with the Rutherford model. A ^{14}N nucleus was found to have integer spin, [7] but according to the Rutherford model, the ^{14}N nucleus is comprised of 14 protons and 7 electrons, 21 spin ½ particles, and thus, per the Rutherford model, the net spin should be half integer.

The continuous beta decay energy spectrum was a crisis that threatened the bedrock of physics.

1.1.2 The neutrino hypothesis

Though some scientists, notably—Bohr, were beginning to suggest that energy may not be conserved on length scales of the atomic nucleus, this was too great a break for many physicists to accept!

In an effort to preserve conservation of energy in beta-decay, in 1930 Wolfgang Pauli postulated the "neutron" in a letter starting "Dear radioactive colleagues" at a meeting in Tübingen. [8] (Note, this "neutron" is not the neutron James Chadwick discovered later in 1932) Pauli suggested that there was a third particle in beta decay, later termed the neutrino by Enrico Fermi. Pauli's "neutron" was stated to have very little or no mass, spin ½, and no charge, making this particle very difficult to detect. The new particle thus explained all the presumed violations faced earlier. Pauli's postulate was not verified until 1956 when the (anti) neutrino *(at the time it was not realized that there was a difference between anti-neutrinos and neutrinos; therefore I use the nomenclature (anti) neutrino to allow for clarification)* was observed by Clyde Cowan and Frederick Reines via electron (anti) neutrino capture on ^{1}H [9] [10] [11]-- giving rise to Chadwick's neutron and a positron.

1.1.3 (Anti) neutrino discovery

The neutrino proved to be an elusive particle to detect. It went undetected for a quarter century until Cowan and Reines's neutrino experiment. Cowan and Reines built an (anti) neutrino detector at Hanford and reported results in 1953. The detection medium was organic liquid scintillator (OLS), toluene plus trace amounts of terphenyl and alpha-naptha-phenyloxazole, in which Cadmium propionate was dissolved [9] [10], and the source of (anti) neutrinos was a nuclear reactor, (anti) neutrino flux of ~ 5×10^{13} (anti)

neutrinos/cm^{2}s, much higher than any flux from radioactive sources. (Anti) neutrino capture on a ^{1}H nucleus of the OLS yields a neutron and a positron, according to the first reaction in Figure 2. The positron quickly annihilates with an electron, which results in the production of two 511 keV gammas. In the mean time the neutron thermalizes, diffuses, and moderates for several micro seconds and is then captured on Cd, emitting several gammas with total energy ~9MeV. The second reaction in Figure 2, provides a delayed coincidence reaction signature.

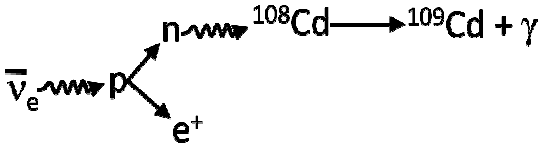

Figure 2 Cowan and Reines detection method. An anti-electron neutrino is captured on a proton producing a neutron and a positron. The positron is easily detected through electron positron annihilation, and the neutron is detected when it is captured on Cadmium-108 producing Camium-109 and a gamma ray.

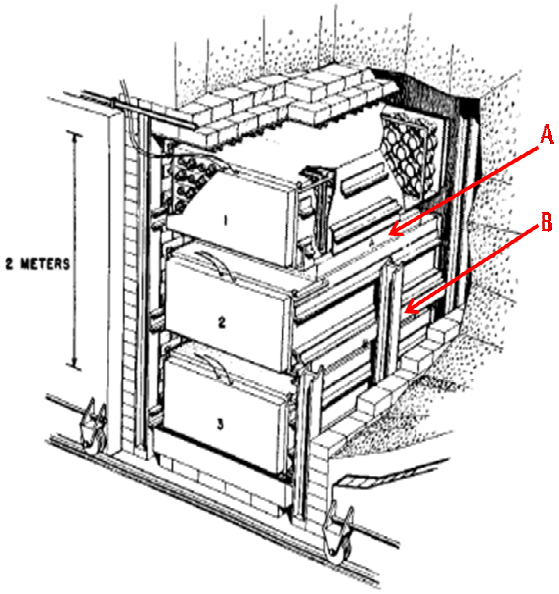

Figure 3 Cowan and Reines's Savannah River Experimental setup. Reprinted figure with permission from Fredrick Reines, Reviews of Modern Physics Volume 68 Issue 2 pg 322, 1996 http://rmp.aps.org/abstract/RMP/v68/i2/p317_1. (11)

They detected an excess of 0.41±0.20 counts/min compared to prediction ~0.5 counts/min (an effective cross section ~6×10^{-20} barns was used for this prediction); however, the signal to noise ratio in the experiment was 1:20. [9] Thus the Hanford experiment provided evidence for the existence of the (anti) neutrino; however, due to poor detection efficiencies and large uncertainties, the evidence for the existence of (anti) neutrinos was not yet conclusive. Cowan and Reines then modified their experiment. The subsequent experiment was conducted at the Savannah River Plant near Augusta, Ga. The experiment was 11m from the reactor core and 12m underground to provide shielding against cosmic rays. Two reaction water tanks were sandwiched between three OLS tanks – see Figure 3. Each end of each scintillator tank was outfitted with 55 PMTs. Cadmium chloride was added to the reaction water tanks. The reaction in this detector is the same as in the previous Hanford detector. The

differences in the Savannah River experiment were— the addition of a larger over burden allowing for larger reduction in μ flux and the signal 511 keV γ-rays for the positron annihilation must be detected in two OLS tanks adjacent to the water tank in which the neutrino capture occurred, and then the ~9MeV total energy from neutron capture on Cd must be detected in the same two OLS tanks. They measured an (anti) neutrino on proton capture cross-section of 6.3×10^{-44} cm^2 compared to the predicted value of 6×10^{-44} cm^2. [10] (Note: later when parity violation was discovered this predicted value was revised to about half this value thus making this initial value incorrect; however, the error was eventually traced to poorly understood systematic errors.) They published the results in 1956. Cowan died in 1974, but Reines was awarded the Noble Prize for the experiment in 1995. Cowan and Reines confirmed the existence of Pauli's "neutron", now tagged with the nomenclature "neutrino."

Cowan and Reines's discovery was the beginning of an exciting and rich era in experimental nuclear and particle physics continuing to this day.

1.1.4 Standard Solar Model

The Sun produces energy by nuclear fusion of four hydrogen nuclei into one helium nucleus, liberating ~25 MeV ($E=\Delta mc^2$) in the process. In 1920, Francis Aston discovered that four hydrogen atoms are heavier than a helium atom plus two electrons. [12] As a result, Sir Arthur Eddington concluded in the same year that the Sun produces energy by converting hydrogen into helium. [13] In 1928 George Gamow laid out the quantum mechanical ground work describing how two like charged particles can overcome the potential barrier between them and fuse. [13] And in 1938, Hans Bethe worked out the processes by which hydrogen is fused into heavier elements in stars, including the two major processes we believe today account for the energy production in the Sun, the pp-chain and CNO-cycle. [14]

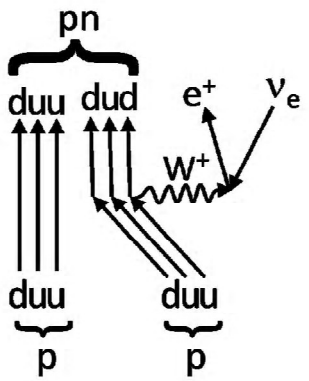

Figure 4: Proton-Proton Fusion Feynman Diagram. The fusions results in deuterium, a positron, and an electron type neutrino.

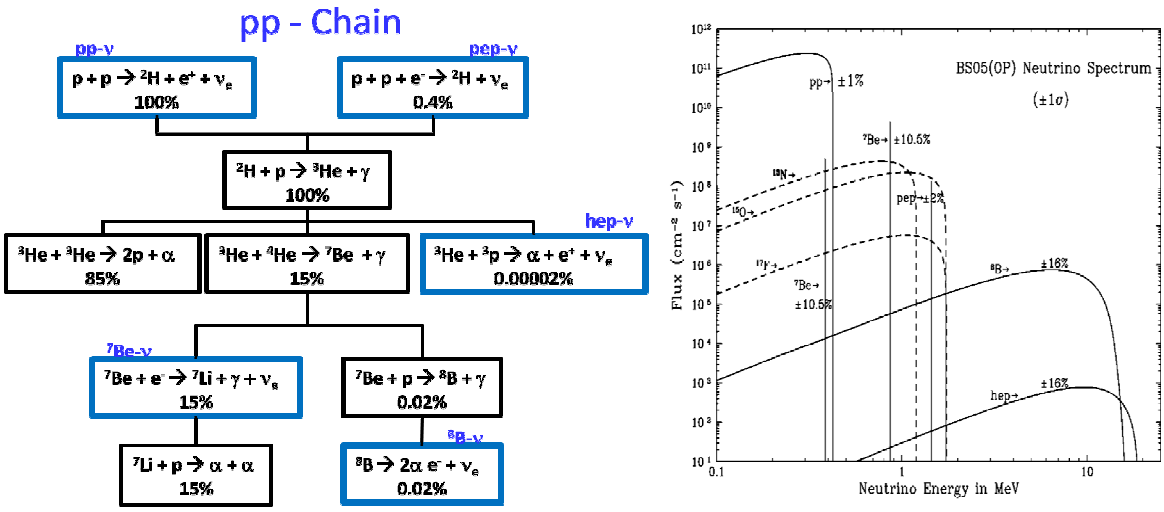

Figure 5 Left: pp – Chain of energy production in the Sun, with neutrino producing reactions highlighted in blue, and the name for that portion of the neutrino spectrum above the reaction. Right: Solar neutrino flux vs energy graph for those contributions from the pp-Chain— Reproduced by permission of the AAS from Reference **(15)**.

Solar models predict neutrino production in the Sun due to the fusion of light nuclei— p, ^{2}H, ^{3}He, ^{4}He, etc into heavier nuclei. [(15)] Figure 4 depicts the basic process for proton-proton fusion, $p + p \rightarrow d + e^+ + \nu_e$. One of the protons emits a W+ boson becoming a neutron which fuses with the other proton, while the W+ boson decays into a positron and an electron neutrino.

Figure 5 shows the pp-chain which is the chain by which pp fusion terminates in the creation of ^{4}He, beginning with protons (^{1}H nuclei). The percentages are the percentage of terminations in the pp-chain that include that particular reaction. Nearly 100% of the time this is two protons fusing to create a ^{2}H nuclei and a virtual W^+ boson. The virtual W^+ decays into a positron and a ν_e (pp-ν) pair— both have continuous energy spectrums up to the maximum available energy. Rarely, ~0.4% of the time, the reaction is the combination of two protons and an electron where a proton and electron combine through W^+ boson exchange resulting in a neutron that fuses with a proton. This reaction yields a ^{2}H nuclei and a ν_e (pep-ν). This ν_e is mono-energetic. The resulting ^{2}H can then combine with a proton yielding a ^{3}He nucleus and a gamma ray. From here, there are four branches in the chain all terminating with the creation of ^{4}He:

1) *pp I branch*— ~85% branching. In this branch two ^{3}He nuclei fuse yielding an alpha (^{4}He) and two protons.
2) *pp II branch*— ~15% branching. In this branch a ^{3}He and ^{4}He nucleus fuse yielding a ^{7}Be nucleus and a gamma ray. The ^{7}Be may then capture an electron, producing a ^{7}Li, ν_e (^{7}Be-ν), and gamma if ^{7}Li is produced in an excited state. The neutrino in this reaction is mono-energetic and created with one of two energies (0.861 MeV or 0.383 MeV) depending on whether ^{7}Li is produced in an excited state, or ground state. ^{7}Li may then capture a proton and produce two ^{4}He nuclei.
3) *pp III branch*— ~0.02% branching. This branch produces ^{7}Be in the same manner as the pp II branch. After ^{7}Be is produced it captures a proton yielding ^{8}B and a gamma. ^{8}B then fissions yielding two ^{4}He nuclei, an electron, and a ν_e (^{8}B-ν). As in proton-proton fusion, the electron and ν_e have continuous energy spectra.
4) *pp IV branch*— ~0.00002% branching. ^{3}He and a proton fuse yielding ^{4}He, a positron, and a ν_e (hep-ν). As in proton-proton fusion and ^{7}Li production, the positron and ν_e have continuous energy spectra.

In addition to the pp-chain, ^{12}C is created through the triple alpha process and feeds into the CNO cycle, $^{12}C \rightarrow {}^{13}N \rightarrow {}^{13}C \rightarrow {}^{14}N \rightarrow {}^{15}O \rightarrow {}^{15}N \rightarrow {}^{12}C$, Figure 6, producing ν_e's from the β^+-decay of ^{13}C and ^{15}N.

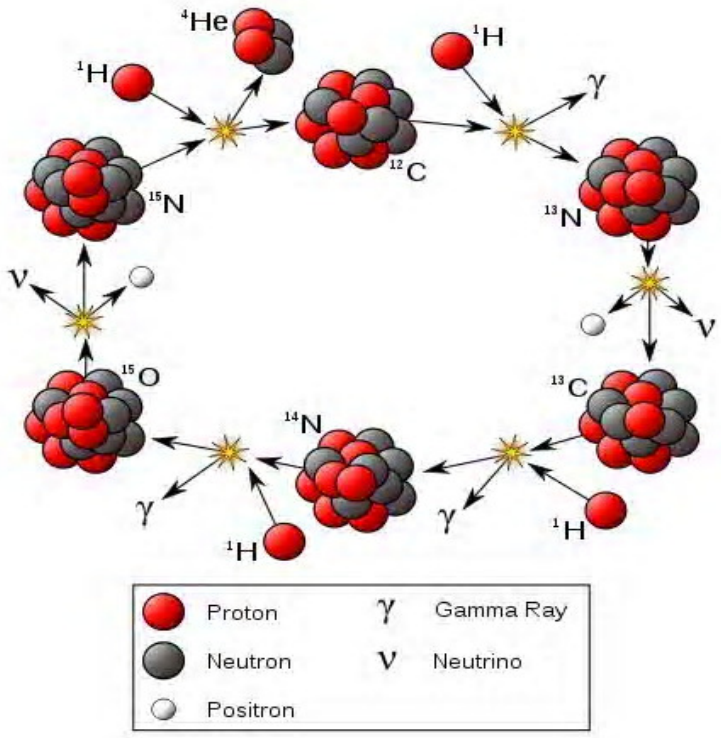

Figure 6 The CNO Cycle in the Standard Solar Model, the image was taken from **http://en.wikipedia.org/wiki/CNO_cycle**.

1.1.5 Detection of solar neutrinos

Raymond Davis Jr, after an endeavor to measure reactor neutrinos at Brookhaven National Laboratory and Savanna River using the inverse beta decay reaction:

$$\nu_e + {}^{37}Cl \rightarrow {}^{37}Ar + e^-,$$

suggested by Bruno Pontecorvo, [16] decided to attempt a solar neutrino measurement using the same detection method. Note, the reactor experiments detected no surplus of neutrinos with the reactors running versus the reactors being shut off due to the fact understood later that reactors produce antineutrinos not neutrinos. The distinction in the behavior of antineutrinos and neutrinos was still not known at this time, and in fact this work contributed to the conclusion that neutrinos and antineutrino are not identical. [10] In the late 1960's, Davis deployed a ~375000 L tank of perechloroethylene 4800 feet below the earth's surface at the Homestake gold mine in Leads, South Dakota, and began counting ^{37}Ar produced by neutrino capture on ^{37}Cl. The counting method was to allow the ^{37}Ar to accumulate and every few weeks extract the ^{37}Ar by bubbling the tank with

Helium and collecting the ^{37}Ar in a cold charcoal filter. After sample collection it is heated to remove chemically active compounds, and then Xe and Kr are removed through gas chromatography. Finally the sample is counted in a proportional counter. The ^{37}Ar produced in the detector was significantly less than expected, typically 1/3 the value expected from theoretical predictions by John Bahcall. [17] [18] As other experiments confirmed Davis's results and Bahcall's calculation were put through rigorous checks, this discrepancy would become known as The Solar Neutrino Problem.

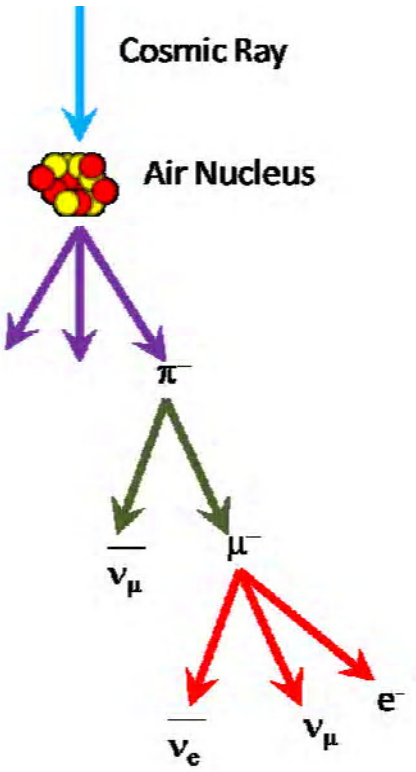

Figure 7 Atmospheric neutrino production. Cosmic rays incident on the upper atmosphere collide with nuclei producing pions, which decay into a muon, and an antimuon neutrino. The muon subsequently decays into an antielectron neutrino, a muon neutrino, and an electron

1.1.6 Oscillation hypothesis and discovery

In 1957, before Davis began counting solar neutrinos, Bruno Pontecorvo, suggested that neutrinos may oscillate, as an explanation to the signal deficit Davis observed in his reactor experiment. That is, he suggested neutrinos may oscillate between electron, muon, and tauon flavors. Equation 1 expresses the relationship between the flavor eigenstates and the mass eigenstates. Equation 2 shows the probability for oscillation over distance L with energy E. Note, if all the neutrino flavors have no mass, the sin term is zero and there is no flavor oscillation. See reference (19) for a full derivation of Equation 2 and more details on neutrino oscillation.

$$\left|\nu_\alpha\right\rangle = \sum U^*_{\alpha i}\left|\nu_i\right\rangle$$

$$\left|\nu_i\right\rangle = \sum_{\alpha}^{i} U_{\alpha i}\left|\nu_\alpha\right\rangle$$

Equation 1 Relation between mass and flavor eigenstates
where $\left|\nu_\alpha\right\rangle$ is the flavor eigenstate and $\left|\nu_i\right\rangle$ is the mass eigenstate.

$$P\left(|\nu_\alpha\rangle \rightarrow |\nu_\beta\rangle\right) = \quad \delta_{\alpha\beta} - 4\sum_{i>j} Re\left(U^\dagger_{\alpha i}U_{\beta i}U_{\alpha j}U^\dagger_{\beta j}\right)\sin^2\left(\frac{\Delta m^2_{ij}L}{4E}\right)$$

$$+\,\mathbf{2}\sum_{i>j} \boldsymbol{Im}\left(\boldsymbol{U^\dagger_{\alpha i}U_{\beta i}U_{\alpha j}U^\dagger_{\beta j}}\right)\mathbf{sin}\left(\frac{\boldsymbol{\Delta m^2_{ij}L}}{\mathbf{2E}}\right)$$

Equation 2 Neutrino oscillation probability. $\boldsymbol{\Delta m^2_{ij} = m^2_i - m^2_j}$

The unitary mixing matrix U is expressed in Equation 3 as a product of three unitary matrices corresponding to the mixing of the states. In analogy to rigid body rotations, the matrix elements are conveniently expressed as $c_{ij} = \cos\theta_{ij}$ and $s_{ij} = \sin\theta_{ij}$ where θ_{ij} are termed mixing angles. Herein, the phase factor δ is introduced to accommodate the possibility that the neutrino oscillation violates CP symmetry and α_1 and α_2 are the Majorana phases. This mixing matrix is referred to as the MNS matrix in analogy to the CKM matrix in quark mixing.

The first suspicion of neutrino oscillation was the deficit in Davis's experiment; however, not knowing whether the models of the Sun were correct, this experiment could not stand alone as conclusive evidence for neutrino oscillations. It was not until 1998 that neutrino oscillation was confirmed by the Super Kamiokande Experiment (Super K). Super K was able to measure an asymmetry in atmospheric ν_e:ν_μ ratio for those neutrinos traveling upward in the detector (having passed through the earth) versus those traveling downward.

$$U = \begin{bmatrix} U_{e1} & U_{e2} & U_{e3} \\ U_{\mu 1} & U_{\mu 2} & U_{\mu 3} \\ U_{\tau 1} & U_{\tau 2} & U_{\tau 3} \end{bmatrix}$$

$$= \begin{bmatrix} 1 & 0 & 0 \\ 0 & c_{23} & s_{23} \\ 0 & -s_{23} & c_{23} \end{bmatrix} \begin{bmatrix} c_{13} & 0 & s_{13}e^{-i\delta} \\ 0 & 1 & 0 \\ -s_{13}e^{i\delta} & 0 & c_{13} \end{bmatrix} \begin{bmatrix} c_{12} & s_{12} & 0 \\ -s_{12} & c_{12} & 0 \\ 0 & 0 & 1 \end{bmatrix} \begin{bmatrix} e^{i\alpha_1/2} & 0 & 0 \\ 0 & e^{i\alpha_{21}/2} & 0 \\ 0 & 0 & 1 \end{bmatrix}$$

$$= \begin{bmatrix} c_{12}c_{13} & s_{12}c_{13} & s_{13}e^{-i\delta} \\ -s_{12}c_{23} - c_{12}s_{23}s_{13}e^{i\delta} & c_{12}c_{23} - s_{12}s_{23}s_{13}e^{i\delta} & s_{23}c_{13} \\ s_{12}s_{23} - c_{12}c_{23}s_{13}e^{i\delta} & -c_{12}s_{23} - s_{12}c_{23}s_{13}e^{i\delta} & c_{23}c_{13} \end{bmatrix} \begin{bmatrix} e^{i\alpha_1/2} & 0 & 0 \\ 0 & e^{i\alpha_2/2} & 0 \\ 0 & 0 & 1 \end{bmatrix}$$

Equation 3 MNS Matrix $c_{ij}=\cos\theta_{ij}$ and $s_{ij}=\sin\theta_{ij}$

1.1.7 Solar Neutrino Problem Solved

In 2001 the Sudbury Neutrino Observatory (SNO) experiment released results solving the solar neutrino problem. [20] The SNO detector was sensitive to all three flavors of neutrino and was able to detect the number of neutrinos predicted in the SSM. This was done by having a large heavy water (D_2O) detector. All three neutrinos can interact with a deuterium nucleus through the neutral current interaction breaking the deuterium nucleus into its constituents and then continuing on with slightly less energy.

Nuclear NC:

$$\nu_x + d \rightarrow \nu_x + p + n$$

The neutron can then capture on D_2O and emit a 6MeV gamma ray which can be detected. All three neutrinos can also interact by scattering off of an atomic electron via a Z^0 boson and ν_e's can scatter via a $W^{\pm}$ boson as well.

Electron Scattering NC:

$$\nu_x + e \rightarrow \nu_x + e$$

Electron Scattering CC:

$$\nu_e + e \rightarrow \nu_e + e$$

These scattering interactions produce a Compton like energy spectrum as a signal and have directional sensitivity (analogous to billiards). Lastly, a solar electron neutrino can be captured on a neutron in a deuterium nuclei producing an electron between 5-15 MeV.

Nuclear CC:

$$\nu_e + d \rightarrow p + p + e^-$$

This interaction is not allowed for muon and tauon neutrinos due to solar neutrinos having insufficient energy to produce muons and tauons. SNO's solar flux measurements, $\varphi^{CC}(\nu_e) = 1.75\pm0.07\times10^6 cm^{-2}s^{-1}$ and $\varphi^{CC+NC}(\nu_x) = 5.44\pm0.99\times10^6 cm^{-2}s^{-1}$, concluded the "missing" solar neutrinos were oscillating on their way to earth, and the total number of neutrinos e, μ, and τ agrees with the SSM. [20]

1.2 The horizon of neutrino physics

The neutrino has been an elusive and mysterious particle, evading detection and baffling scientists for decades. Now that we have confirmed the neutrinos existence and solved the solar neutrino deficit problem, what lies ahead?

1.2.1 Precision measurement of the solar neutrino luminosity

Precision measurement of the solar neutrino luminosity, L_ν, is the next major endeavor in the field of solar neutrino physics. The Sun offers 1) the highest flux of pure ν_e on earth, 2) the highest matter density, 3) the longest baseline, and 4) lower ν energies compared to terrestrial sources. These properties make the Sun ideal for studying ν-flavor phenomena.

A low energy solar ν spectrum measurement offers unique access to direct experimental proof of the Mikheyev-Smirnov-Wolfenstein – Large Mixing Angle (MSW-LMA) effect for ν-flavor conversion. A final test of this model is very desirable. The basic test is the measurement of the flavor survival probability as a function of energy. This could reveal explicitly the presence of non standard interactions in particle physics. The measurement will allow for a precision test of the standard solar model (SSM) via a comparison of the solar ν luminosity, L_ν, to the precisely known photon luminosity, $L_¤$. Any inequality $L_\nu \neq L_¤$ that survives at high precision will have serious implications for our understanding of the Sun— e.g. reactions beyond the standard model, new sources of energy production in the Sun, or a flaw in neutrino oscillation physics. The precision measurement of the solar neutrino luminosity is covered in

greater detail in Chapter 2: The Low Energy Solar Neutrino Spectrometer (LENS) and Scientific Objectives.

1.2.2 Precision measurements of ν Mixing Parameters

As discussed in 1.1.6 Oscillation hypothesis and discovery, neutrinos oscillate as they travel. These oscillations are governed by the MNS mixing matrix which contains mixing parameters θ_{12}, θ_{13}, θ_{23}, δ, the three neutrino masses, and two Majorana phases. Neutrino to neutrino oscillations are only sensitive to:

1) The three mixing angles θ_{12}, θ_{13}, and θ_{23}
2) Two mass squared differences Δm^2_{12} and Δm^2_{31}, where $\Delta m^2_{ij} = m^2_i - m^2_j$
3) The CP-violating phase factor δ assuming $\theta_{13} \neq 0$

Neutrino to neutrino oscillations are not sensitive to the absolute neutrino mass, or the Majorana phases which only appears in lepton number violating processes, such as neutrinoless double β-decay. [21]

Solar neutrino experiments with KamLAND reactor neutrino experiments are sensitive to θ_{12} and Δm^2_{12}. These parameters are thus often referred to as θ_{sol} and Δm^2_{sol} respectively. Likewise, atmospheric neutrino and long baseline accelerator neutrino experiments have driven the precision of θ_{23} and Δm^2_{23}, and are thus often referred to as θ_{atm} and Δm^2_{atm} respectively.

The current parameter limits are:

1. $\theta_{13} < 10.3°$ [22]
2. $\theta_{12} = 33.9° \, ^{+2.4°}_{-2.2°}$ [23]
3. $\theta_{23} = 45° \, ^{+7°}_{-7°}$ [24]
4. $\Delta m^2_{21} = 8.0 \, ^{+0.6}_{-0.4} \times 10^{-5} eV^2$ [23]
5. $|\Delta m^2_{31}| \approx |\Delta m^2_{32}| = 2.4 \, ^{+0.6}_{-0.5} \times 10^{-3} eV^2$ [24]
6. The Majorana phases, CP violating phase factor, and the sign of $|\Delta m^2_{32}|$ have not yet been measured

Pushing the neutrino parameter limits is important for many theoretical models. For example, the measurement of θ_{13} directly impacts weather it is even possible to measure CP violation in the neutrino sector. If θ_{13} is very small then the CP violating term in the

MNS matrix becomes small, making a measurement of the CP-violating phase factor, δ, difficult.

1.2.3 Are there more than three neutrino flavors?

Studying the decay of the Z boson from Z boson production in e^+e^- collisions gives insight into the number of active light neutrinos, light being $m_\nu < m_Z/2$ and active meaning that the neutrino couples to the weak force carriers (Z^0,W^+, and W^-). The invisible width, Γ_{inv}, is determined by subtracting the observed partial widths for quarks and charged leptons from the total Z boson width. The resultant Γ_{inv} is assumed to be due to the number of active light neutrinos each contributing Γ_ν in accordance to the Standard Model of Particle Physics. The LEP result is: [25]

$$N_\nu = \frac{\Gamma_{inv}}{\Gamma_l}\left(\frac{\Gamma_l}{\Gamma_\nu}\right)_{SM} = 2.984 \pm 0.008$$

Equation 4 Number of active light neutrinos. [25]

Though the evidence is strong for there being no more than three active light neutrinos, there are possibilities for the existence of more than three neutrinos that do not interact with the weak force carriers; they are termed sterile neutrinos.

A problem of great interest in the physics community is the possibility of more than three neutrino flavors. [26] [27] [28] The LSND collaboration first observed what is considered a possible fourth neutrino flavor [26] in a measurement of $\bar{\nu}_\mu \rightarrow \bar{\nu}_e$ oscillations. Although the MiniBooNE experiment failed to confirm this measurement [27], theoretical interest in sterile neutrinos continues— light sterile neutrinos ($m_\nu \sim 1eV$) proposed as smaller mixing to the electron neutrino than claimed by LSND may fix problems in heavy element production in supernova [29]. Indeed it may be possible to search for active-sterile neutrino mixing in LENS using a radioactive source where the granularity of the LENS detector provides a unique advantage over other detectors. [30]

Chapter 2: The Low Energy Solar Neutrino Spectrometer (LENS) and Scientific Objectives

2.1 Introduction to LENS

Solar Neutrino research offers an ideal opportunity for major advances in the detailed understanding of the nature of the neutrino (ν). Compared to terrestrial ν production machines, the Sun offers higher source flux of pure ν_e's, a higher matter density to investigate matter enhanced effects on ν oscillations, a much longer baseline (the distance from production to detection), and lower ν energies—all ideal for studying ν-flavor phenomena. The low-energy spectrum from the Sun (<2 MeV) offers a palette of known fluxes with specific energies ideal for probing in detail ν-flavor physics via the energy dependence of ν-flavor survival. The low-energy solar ν spectrum offers unique access to direct experimental proof for completing the MSW-LMA ν-flavor conversion model, and probe new scenarios of non standard particle physics. This window allows for the opportunity of an overall precision test of ν physics and astrophysics using the fundamental equality of the derived solar ν luminosity, L_ν, to the precisely known photon derived luminosity, L_γ, of the Sun. [31] Any inequality in the two luminosities that survives at high precision has epochal implications. This objective requires the measurement of the complete set of neutrinos created in the Sun—pp, ^{7}Be, pep, and CNO ν fluxes, which generate >95% of the ν luminosity, clearly resolved into individual fluxes with minimal background uncertainty. Energy specific charge current (CC) based ν detection is essential for this purpose. This is the primary mission of the LENS collaboration.

Individual flux measurements, e.g. CNO cycle flux, are key to studying intrinsic importance in the present context of the "new solar neutrino problem" which asks "Are the light elements really depleted in the Sun?" The question was prompted by the recent analysis of atomic absorption data which has conflicts with heliosiesmology. [32] The high signal/background in the LENS CNO measurement is especially attractive. In comparison, other approaches that are based on the electron scattering method of ν

detection do not give sufficient discrimination against backgrounds from radioactive contaminants, nor do they give a one-to-one correspondence of ν energy to the observed electron.

The first real-time spectroscopy of solar ^{7}Be ν's by Borexino [33] is a breakthrough providing fresh impetus to the program of low-energy ν research. The CC+NC based Borexino result offer a key compliment to the LENS detector.

LENS is set to chart new directions in precision ν spectroscopy for ν physics. For the first time, the needed technology to accomplish these goals of low energy ν physics is available in, and only in, LENS.

The last decade of the LENS collaboration's research:

1) Fundamentally reinvented the concepts and strategies of the background suppression in LENS, dramatically enhancing prospects for the feasibility of LENS, Chapter 5: Background Events.
2) Research into In-loaded liquid scintillator (InLS), which is the basis of LENS, has culminated in robust chemical methods that have yielded InLS with extremely favorable properties, Chapter 3: Metal Loaded Organic Liquid Scintillator (MLLS) Technology.
3) A novel scintillation lattice (SL) technology was developed that achieves the basic granularity for more precise event localization and topology analysis than are achievable by conventional time of flight methods, Chapter 4: Scintillation Lattice (SL).
4) The combination of 1), 2), and 3) can be tested in a 15% length-scale prototype, miniLENS, which is in the initial phases of construction, Chapter 7: MiniLENS.

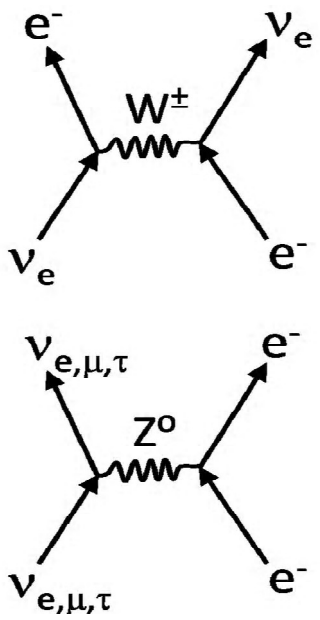

Figure 8 Neutrino-electron elastic scattering. Top a ν_e is able scatter off of an electron via $W^{\pm}$ exchange. Bottom all three flavors of neutrino are able to scatter off an electron via a Z^o boson.

2.2 Methods for ν Detection.

The two primary reactions for detecting neutrinos are 1) e-ν scattering and 2) ν-capture. In e-ν scattering a neutrino scatters off of an electron, transferring a portion of its energy to the electron (Compton like ν scattering). This can be done two ways 1) an incoming ν_e can exchange a $W^{\pm}$ with an electron or 2) all three flavors of neutrinos can exchange a Z^o with an electron. In both cases some energy is given to the electron. This energetic electron can then be detected, Figure 8. [20] [33] The second detection method is charge-current capture of a neutrino on an atomic nucleus. A neutrino incident on a neutron can be captured changing one of the neutrons down quarks into an up quark, and emitting an electron. [4] [17] [20] An antineutrino incident on a proton can be captured changing one of the protons up quarks into a down quark, and emitting a positron. [10]

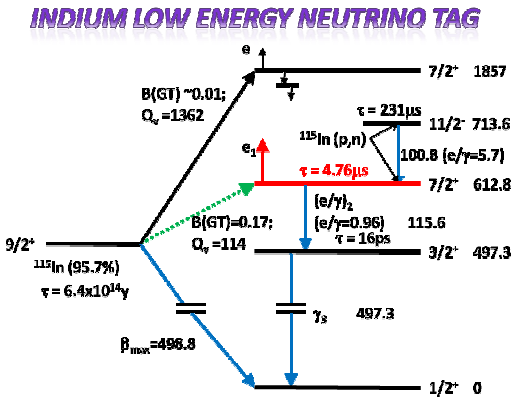

Figure 9 ^{115}Indium to ^{115}Tin Energy Levels. The green dashed line shows ^{115}Indium to ^{115}Tin via neutrino capture and the diagonal blue line shows ^{115}Indium to ^{115}Tin via beta-decay.

2.3 The Indium Neutrino Capture Reaction [4]

The LENS detector is a unique real-time charge current (CC) neutrino detector using a tagged ν_e-capture on ^{115}In:

$$\nu_e + {}^{115}In \rightarrow e^- + (\tau = 4.76\ \mu s)\ 2\gamma + {}^{115}Sn$$

Figure 10 ν_e capture on ^{115}In. An ν_e is captured on ^{115}In, creating ^{115}Sn in an excited state. The excited state of ^{115}Sn decays with a mean lifetime of τ= 4.76 μs by emition of two gamma rays providing a coincidence tag

In contrast to other CC capture based experiments most famous $\nu_e + {}^{37}Cl \rightarrow e^- + {}^{37}Ar$ [17], the ^{115}In reaction populates an excited state of ^{115}Sn which subsequently decays by γ-rays which can tag the ν capture. The detector takes advantage of cutting edge technology of organic liquid scintillator loaded with 8% - 10% by weight Indium and a unique detector design allowing for excellent spatial resolution and background suppressions that help with visualization of the γ-ray tag.

The ^{115}In neutrino capture reaction (nuclear schematic— Figure 9) is unique because:

1) It provides a prompt signal e^- with specific energy, $E(e^-) = E(\nu_e) - Q$, that uniquely specifies the energies of incident ν_e's thus providing a true energy spectrum of the incident ν_e's. The Q-value of the reaction is only 115.34(5) keV [34] [35]. This is the lowest known Q-value for neutrino CC capture, providing sensitivity to >95% of the pp solar ν spectrum (0-420 keV).
2) The prompt nuclear state following the ν capture is a ^{115}Sn nucleus in the 7/2+ excited state. This excited state decays by emission of two gamma rays with mean lifetime of τ=4.76μs providing a coincidence tag. This tag is the central feature in LENS that allows on-line tagging of ν events against background.
3) The natural abundance of ^{115}In is ~95.7%.

A major background for LENS arises from the natural β-activity of ^{115}In, ~10^{11} β's per pp signal electron. The space and time delayed coincidence of the Indium ν tag that provides a direct suppression of ~10^5 β's per pp signal electron. The remaining suppression can be achieved by analysis cuts on false tag events to fit the template of the ν tag in detail (see Chapter 5: Background Events for more details on these cuts).

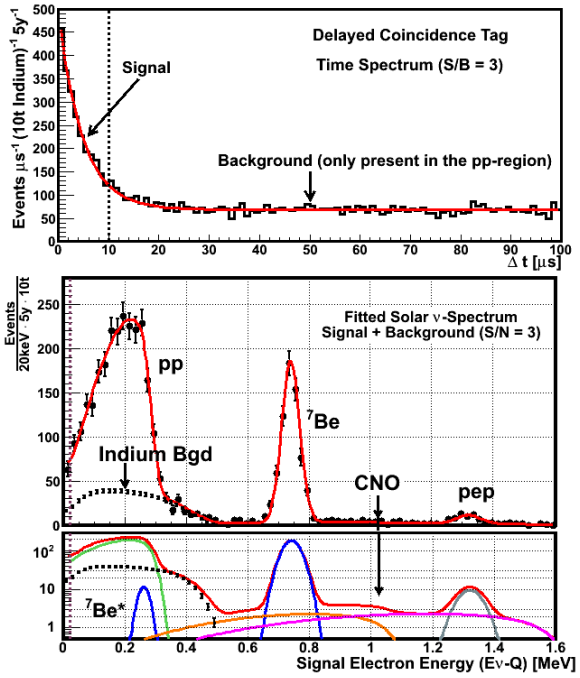

Figure 11 The LENS detector solar neutrino detector response. The signal time spectra and random coincidence background for a signal to noise ration of 3:1 and a pp-ν signal window of Δt<10μs is shown in the top graph. The middle graph shows the ν-energy spectrum derived from the first 10μs of the top graph and the background spectrum from an equal time window. The signal is the solar ν spectrum as predicted by the SSM (offset by 115.3 keV) and modified by the MSW-LMA model of neutrinos and detection efficiencies expected in the current design (pp-ν 64%, ^{7}Be-ν 85%, CNO-ν and pep-ν 90%). The pp-ν rate is ~40 pp-ν events/ ton In / year. The bottom graph shows the details of the CNO ν-signal, reprinted from Ref. **(37)**.

The ^{115}In β-spectrum extends up to 497.47(2) keV [34] [35], overlapping only the pp-ν signal electrons. Thus the ^{115}In β-decay is a background only for pp-ν's, Figure 11. Because the signal in LENS is a coincidence event, internal contamination with specific activity less than that of ^{115}In β-decay is not an issue in LENS unlike low energy solar ν detectors so far, such as Borexino which do not have a ν-signature. This means that the radiopurity demands of LENS scintillator are ~10^3 time less severe than for Borexino. Random external gamma rays together with ^{115}In β-decay events can mimic the tag, but they are controllable via passive shielding and a potential buffer scintillator envelope. Cosmogenic secondary protons can produce the same tag cascade as the ν signal, but their rate is adequately low at a depth of 2000 mwe and easy identification converts them into reliable 'proxy' confirmation in LENS.

The DAQ system is designed to yield a triple-coincidence spectrum event – sorted with delay time and energy. The total signal is extracted from the coincidence time delay spectrum, Figure 11 top. The initial event is followed by a cascade decay with the signature lifetime of τ=4.76μs. The background from random coincidences is measured independently and precisely at longer delays as shown in Figure 11 top. A fit to the exponential decay plus the constant background gives the total signal and the background. The energy spectrum, Figure 11 bottom, which assumes an energy resolution with a photoelectron yield of ~900 p.e./MeV, shows well-separated solar features that for the first time can yield precise rate data for each of the low energy solar neutrino sources. The design goal is to achieve ~2000 pp ν events (~750 ^{7}Be and 200 CNO ν events) in five years with 10 tons of Indium in LENS. With the backgrounds from fits to the time spectra in Figure 11 top, a statistical precision of ±2.5% can be achieved for the pp-ν signal. Chapter 5: Background Events goes through step-by-step explanations of the analysis cuts that lead to a background suppression by a factor of $6x10^{11}$ with a signal loss of only 36% that results in an overall S/N~3. The goal of the miniLENS program is to demonstrate detector performance and background rejection feasibility in a full scale LENS detector.

2.4 Neutrino Capture Cross Section on ^{115}In

The Indium CC ν-capture rate depends on the Gamow-Tellar matrix element, B(GT), which has been measured via ^{115}In (p,n) reactions [36] as B(GT) = 0.17±10% which is useful for preliminary ν rate estimates. A precision measurement, in particular by means of only weak interactions, requires an expensive calibration of B(GT) via ν_e's with a strong electron capture source (producing mono-energetic neutrinos) such as ^{51}Cr. Figure 12 bottom shows the LENS response for four 100 day runs with 10 MCi ^{51}Cr. [37]

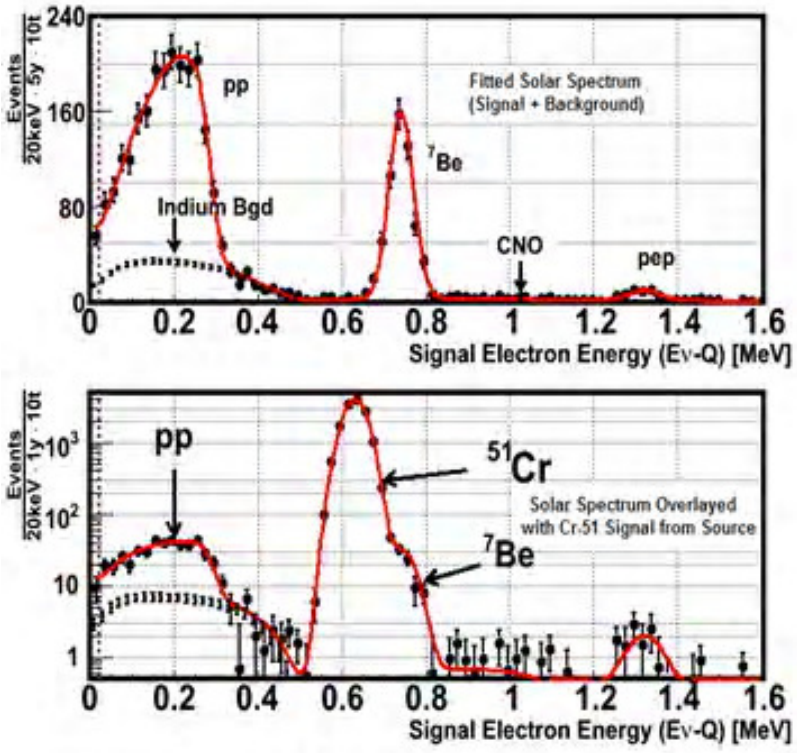

Figure 12 Response of the LENS detector to four 100 day exposures to 10 MCi ^{51}Cr calibration sources. The anticipated solar neutrino spectrum in LENS is shown (top). The anticipated neutrino spectrum with a ^{51}Cr source located in the center of the LENS detector is shown (bottom). The source signal is two orders of magnitude larger than the solar neutrino background, reprinted from Ref. **(37)**.

The major challenge for LENS calibration is the production and handling of a MCi source. This has been done in Europe and Russia before, but has never been done in the Unites States. There is an effort underway to design sources to be made at Oak Ridge National Laboratory (ORNL) and design containers for transporting a MCi source to the DUSEL sight once LENS is operational; however, this is not a must have item for LENS

initially, there is no funding yet available, and there is an alternate initial calibration scheme using Borexino results; therefore, these efforts are low priority at the moment.

$$\sigma_c = \left(\frac{R_L}{R_B}\right)\left[\frac{[p_{ee}\sigma_e + (1-p_{ee})\sigma_{\mu,\tau}]}{p_{ee}}\right]$$

Equation 5 ν_e charge-current capture cross section on ^{115}In derived from Borexino ^{7}Be results.

Borexino has observed the ν-e scattering signal; a well understood cross section, for ^{7}Be solar neutrinos and thus provides a way to initially bypass the MCi source calibration (similar to ^{8}B measurements in SK and SNO). LENS and Borexino measure the same flux with two different reactions, LENS based on CC (ν_e only) and Borexino on NC-sensitive ν–e scattering (sensitive to all flavors— ν_e, ν_μ and ν_τ). The ν_e capture cross section on ^{115}In can thus be written as in Equation 5. In LENS and Borexino p_{ee} is the ν_e survival probability and σ_e and $\sigma_{\mu,\tau}$ are the well-known scattering cross sections for $\nu_{(e,\,\mu,\text{ and }\tau)}$. The derivation of σ_c thus depends only on the measured rates and θ_{12}, and is independent of uncertainty in the ^{7}Be-ν flux in the SSM (~8%). The absolute detection efficiency for the other families of solar neutrino (pp, pep, CNO, etc) can be determined from the energy dependence on σ_c, $\sigma_c \propto (E_\nu\text{-}Q)^2$. Borexino and/or other planned ν-e scattering detectors will eventually measure the pep and CNO ν fluxes. Thus by a global analysis of the LENS and Borexino data sets for ^{7}Be, pep, and CNO ν fluxes (6 data sets) one can determine the fluxes independent of any solar model as well as θ_{12} and Δm_{12}^2, with possible improvements to the measured precision of θ_{12}.

2.5 Scientific Goals of LENS

A real time precision measurement of the pp solar neutrino flux is achievable for the first time ever with and only with the LENS detector. This measurement will allow us to study in great depth models of neutrino physics and astrophysics. Figure 13 shows what this experiment may look like in an underground laboratory hall in DUSEL.

As the LENS detector has matured the science objectives of the detector have expanded, from a purely solar neutrino luminosity measurement to possibilities in other current questions: sterile neutrinos, insights into dark energy and mass varying neutrinos (MaVaN), understanding of CNO reactions in the Sun, and possibly neutrino less double

β-decay (ββ0ν) measurements. The detector design is truly unique, and the science that such a detector may be able to probe is exceptional and continuously growing.

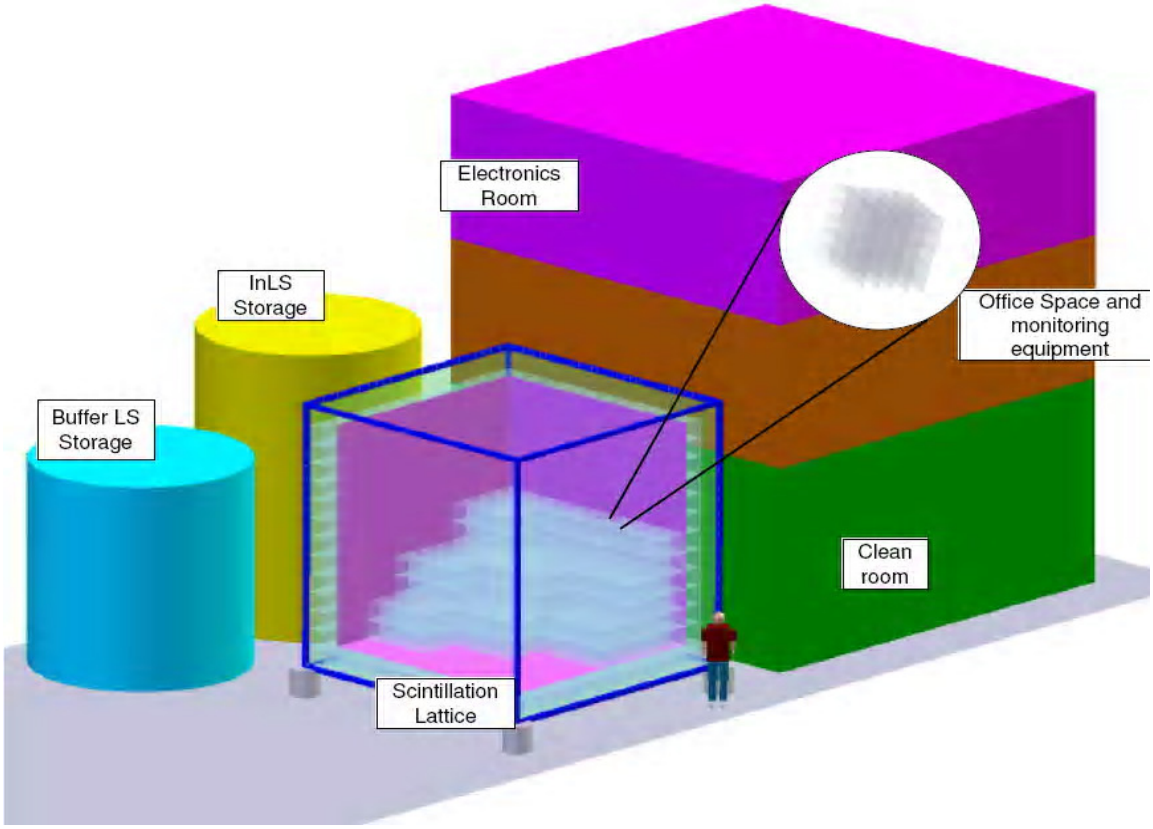

Figure 13 LENS experimental hall. This is a solid model showing what the LENS detector and major support infrastructure will look like in one of DUSEL's experimental halls.

2.5.1 Compare L_ν –vs– L_γ

The complete low-energy flux data from LENS, Figure 11, coupled with the ν_e survival probability, p_{ee}, will allow us to deduce the ν_e pre-conversion fluxes at the Sun. Each of the low-energy reactions, Figure 11, represents energy release from specific reactions in the Sun. These reaction coefficients have been accurately calculated. [38]

Once the pre-conversion fluxes at the Sun are know the solar luminosity inferred via ν's, L_ν can be calculated. L_ν is the total energy released from all features of Figure 11. L_ν can be compared to the solar energy released by photons, the solar luminosity inferred via photons, L_γ. The ν parameters can be varied until L_ν and L_γ balance is achieved. The final ν parameters from the ν–γ balancing may suggest fundamentally new particle physics beyond the standard model.

L_ν will need to be corrected for the overall reduction in flux due to the mixing parameter θ_{13}. θ_{13} reduces all ν fluxes by the factor $\cos^4 \theta_{13}$ independent of energy. If ignored an inherent deficit will appear in the $L_\nu = L_\gamma$ equality. The limit on the θ_{13} value will be improved by the LENS luminosity analysis, and/or constraints on θ_{13} from future reactor experiments.

The luminosity balance $L_\nu = L_\gamma$ is based on broad astrophysical assumptions: 1) nuclear reactions are the sole energy source in the Sun, and 2) the Sun is in a quasi-steady state of energy production (the amount of fuel and the consumption/production rates are fairly constant). Due to Compton scattering, pair production, and photoelectric effect, the L_γ measured today is a measurement of the energy produced in the Suns core between 10^4 and 1.7×10^5 years ago [39] [40]; however, L_ν is a measurements of today's energy production in the Sun (ν's take approximately eight minutes to arrive at the earth from creation), Figure 14. Therefore, the LENS model-independent luminosity balance test is critical to verify these two root level assumptions.

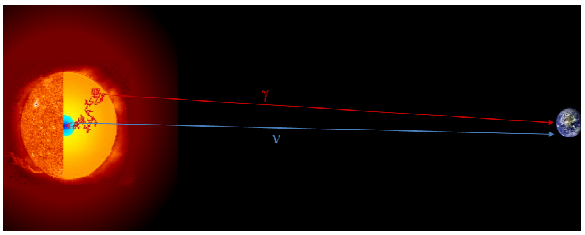

Figure 14 Neutrino path from creation vs photon path from creation. The red path is a likely path of a photon. From the Sun's core to the surface it is absorbed and re-emitted many times, finally reaching the surface and traveling to the earth. The total process takes between 10^4 and 1.7×10^5 years. [39] [40] The blue path is a likely path of a neutron. It is created and travels through the Sun with no interactions, arriving at the earth minutes after creation.

If with the best knowledge of neutrino physics a residual inequality at high precision is revealed, then major new science may be exposed!

1) $L_\nu > L_\gamma \rightarrow$ the Sun may be getting hotter with time
2) $L_\nu < L_\gamma \rightarrow$ the Sun is cooling or the Sun has non-nuclear sources of energy

The success of such possibilities requires decoupling the fluxes from the neutrino parameters. A global analysis of the LENS results for the individual fluxes provides an independent precision measurement of neutrino parameters such as θ_{12}, given that θ_{13} will be measured precisely via the reactor neutrino experiments.

2.5.2 Dark Energy and Mass Varying Neutrinos (MaVaN)

Dark energy is currently one of the most pressing open questions in physics today. Both neutrino phenomena and models of dark energy occur in very similar energy scales, purely as a coincidence thus far but possibly with a more fundamental connection? The latter view point was explored recently, and they found that MaVaN's may behave as a negative pressure fluid that could be the origin of cosmic acceleration. [41] This is accomplished by making the ν mass a dynamic variable dependent on ν density. Model-independent tests of MaVaNs as a source of dark energy are cosmological in nature; however, with mild assumptions one can exploit ν oscillations to test the MaVaN hypothesis. The Sun is the only close object that exhibits high ν density (~10^7 ν's/cc), and is thus the ideal laboratory for to study MaVaNs. [42] Solar ν's with energies of less than ~500 keV are particularly relevant for studying the MaVaN scenario due to ν's in this energy range being subject only to vacuum oscillation and not matter enhanced flavor conversion.

The identification of MaVaNs may be aided by an enhancement in the survival probability of pp ν's from the Sun over the basic vacuum value by ~10% while not affecting the flux of higher energy ν's. [43] This effect is a distinct feature of the MaVaN hypothesis and cannot be easily caused by other non-standard ν physics models. Thus the ability of LENS to explore this solar ν energy regime with high precision can lead to a unique test of the MaVaN theory for the origin of dark energy.

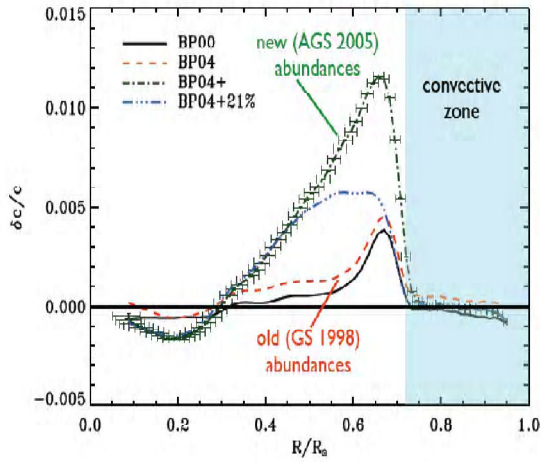

Figure 15 Effect of revised solar abondances on helioseismology results. Reproduced by permission of the AAS from **(47)**

Source	BPS08(GS)	BPS08(AGS)	Diff.
pp	5.97(1± 0.006)	6.04(1±0.005)	1.2%
pep	1.41(1±0.011)	1.45(1± 0.010)	2.8%
hep	7.9(1± 0.15)	8.22(1± 0.15)	4.1%
^{7}Be	5.07(1±0.06)	4.55(1±0.06)	10%
^{8}B	5.94(1± 0.11)	4.72(1± 0.11)	21%
^{13}N	2.88(1± 0.15)	1.89(1+ 0.14-0.13	34%
^{15}O	2.15(1+0.17-0.16	1.34(1+0.16-0.15	31%
^{17}F	5.82(1+0.19-0.17	3.25(1+0.16-0.15	44%
Cl	8.46 (+0.87-0.88)	6.86(+0.69-0.70)	
Ga	127.9(+8.1-8.2)	120(+6.9-7.1)	

Table 1 ν flux predictions for low (col 2) and high (col 3) abundances [32] The measued ^{8}B flux from SNO salt phase is 5.54 vs. 4.72 (BPS 08, AGS)

2.5.3 CNO Reactions in the Sun

Predictions of the Standard Solar Model (SSM) have provided the fundamental basis for interpreting and evaluating measured solar ν fluxes. The measured solar ν fluxes verified the basic assumptions that lead to the conclusion that the dominant energy mechanism in the Sun is the proton-proton (pp) chain with a significantly smaller contribution due to the CNO cycle. This confirmation comes not only from the solar ν result, but also the spectacular agreement with heliosiesmology. The specific CNO ν flux prediction however, is yet to be tested due to the low CNO ν flux and high background at CNO ν energies. On the other hand serious progress has been made in measuring the relevant fusion cross sections at the LUNA and LENA facilities [(44)] that indicate systematically lower ν fluxes, which pose more difficulties for a CNO ν flux measurement particularly in scintillation approaches based on electron scattering.

The solar model ν flux predictions depend fundamentally on the metallicity in the Sun— particularly the abundances of the light elements carbon, nitrogen, and oxygen. So far the SSM adopts results based on measurements of optical absoption lines of these elements at the solar surface. [(45)] A major crisis in the CNO problem has recently precipitated by new results that suggest a reduction in these abundances by 30-50%. [(46)] The result is significantly lower metallicity that has the effect of destroying the agreement with heliosiesmology results as in Figure 15. [(47)] The effect on the ν fluxes is shown in Table 1. [(32)] The CNO problem is much more than the local conflict of solar ν fluxes. The understanding of the CNO reactions reaches into the general problem of star formation and solar evolution in this framework. [(48)]

Thus we have a new "solar neutrino problem." There is no clear indication on how to resolve the conflict introduced by the light abundance results. The most fruitful way is a direct and reliable measurement of the CNO ν flux. This needs massive scintillation detectors such as Borexino and the future SNO+ [(49)] that are sensitive to low energies. However, these detectors, based on e – ν scattering yield untagged electron recoil continua that are frequently indistinguishable from background, particularly from impurities such as ^{210}Bi even in the extremely small concentrations achieved in Borexino. Cosmic ray secondaries such as ^{11}C are a further serious problem, though less so in

SNO+ because of its deep location. It is here that LENS can play a decisive role. LENS ν detection has a distinct signature which discriminates against all the above background. The CC-based method gives the CNO spectrum directly (unlike electron recoil which smears the incident ν spectrum) that can be clearly resolved (as seen in Figure 11) from the line features due to other low-energy solar ν features.

2.6 Summary

LENS is the only detector under development that can measure the entire solar neutrino spectrum above 115 keV via the charged current interaction. Over 95% of neutrinos from the Sun have energies below 2 MeV, where only limited high-precision spectroscopic data is currently available. Measurement of the full spectrum of these neutrinos would provide a model-independent determination of the current rate of energy generation in the solar core, allowing a comparison with the current photospheric luminosity, which arises from nuclear reactions that occurred ~ 10^5 years ago. Such a comparison is a stringent test of our understanding of energy generation in the Sun and neutrino oscillation parameters. The LENS measurement of the CNO spectral flux will provide a critical and timely input to the recent disagreement between solar CNO abundances and helioseismology; the previous agreement had been one of the longstanding fundamental foundations of the belief in the Standard Solar Model. Finally, the spectrum below 2 MeV will provide direct experimental validation of the predicted low-energy dependence of neutrino flavor survival in the current MSW-LMA model. The novel aspects of the LENS detector can be exploited in testing new suggestions for low energy neutrino phenomenology, MaVaN's.

Chapter 3: Metal Loaded Organic Liquid Scintillator (MLLS) Technology

3.1 Introduction to Organic Liquid Scintillator (OLS)

Organic liquid scintillator (OLS) have long been used for measuring ionizing radiation through light emission from molecular excitations. An OLS contains an aromatic component (benzene ring). Historically this aromatic component has typically been Benzene or Toluene; however, in recent years safer materials such as 1-2-4 Trimethyl Benzene (PC), Phenylxylylethane (PXE), and Linear Alkylbenzene (LAB) have been adopted. The OLS is often doped with a fluor and wavelength shifter. An ionizing particle ($\beta^{+/-}$, α, γ, etc.) traveling through the medium will lose energy and excite the π-electrons associated with the aromatic component to singlet and triplet states, S* and T* respectively. The aromatic component will then de-excite:

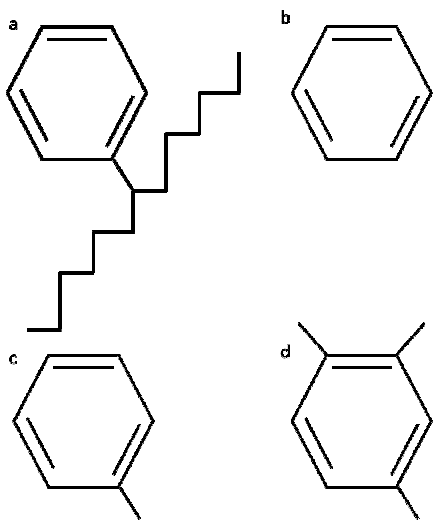

Figure 16 Moleculer diagrams of some common Liquid Scintilators.
a) Linear Alkylbenzene (10 carbon chain on average)
b) Benzene
c) Toluene
d) 1-2-4 Trimethyl Benzene

$S^* \rightarrow S_o$ + scintillation photon,

$T^* \rightarrow S_o$ + scintillation photon (delayed with low probability),

$T^* + T^* \rightarrow S^* + S_o$ + phonons (delayed)

Many experiments add fluors/wavelength shifters to the primary scintillator to increase the scintillation signal, decrease self absorbance, and match the photo cathode response of the photo multiplier tubes (PMTs). With the addition of flours the primary OLS transfers the deposited energy to the flour, via molecular collisions, thus by non-radiative energy transfer. The fluor then de-excites by emission of a scintillation photon. This photon then traverses the detector and is detected with a PMT.

Organic liquid scintillator (OLS) has been the detection medium of choice for ν experiments since the Reines and Cowan ν discovery experiment. [10] This is largely due to the lower cost for building a large OLS detector compared to other detection medium

such as plastic scintillators. Most recent neutrino experiments utilizing pure OLS are Borexino [33] and KamLAND [50].

3.2 Metal Loaded Organic Liquid Scintillator (MLLS)

Metal loaded liquid scintillators (MLLSs) are an extremely useful detection medium for ν physics. One can place a target nuclei in solution with an OLS for charge-current neutrino capture ([115]In MLLS for the LENS experiment first synthesized at Bell Laboratory in 1978 [4] [51]) or a nuclei with large neutron capture cross-section for delayed coincidence tagging in $\bar{\nu}_e$ experiments where an $\bar{\nu}_e$ is captured on a proton via charge-current capture producing a positron and a neutron. [10] [52] [53] [54] Both of these applications of MLLS have a key common aspect; they require:

1) High metal loading (up to 10% loading for LENS) with long term chemical stability,
2) High scintillation efficiency ($h\nu$/MeV),
3) Sufficient optical clarity ($L_{1/e}$~10m), and
4) Low radioactive impurity contaminates.

Satisfying these requirements has lead to years of research and development in chemistry and nuclear chemistry particularly at Bell Labs—Figure 17 [55] [56] [57], VT [58], and BNL [59], but also in Europe, Japan, and Russia.

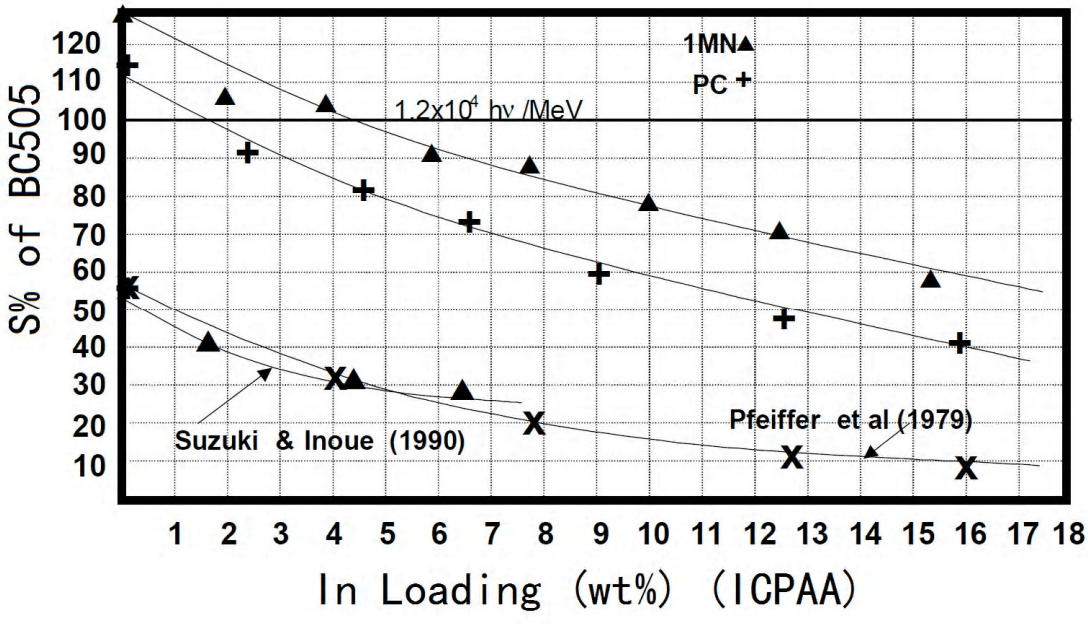

Figure 17 Light yield vs In loading in PC 1MN solvents. This graph was taken from Ref. (57)

3.2.1 How MLLS is synthesized

The basic approaches developed to synthesize MLLS involve forming organo-metallic complexes with carboxylic acid in aqueous media and extracting them into an organic solvent then combining the organo-metallic complex with an aromatic OLS by one of three means 1) the organic solvent for the extraction is the OLS, [55] [56] [59] Figure 18, 2) vacuum evaporating the solvent off to form solid a solid of organo-metallic complex and dissolving the solid into the aromatic OLS, [58] Figure 19, and 3) mixing the organo-metallic complex solvent solution with the aromatic OLS then vacuum evaporating off the solvent, Figure 20.

Figure 18 illustrates the basic production line for Indium loaded OLS (InLS) initially developed at Bell Laboratory. [55] [56] The synthesis begins with neutralization of

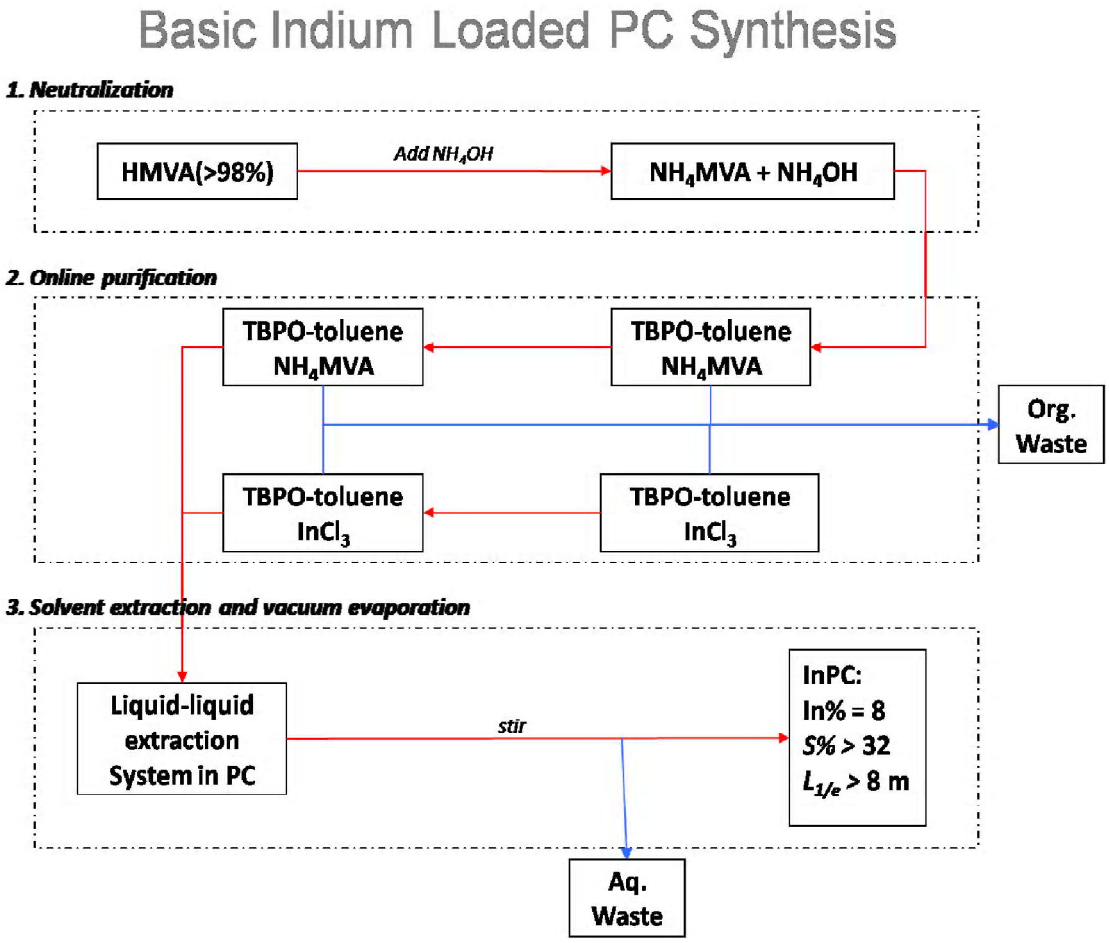

Figure 18 Basic indium loaded PC synthesis. The synthesis start with the neutralization of organic acid, HMVA, then undergoes online purifications with Toluene TBPO, and is completed by liquid-liquid extraction of In directly into PC.

an organic acid (2-methylvaleric acid {HMVA} in this case) with NH_4OH creating an aqueous solution of [NH_4MVA and NH_4OH]. This solution and an aqueous solution of $InCl_3$ are then mixed with an OLS. This is the so called Liquid-Liquid extraction step of the synthesis, 3.2.2 Introduction to Liquid-Liquid Extraction. Here the In^{+3} combines with three MVA^{-1}'s creating $In(MVA)_3$ which migrates into the OLS due to the relative solubility of $In(MVA)_3$ in the OLS compared to the aqueous solution. The organic and aqueous phases are then separated gravimetrically due to the differences in densities. The aqueous portion is disposed, and the resultant organic solution is an indium organo-complex, $In(MVA)_3$, in OLS (PC or LAB for the work done at Virginia Tech)—InLS. The online purification steps of Figure 18 were left out of this discussion, but are crucial for manufacturing long attenuation length OLS, and are discussed in detail in section 3.3 LENS recipes for Indium Loaded Liquid Scintillator (InLS).

3.2.2 Introduction to Liquid-Liquid Extraction

Liquid-liquid extraction, also known as solvent extraction, is a process used to separate compounds based on relative solubility into two immiscible liquids, most common is an aqueous solution and an organic solvent, extractions with molten metal in contact with molten salt are also possible. The process of liquid-liquid extraction is a robust technique used commercially in nuclear reprocessing, metal ore processing, perfume production, and other industries.

3.3 LENS recipes for Indium Loaded Liquid Scintillator (InLS)

The basic approach developed to synthesize Indium loaded liquid scintillator involves forming organo-indium complexes in aqueous medium and extracting them into a buffer organic solvent (Hexane currently). Then the organo-indium complex is dissolved in an aromatic OLS by one of three means 1) solvent evaporation to form solid organo-indium complex and dissolving the solid into the aromatic OLS, 2) mixing the organo-indium complex solvent solution with the aromatic OLS then evaporating off the solvent, and 3) direct extraction of the organo-indium complex into the aromatic OLS without the means of a buffer organic solvent, discussed in 3.2.1 How MLLS is synthesized— this method is currently used by LENS collaborators at Brookhaven National Laboratory (BNL). [59]

3.3.1 Chemical procurement, purity, and pre-extraction purification

Light yield, attenuation length, and stability are greatly affected by MLLS purity (chemical and radiopurity). It is very important that all chemicals going in to the synthesis line are of the highest purity.

Most of the purification steps that we have developed are applied before and during the synthesis of the InLS. Purification schemes that one would employ after the InLS synthesis are unsuitable because they would likely remove some of the In as well as other inorganic impurities. The removal of chemical impurities critically affect the transmission of the signal light in the InLS and long term stability of the InLS—investigations into long term performance of the InLS show that some impurities induce slow chemical reactions that cause the light transmission of InLS to deteriorate gradually. Thus we have developed several chemical purification steps before and during the synthesis to enhance the performance of the final InLS:

1) Purification of chemicals in the aqueous phase is done by solvent extraction with toluene containing 0.5% by weight of Tri-n-butyl phosphate-oxide (TBPO mixture is toluene-TBPO). These aqueous phase chemicals are Indium tri-Chloride, Ammonium Hydroxide, and Ammonium Carboxylate.
2) Purification of chemicals in the organic phase is achieved through dry column absorption (6 cm diameter 120 cm long glass column loaded with 60 cm activated 100-500 micron acidic aluminum oxide.) These organics include 1,2,4-trimethylbenzene (PC), Linear Alkyl benzene (LAB), Toluene, and Hexane.
3) Purification of 2-Methylvaleric Acid (HMVA) is done by temperature dependent vacuum distillation. The distillation column is 30cm long and filled with Teflon coils. The Teflon coils provide many theoretical plates that can effectively separate the organics in HMVA, which have boiling points at ~10 ^{o}C intervals. The vacuum distillation is set to remove ~10% of the low boiling point fraction, collect ~80% of the distilled HMVA, and leave ~10% of the high boiling point fraction (usually yellow to amber in color) in the distillation vessel.

These purification steps are largely to purify the liquids to obtain excellent optical properties in the final InLS. We will also need to remove radioactive impurities in the

liquids (Uranium, Thorium, Potassium, and daughters). The cleaning of radioactive impurities is largely taken care of in the processes for chemically cleaning the liquids. For those chemicals that are vacuum distilled, it is expected that the vacuum distillation will remove radioisotpic impurities, including Radon. The radio-purification of the inorganic solutions is accomplished by solvent extraction during the toluene-TBPO washing during chemical purification. PC, LAB, Toluene, and Hexane are filtered through dry columns of aluminum oxide. This along with silica gel chromatography [60] yields purities of 10^{-14} to 10^{-16} g/g for Thorium, 10^{-14} to 10^{-17} g/g for Uranium, and 10^{-12} g/g for Potassium. [61]

Even with purification measures, the synthesis of InLS is largely affected by the purity of the raw chemicals used. As chemicals vary slightly from supplier to supplier (and batch to batch), I list in Table 2 the chemicals used, purity and the suppliers.

Chemical	Abbreviation	Purity	Supplier
Indium tri-Chloride	InCL3	99.999	Indium Corp. of America
2-Methylvaleric Acid	HMVA	98%	Sigma Aldrich (Alfa Aesar)
Ammonium Hydroxide	NH4OH	?	VWR International
Tri-n-butyl phosphate-oxide	TBPO	98%	Alfa Aesar
Hexanes		99.90%	Fischer Scientific
Ammonium Acetate		98%	Sigma Aldrich
Deionized water	DI Water	18MΩ	VT Physics Department DI water plant
Linear Alkyl benzene	LAB	?	Petresa Canada via BNL
1,2,4-trimethylbenzene	PC (pseudo cumene)	98%	Sigma Aldrich
100-500 micron Acidic Aluminum oxide	Al_2O_3	?	Acros Organics
Toluene	Tol	?	Fischer
p-Bis(o-methylstyryl) benzene	bis-MSB	?	Eastman
2,5-Diphenyloxazole	PPO	?	Sigma Aldrich

Table 2 List of chemicals, purity and suppliers that are used in the LENS 115In MLLS synthesis. We are moving away from those chemicals supplied by Sigma Aldrich due to issues with contaminates that our purification methods are not able to remove, most notably HMVA.

There are several key performance criteria that must be considered in selecting the OLS for metal-loading a multi-ton underground OLS neutrino detector:

1) Excellent optical transparency (attenuation length)
2) High light output (light yield)
3) Low levels of chemical contaminants
4) Low levels of radioactive contaminants
5) Chemical stability when doped
6) Low toxicity
7) Low reactivity
8) High flash point (low vapor pressure)

Points (1-5) above are directly related to the performance of the detector, and (6-8) are concerns for compatibility with materials in and of the detector. Environmental and human safety is also a major concern in an underground laboratory environment. For LENS the attenuation length should be greater than 8m. The minimum light yield needed is still being constrained for the purpose of using InLAB but is not more than that of InPC ($S\%_{PC}$~55%). The chemical stability refers to stability against slow chemical reactions, such as hydrolysis and polymerization, which can lead to formation of color, gels, or precipitates causing the OLS attenuation length to degrade.

3.3.2 OLS Solvents

Several OLS's were studied with these criteria in mind. Some of these are PC, Phenylcyclohexane (PCH), di-isopropylnaphthalene (DIN), 1-phenyl-1xylyl ethane (PXE), and LAB. [59] [62] The most promising OLS's were found to be PC and LAB. [59] Recipes and data for loaded and unloaded scintillator for both PC and LAB will be presented below.

PC is the benchmark we use for measuring scintillation light yield (S%) were PC S% = 100%. LAB has S% ~ 85%. Both PC and LAB have comparable attenuation lengths of $L_{1/e} >> 8$m and are stable for years if carefully stored in an oxygen free dark environment.

PC is an excellent OLS with regards to $L_{1/e}$ and light yield. It's short comings are that it has a low flash point and is chemically aggressive towards materials.

	PC	LAB	PXE[a]
Molecular Formula	C_9H_{12}	$C_{6+n}H_{2n+6}$[b]	$C_{16}H_{18}$
Density (g/mL)	0.876	0.864	0.99
absorption at 430nm	0.002	0.001	0.022
index of refraction[a]	1.504	1.482	1.565
S% (%)[c]	1	85	87
Flash point (^oC)	48	130	145

Table 3 Properties of some OLS's of interest to LENS. All OLS's were purified via **Al_2O_3 dry column purification.**
[a]Values take from Ref. **(59)**
[b]Average n~12
[c]S% with respect to PC—Light yield of PC~$1.25x10^4$ hν/MeV

LAB was first suggested as an OLS for large scale neutrino experiments by the SNO^+ collaboration. (63) LAB is composed of a linear alkyl chain with a length of 10-13 carbons with a benzene ring attached to one of the carbons, Figure 16. LAB with its comparable optical properties to PC, higher flashpoint, high volume commercial availability, and less stringent material compatibility issues suggest it would be an excellent scintillator for large scale OLS neutrino detectors. The negative aspects of LAB are—1) although the light yield is nearly that of PC it may still not be suitable due to considerably lower light yield than PC after metal loading and 2) attenuation lengths of indium loaded LAB (InLAB) degrade quickly (this is being worked on).

3.3.3 InPC Recipe

Initial work for the LENS scintillator was done using PC. The synthesis recipes have matured over the years. Presented here is the latest recipe which gives high stability and very high light yield, Figure 19. The unit eq is mole equivalents. The exact extraction for this discussion is zVt58_Hex_Ac synthesized by Zheng Chang, Steven Derek Rountree, Raju Raghavan. Other InPC extractions are reported in Table 15 to Table 17 in Appendix B: Indium Liquid Scintillator Recipes.

The first step is neutralization of previously distilled HMVA. This is done by slowly adding 5.1eq NH_4OH to an immiscible solution of 3.0eq HMVA and 40eq DI water. The resulting solution is a basic aqueous solution (pH~9.85) with ions of NH_4^+ and MVA^-. The resulting solution then undergoes purification by vigorously mixing and

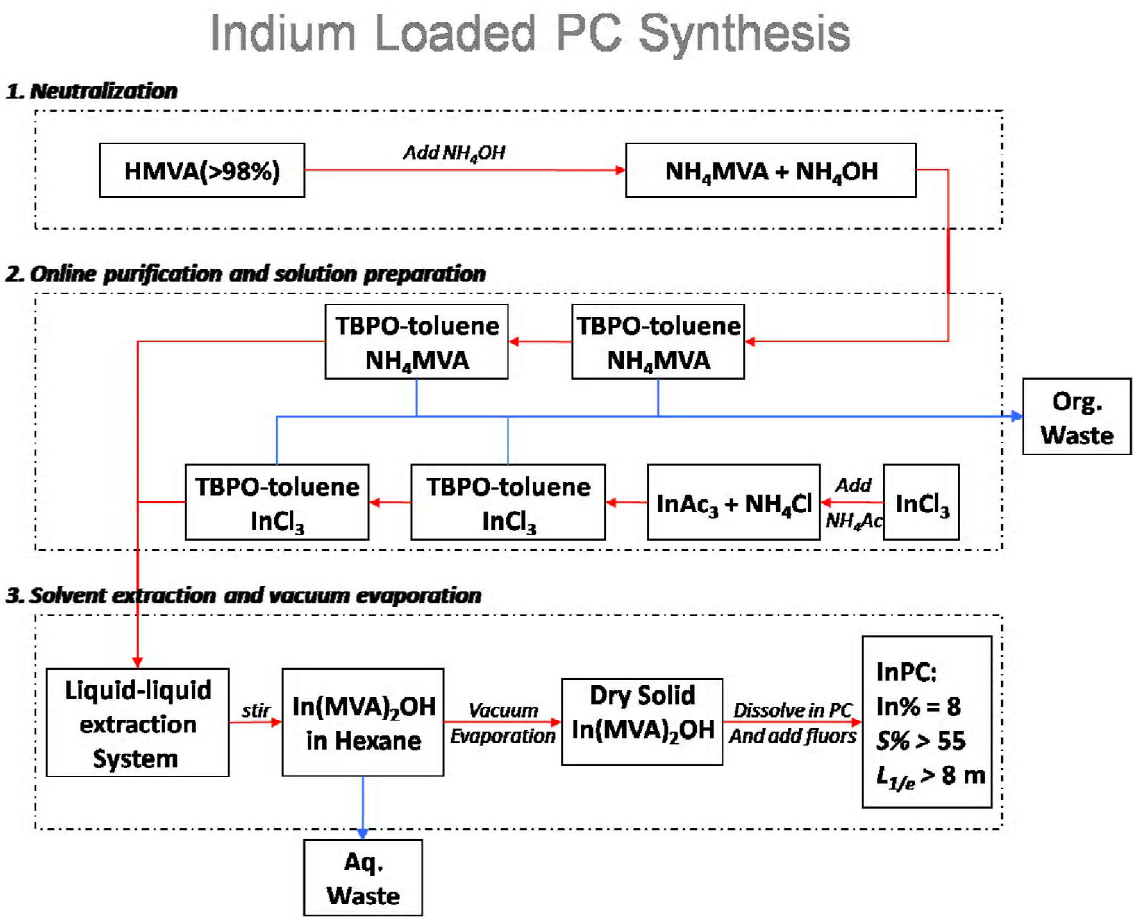

Figure 19 Schematic for Indium loaded PC synthesis. Starting with neutralization, continuiing with online purification and solution preparation, and concluding with solvent extraction and vacuum evaporation.

separating it twice with equal mass of Toluene with 0.5% by weight TBPO (Toluene-TBPO). Next a solution containing 8eq NH_4Ac, 1eq $InCl_3$, and 40eq DI water is prepared, and then purified using the same Toluene-TBPO purification from above. The last component solution is 40eq Hexane with 40eq DI water. The Hexane and Water solution is stirred vigorously to provide maximal surface area between the aqueous and organic solutions (Hexane is used here to provide a large amount of organic solvent which can later be evaporated off, thus increasing extraction efficiency at higher pH's and increasing $S\%_{PC}$). The solutions containing $InCl_3$ and MVA are then added slowly to this Hexane and water solution. As the solutions are added the liquid becomes somewhat cloudy; however, once the total volume of all solutions have been added the solution becomes clear on the order of an hour. The solution is then allowed to settle. We

separate the aqueous and organic portions in a separation funnel. The pH of the aqueous portion is measured, ~6.75, this is the extraction pH. Now we have a solution of $InMVA_2OH$ in Hexane. The hexane in this solution is vacuum evaporated in a Rotavapor apparatus leaving a crystalline like (no real crystalline structure) solid of $InMVA_2OH$. This solid is then dissolved in PC at a ratio of 3g:13g, $InMVA_2OH$:PC, yielding InPC.

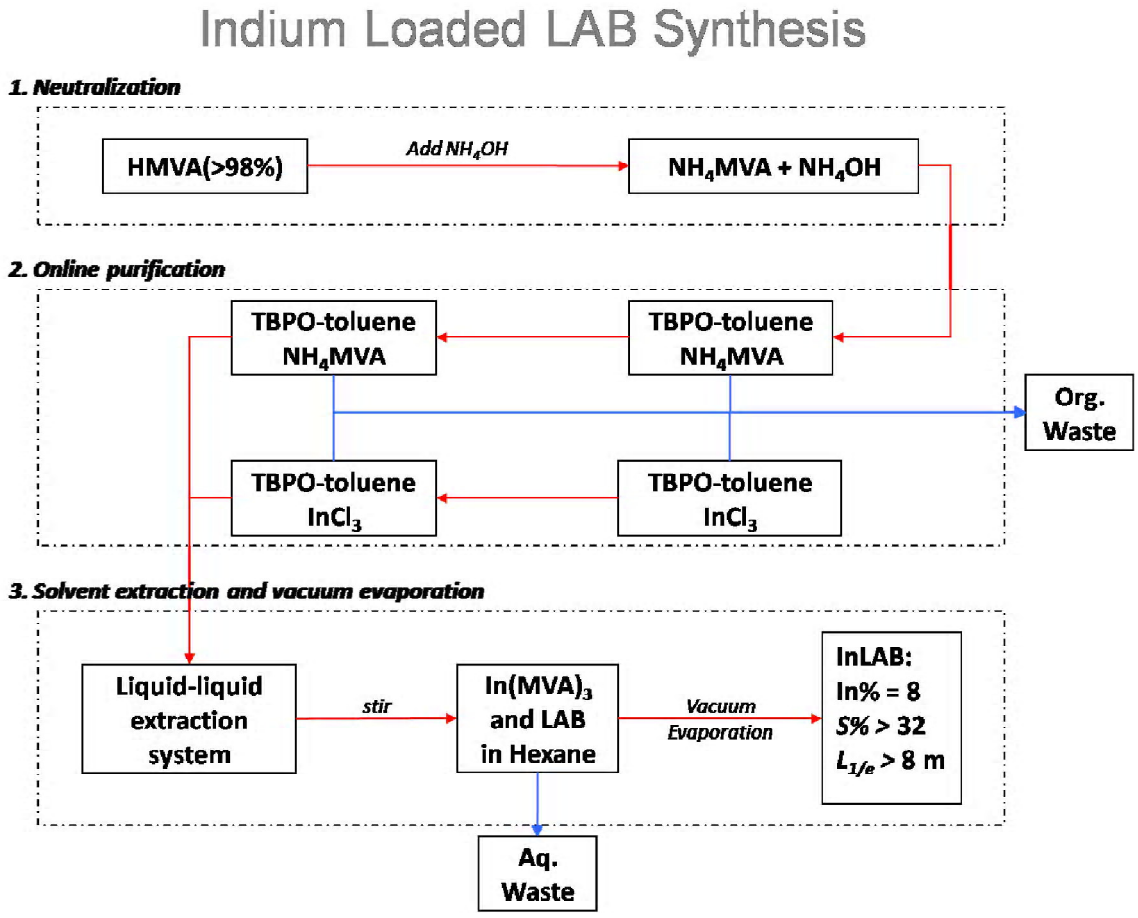

Figure 20 Schematic for Indium loaded LAB synthesis. The synthesis starts with neutralization, continues with online purification, and concludes with solvent extraction and vacuum evaporation.

3.3.4 InLAB Recipe

This section outlines the preparation of Indium loaded Linear Alkyl-Benzene (InLAB). The exact values used in this synthesis are those of sample RR016 synthesized at Virginia Tech by Steven Derek Rountree and Raju Raghavan, 50mM In. initial $L_{1/e}$ = 6.5m and $S\%_{pc}$ = 35%. Other InPC extractions are reported in Table 18 in Appendix B: Indium Liquid Scintillator Recipes.

The InLAB synthesis recipe, Figure 20, was developed using the InPC recipe from the previous section as a launching point, and has many steps in parallel with the InPC recipe from the previous section. First we start by neutralizing previously distilled HMVA. This is done by slowly adding 5.1eq NH_4OH to an immiscible solution of 3.0eq HMVA and 40eq DI water. The resulting solution is a basic aqueous solution (pH~9.85) with ions of NH_4^+ and MVA^-. The resulting solution then undergoes purification by vigorously mixing and separating it twice with equal mass of Toluene with 0.5% by weight TBPO (Toluene-TBPO). Next a solution containing 1eq $InCl_3$ is purified using Toluene-TBPO purification as above. The last solution to prepare is 40eq Hexane with 3.4eq LAB and 40eq DI water. The solution (Hexane+LAB+Water) is stirred vigorously to provide maximal surface area between the aqueous and organic solutions. The solutions containing $InCl_3$ and MVA are then added slowly (drop wise allowing the solution to clarify each time) to this Hexane, LAB and water solution. Once all the solutions have been added the solution is allowed to continue stirring for approximately an hour. The solution is then allowed to settle. We separate the aqueous and organic portions using a separation funnel. The extraction pH (aqueous portion) is measured, ~6.75. Now we have a solution of $InMVA_3$ in Hexane and LAB. The hexane in this solution is vacuum evaporated in a Rotavapor apparatus leaving $InMVA_3$ in LAB, to yield the final InLAB.

3.4 Optical Attenuation Length ($L_{1/e}$) in InLS Synthesis and Monitoring

The attenuation length $L_{1/e}$ is critical for a large volume neutrino detector. Because it is a very sensitive diagnostic we also use it as a method to monitor InLS quality, degradation and to insure quality control of materials used in the synthesis process. The value of $L_{1/e}$ is defined as the length at which the intensity of light is reduced to 1/e of the initial intensity, $I(L_{1/e}) = \frac{1}{e} I_o$, and is calculated from normalized UV-VIS absorption (abs_λ) data, Equation 6.

$$\frac{I}{I_o} = 10^{-abs_\lambda}$$

$$L_{1/e}(abs_\lambda) = \frac{1}{\ln\left(\frac{I}{I_o}\right)} \times d$$

$$L_{1/e}(abs_\lambda) = \frac{0.434}{abs_\lambda} \times d$$

Equation 6 Attenuation length as a function of absorbance. abs_λ is the absorbance of the sample at wavelength λ measured in a sample of length d.

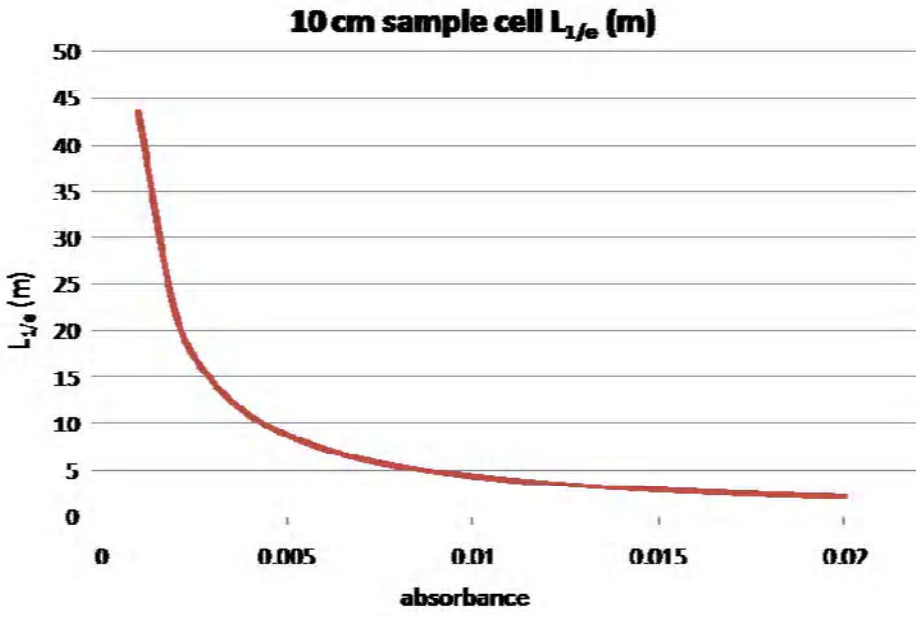

Figure 21 Attenuation length vs. absorbance in a 10 cm sample cell.

There are three methods for measuring $L_{1/e}$. The first is used by both BNL and VT, the second and third are methods used at BNL:

1) The optical absorbance, $abs_\lambda = \log\frac{I_o}{I}$, spectrum is measured using an Evolution 600 UV-Vis Spectrometer from 350 to 900 nm, using a 10cm UV glass cylindrical cell with a capacity of ~35mL of solution. The spectrum is then normalized to the minimum absorbance, Figure 22. The reason for this normalization is, the instrument is calibrated with empty cells in the reference and

sample beams then the sample cell is filled with the liquid of interest. When the absorbance spectrum is measured the change in index interface on the inside surfaces of the cell since the calibration run was taken causes the spectrum to be offset. This is corrected for by assuming the minimum absorbance is very small (abs<0.001) and normalizing it to zero. Equation 6 (plotted in Figure 21) is then used to measure the equivalent $L_{1/e}$ at 430 nm.

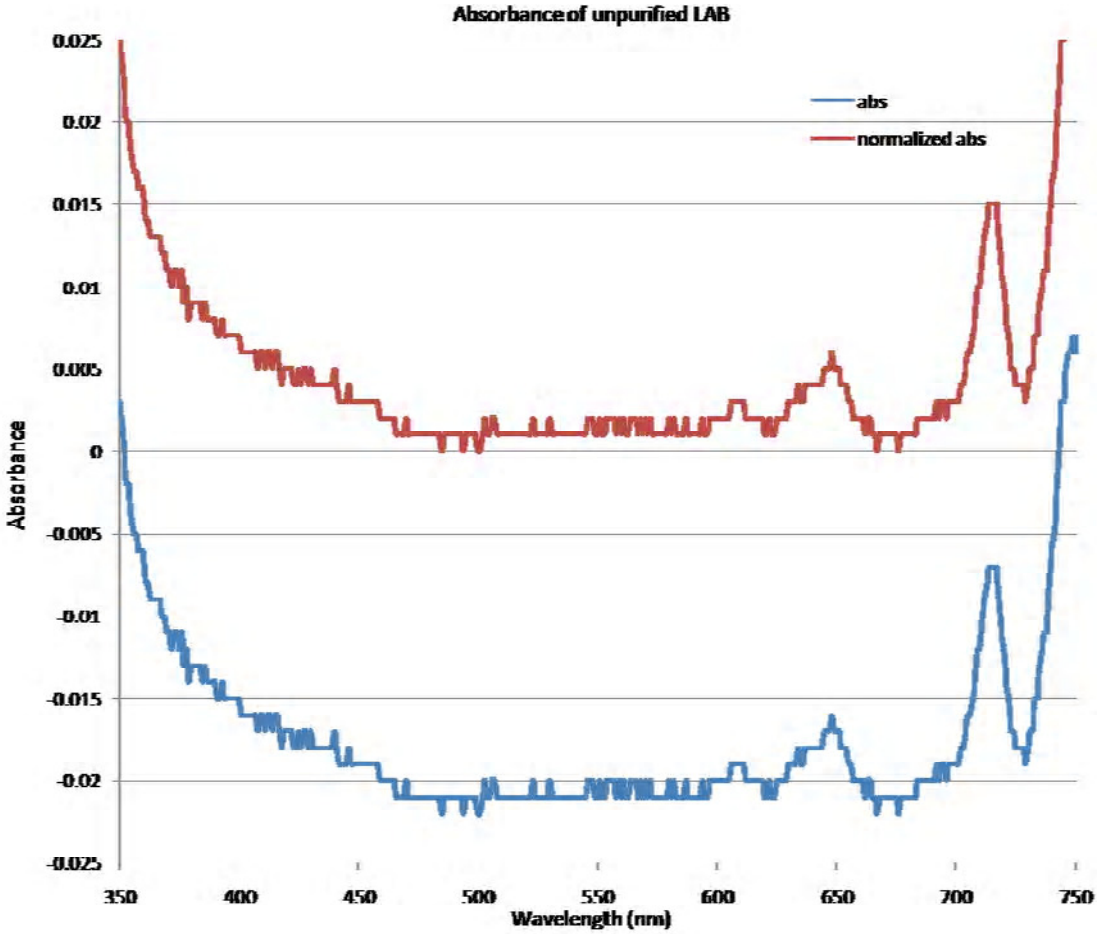

Figure 22 Absorbance of unpurified LAB before (blue) and after (red) normalization of minimum absorption.

2) A horizontal 1-m cylindrical quartz tube, 3.8 cm diameter, holds ~350mL of liquid. A 48 mW He-Cd blue (λ=442nm) laser with a neutral density filter is used to decrease the power to < 5mW is used as the light source in the apparatus. The beam is split, 80/20, into two beams 90^{o} to each other. The 80% beam passes through the 1-m sample and is then measured by a photodiode giving the

absorption in the sample. The 20% beam passes through an air filled 10cm cell and is measured by a second photodiode giving the fluctuations in the beam intensity. The results of this system agree with the attenuation length extrapolated from the UV-Vis Spectrometer measurement (at the time a Shimadzu UV-1601 Spectrometer). [59]

3) To further reduce the systematic error a vertical 2-m cylindrical quartz tube, 2.5 cm diameter (1.3L capacity), system is in the final stages of testing at BNL. This system uses pulsed LED beams with selected wavelengths from 350 to 700nm. These beams are split, 50/50. One beam passes through the sample and is measured by a PMT while the other beam passes through a fiber, creating an ~200ns delay and is then measured by the PMT. The vertical path length allows for measurements at varying thicknesses of liquid giving us the capability to test if the transmitted light verses path length in sample liquid is a simple exponential. [59]

The first of these methods will be used to monitor scintillator degradation while the third method will be used to measure absolute values of $L_{1/e}$.

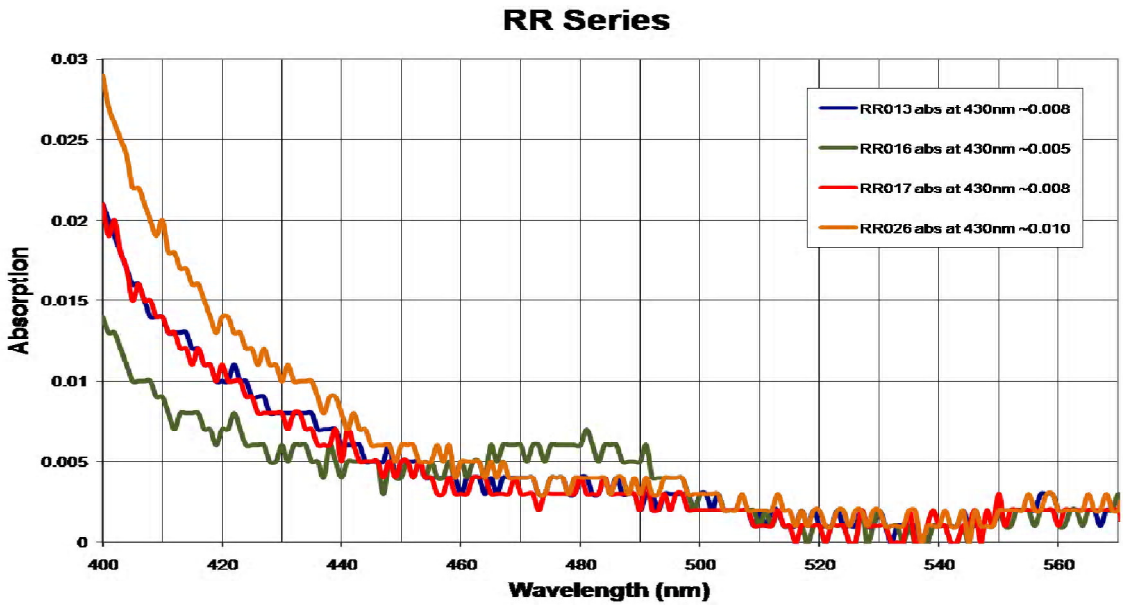

Figure 23 Select InLAB spectrums from the RR*XXX* series taken with an Evolution 500 Spectrometer shortly after synthesis. The absorption at 430nm is reported in the legend for each sample.

3.5 Light Yield (S%) Measurements

We measure the photon production or light yield (S%) of liquids via a photo multiplier tube (PMT) optically coupled to an acrylic sample holder that is wrapped with high reflective foil. There is a bore hole in the acrylic sample holder for a 10 mL scintillation vial. This system is referred to as the S% counting system. The S% counting system containing a sample and a ^{137}Cs source is placed in a lead housing with ~5cm thick lead walls to block out surrounding radioactive backgrounds.

We determine the light yield by comparing the Compton spectrum of pure PC with 3g/L PPO and 15mg/L bis-MSB to

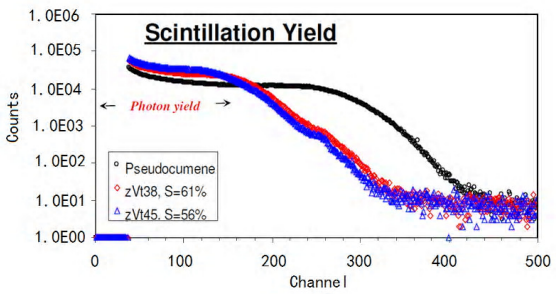

Figure 24 Select InPC compton spectrums from zVt*XX* series using a 137Cs sourc.

Figure 25 S% measurement system at VT. Lead housing, PMT with acrylic sample holder, and ^{137}Cs source.

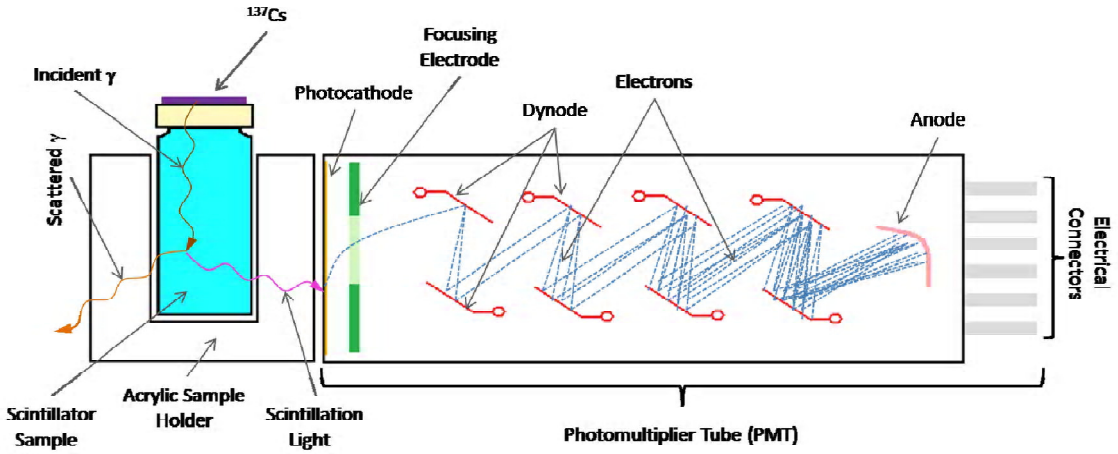

Figure 26 Light Yield Measurement Schematic. Only one ray is shown for scintillation light. In reality many scintillation photons are produced. An acrylic sample holder is optically coupled to a PMT and a sample cell. A ^{137}Cs source is placed on top of this sample. Gamma rays from the source Compton scatter in the scintillator producing scintillation light which is detected by the PMT, giving a Compton spectrum. Two Compton spectrums can then be compared to give a percent light yield (%S) of one versus the other. The standard we compare InLS to is pure PC giving a $\%S_{PC}$.

the Compton spectrum of our sample. The light yield is expressed as $S\%_{PC}$; the ratio of the pulse height of the Compton edge of the sample to the Compton edge observed in a pure PC measurement, Figure 24. InLS samples are prepared in a 10mL sample scintillation vial by adding $3g/L_{InLS}$ PPO and $15mg/L_{InLS}$ bis-MSB dissolved in 0.25mL PC. The precise method for loading the flours is as follows. A concentrated solution of $600mg/L_{PC}$ bis-MSB is made. The bis-MSB takes a few days of stirring to dissolve completely. When ready to make a scintillation sample, 0.25mL of this solution is placed in a scintillation vial and 0.03g of PPO is added and swirled around. Ounce all of the PPO is dissolved the remaining (~9.25mL) portion of the vial is filled with the sample to be measured.

3.6 Investigation of 480nm Light Absorption Contaminant in InLAB

This section addresses a problem that occurred during InLAB development and previously at many InPC measurements at Bell Labs. We began a program to reproduce promising InLAB samples from the initial work in the RR*XXX* InLAB series to gain statistical data concerning these samples. An abnormality was observed at the beginning of this program—we started observing a bump at ~480nm, Figure 27, in our UV-Vis spectrums for samples that were made following the RR012 sample from the initial InLAB development. This bump at 480nm had been observed before at Bell Labs and BNL before Toluene-TBPO methods had been developed for purifying the NH_4MVA

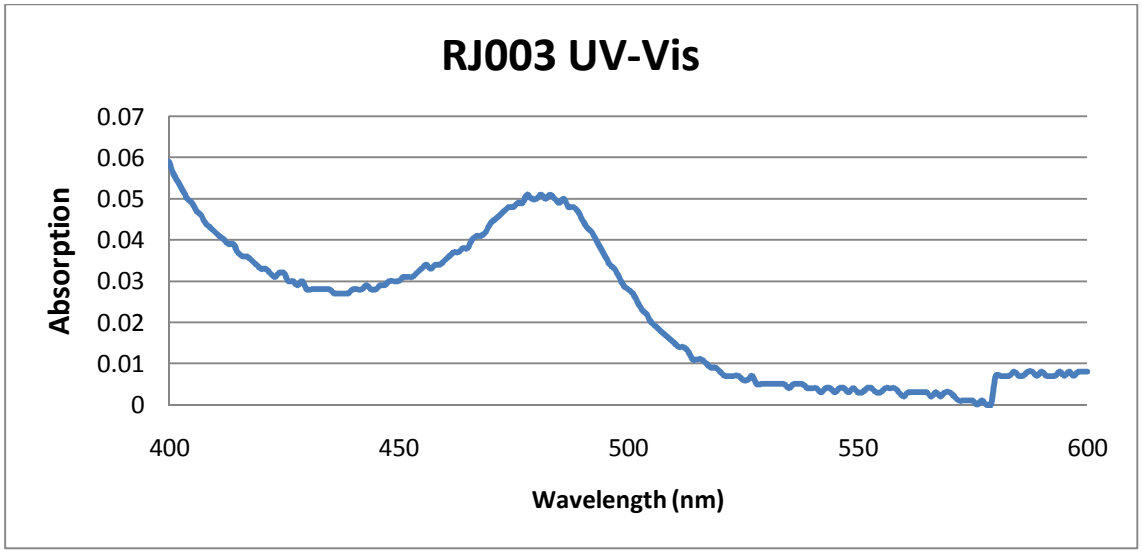

Figure 27 Observation of 480nm "bump" in InLAB UV-Vis spectrum, RJ003 sample-- following the same procedure as RR012 sample.

solution. And, in fact the invention of the Toluene-TBPO purification step at Bell Labs was to get rid of this, [55] but the bump returned years later during continued work at Virginia Tech with InLAB. This lead to a series of investigations to explain the abnormality, the synthesis series is labeled RJXXX.

3.6.1 Test for 480nm "bump" Removal

In an attempt to see if the 480nm "bump" was a problem with this one synthesis, we synthesized four InLAB samples based on the RR012 sample recipe from initial InLAB development which follows the recipe from 3.3.4 InLAB Recipe. The details of the synthesis are listed in, Table 4. All four samples had the characteristic bump at 480nm shown in, Figure 27, in their UV-Vis spectrums.

We then investigated the possibility that the 480nm bump could be a property of the RR012 sample recipe that RJ001-003 and RJ005 were based on. We chose another of the promising recipes from the initial InLAB work, RR016, and made four samples using this recipe (RJ006 failed due to an attempt to raise the extraction

	Model	Samples			
Ingredient (g)	RR012	RJ001	RJ002	RJ003	RJ005
HMVA	34.84	34.86	34.87	34.81	34.81
DI H_2O	70	70.11	70.24	70.14	70.15
HN_4OH	19.94	19.94	20.04	20.03	20.03
HEXANE	200	205.3	201.47	200.8	200.43
LAB	96	96	95.78	95.89	95.94
InCl	45.24	45.69	45.29	45.23	45.24
pH_1	9.06	8.91	8.7	8.57	8.75
pH_2	5.34	4.27	4.16	4.21	4.56
Density (g/ml)	0.955	0.9382	0.954	0.9552	0.944

	Model	Samples			
Ingredient (g)	RR016	RJ004	RJ006	RJ007	RJ008
HMVA	34.84	34.85	34.88	34.83	34.84
DI H_2O	70	70.03	70.03	70.08	70.03
HN_4OH	24.61	24.63	24.64	24.65	24.62
HEXANE	200	200.39	200.13	190	200.87
LAB	98	97.7	97.96	97.71	97.99
InCl	45.32	45.31	45.35	45.34	45.36
pH_1	9.16	9.37	9.71	9.49	9.57
pH_2	5.56	5.58	FAILED	5.55	6.15
Density (g/ml)	0.952	0.9496	FAILED	0.9513	0.948

Table 4 Preliminary investigation of InLAB spectral bump at 480nm. The tables lists the ingredients of the synthesis in grams, pH1, pH2, and the InLAB density. The top table are sample following the initial InLAB work's sample RR012 recipe, and the bottom follows RR016.

pH, pH_2, by adding NH_4OH after the extraction was complete). The three successful samples all showed the same bump at 480nm. This led us to believe the 480nm bump could not be blamed on the recipe or a single synthesis irregularity.

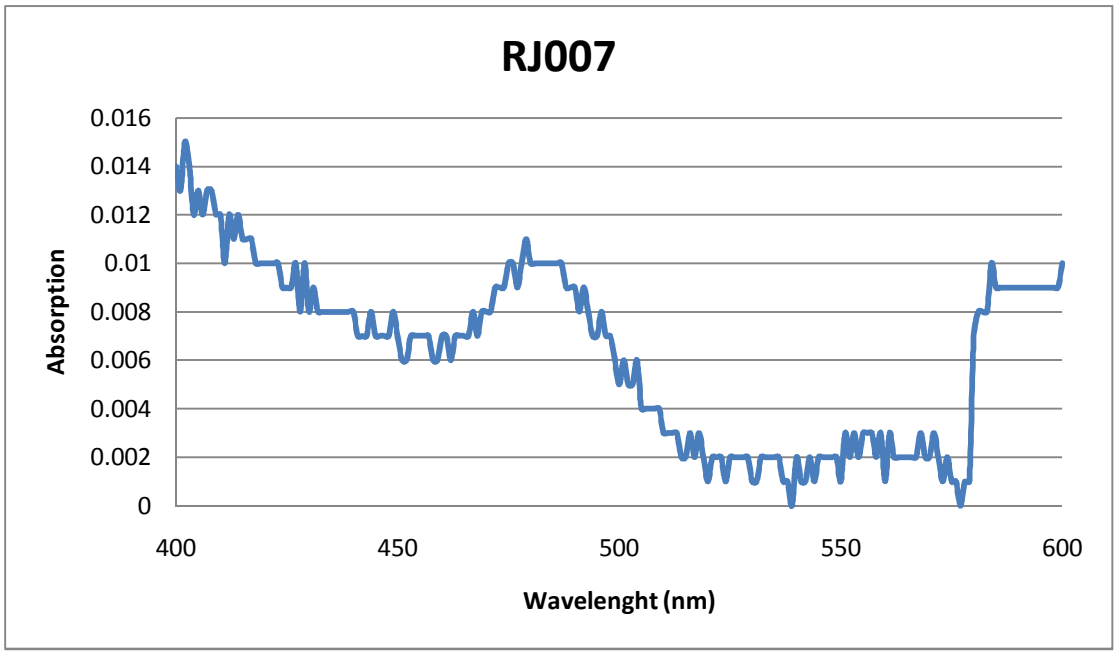

Figure 28 Observation of 480nm "bump" in InLAB UV-Vis spectrum, RJ007 sample-- following the same procedure as RR016 sample.

3.6.2 Investigating Absorption of Front-End Synthesis Components

In order to find the 480nm bump origin we began looking at the spectrums of the chemicals and their purity we used in the InLAB synthesis process, Figure 29-Figure 32. None of these spectra had a significant absorption in the 480nm range that would lead us to believe it was problematic; therefore, we concluded that the 480nm bump occurred due to some unexpected chemical process in the liquid-liquid extraction or some contaminate introduced by $InCl_3$.

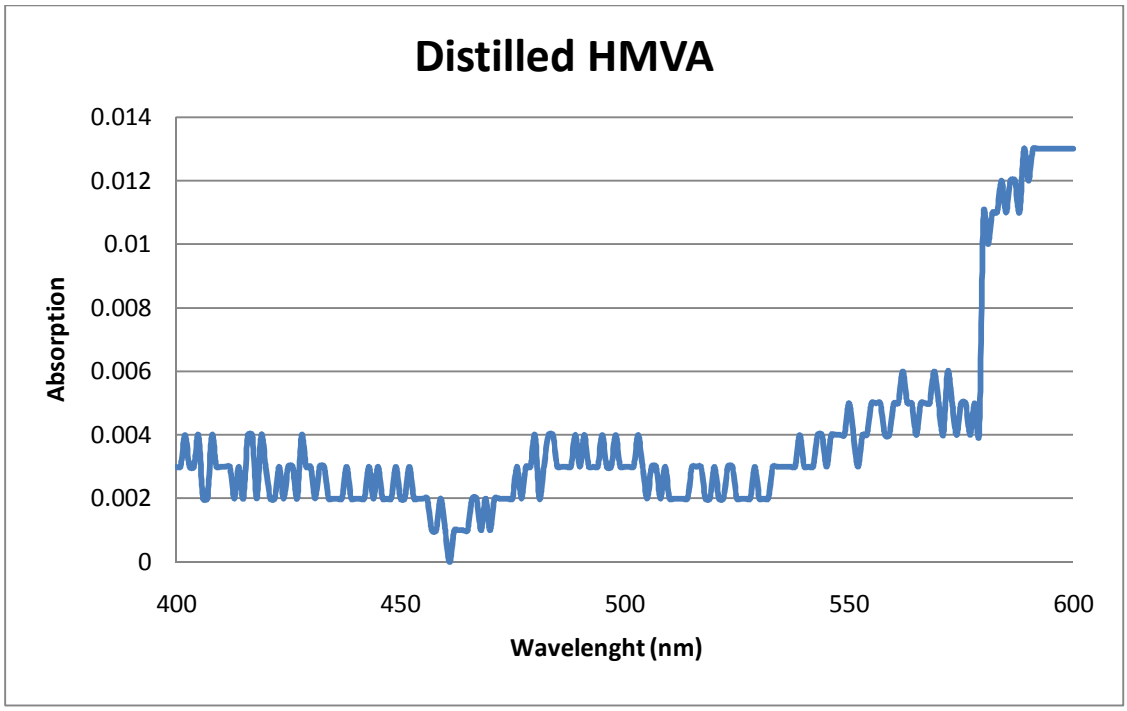

Figure 29 Distilled HMVA UV-Vis spectrum from Distilled HMVA used in the search for a spectral bump in InLAB at 430nm. No significant absorption at 480nm is observed.

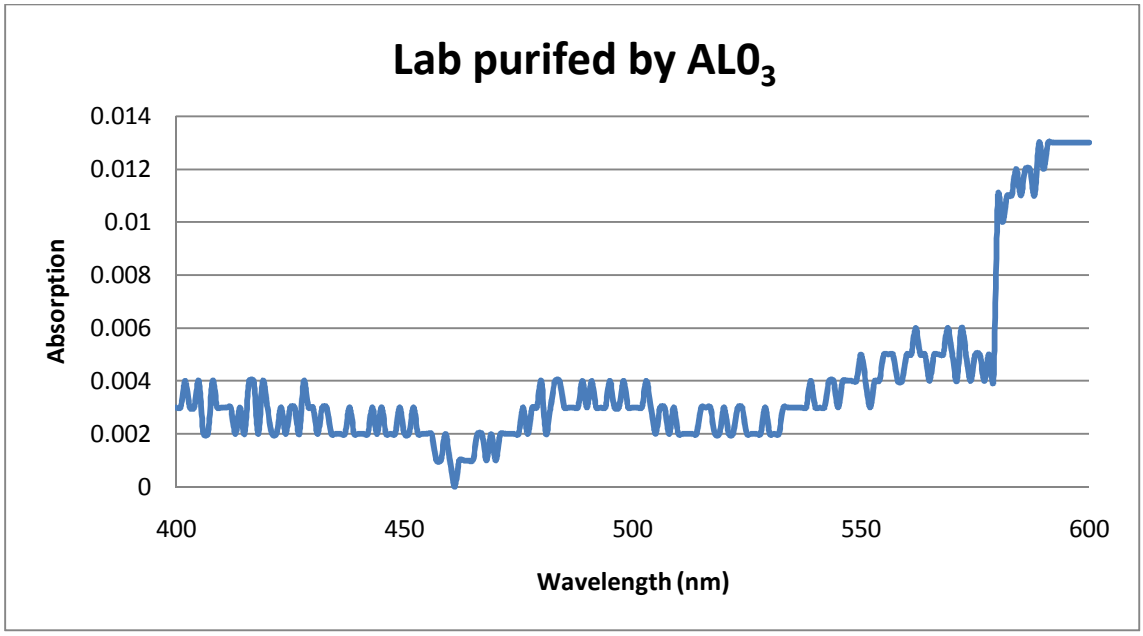

Figure 30 LAB UV-Vis spectrum of LAB passed through an AlO_3 column used in the search for a spectral bump in InLAB at 430nm. No significant absorption at 480nm is observed.

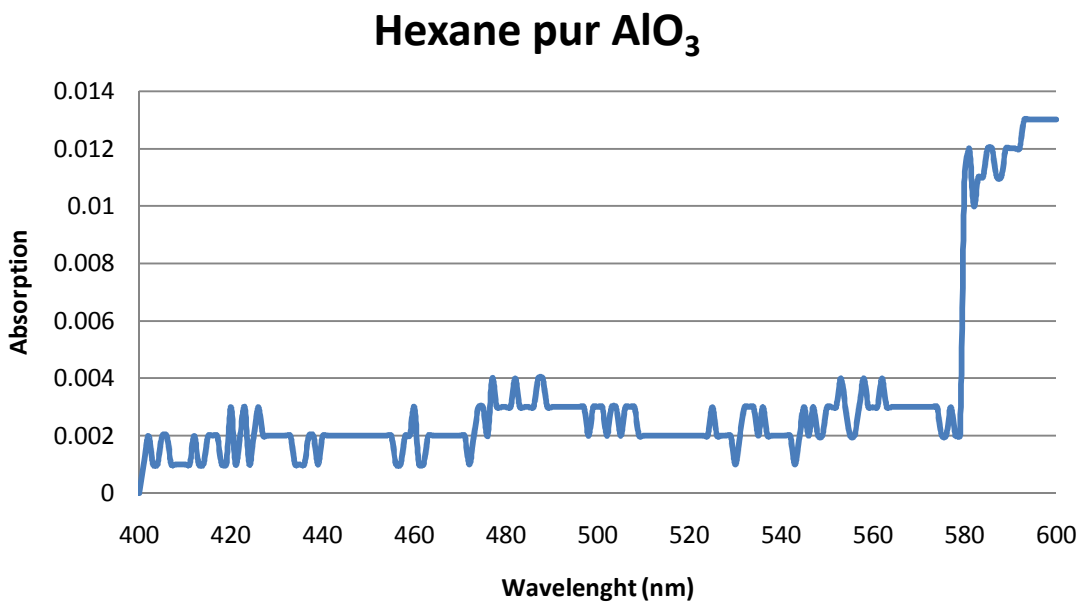

Figure 31 Hexane UV-Vis spectrum of Hexane passed through an AlO_3 column used in the search for a spectral bump in InLAB at 430nm. No significant absorption at 480nm is observed.

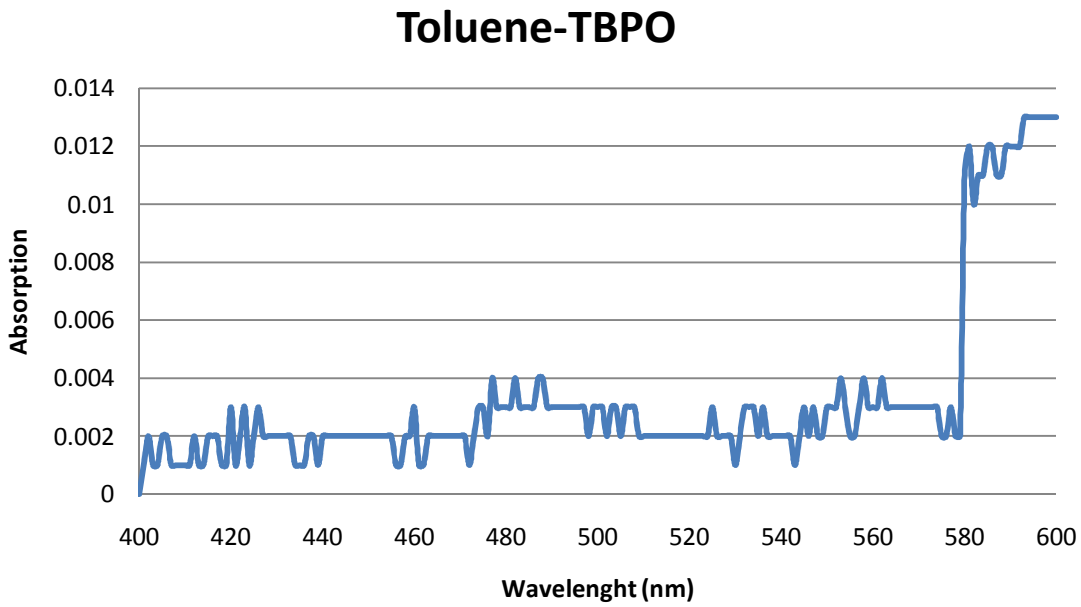

Figure 32 Toluene-TBPO UV-Vis spectrum of Toluene-TBPO used in the search for a spectral bump in InLAB at 430nm. No significant absorption at 480nm is observed.

3.6.3 Investigating Possible Contamination of $InCl_3$ that May Lead to 480nm Bump

The results from the previous section led us to believe the 480nm bump was introduced by our $InCl_3$ solution we thus undertook investigate the origin of a 480nm bump arising from $InCl_3$. The parameters of these experiments are listed in Table 5.

	Model	Samples				
Ingredient (g)	RR016	RJ009	RJ010	RJ011	RJ012	RJ013
HMVA	34.84	34.86	34.85	34.84	34.83	34.83
DI H2O	70	70.01	70.05	71.55	70.08	70.04
NH4OH	24.61	24.63	24.62	24.77	24.58	24.66
HEXANE	200	200.29	201.5	164	173.6	203.6
LAB	98	97.98	97.94	89.14	96.15	45.4
InCl	45.32	0	45.35 (HCL)	55.67	45.33	91.11
pH(1)	9.16	9.65	N/A	9.59	9.55	9.52
pH(2)	5.56	9.67	7.06	4.23	5.77	5.83
Density (g/ml)	0.952	N/A	N/A	0.937	0.932	0.923

Table 5 Parameters from investigating liquid-liquid extraction process and possible contamination of InCl3 that may lead to 480nm bump. The table lists the ingredients of the synthesis in grams, pH1, pH2, and the InLAB density.

The first of these was to run a synthesis following the RR016 recipe, but leave out the $InCl_3$ from the synthesis, sample RJ009. If there was contamination being introduced by the neutralization and purification of HMVA we would expect this synthesis to show the characteristic bump at 480nm in the UV-Vis spectrum. No bump was observed, Figure 33. Next we investigated the introduction of MVA into LAB during the extraction by replacing $InCl_3$ with HCl acid, sample RJ010. This simply extracts HMVA into the LAB scintillator. Again, no bump at 480nm was observed in the UV-Vis spectrum, Figure 34. Clearly the experiments lead to $InCl_3$ being the root of the 430nm bump.

Finally we attempt to extract any impurities from $InCl_3$ that may be having adverse effects on our InLAB sample. We use the same purification method as is used in purifying the NH_4OH + HMVA solution, twice Toluene-TBPO purification. Following

the recipe for RR012 with the addition of Toluene-TBPO purification of $InCl_3$ we obtain an InLAB sample, RJ011, with a vastly reduced absorption at 480nm, Figure 35.

To check the results of RJ011 we synthesize two more samples RJ012 and RJ013 without and with Toluene-TBPO purification respectively. The bump reappears in RR012 as expected, and is minimal in RJ013.

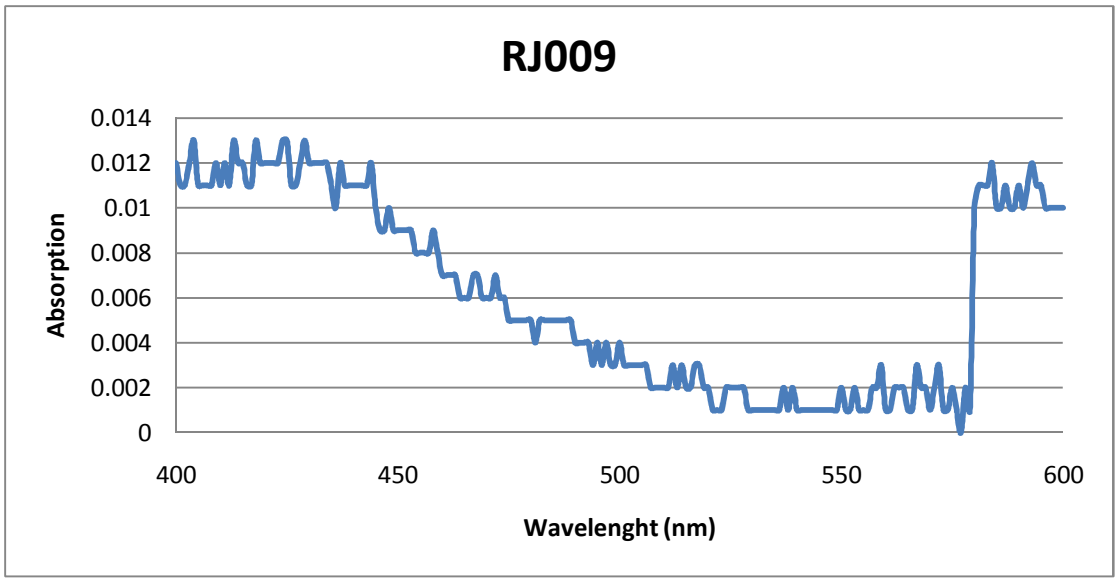

Figure 33 UV-Vis spectrum from InLAB synthesis leaving out $InCl_3$. Note, the final solution does not actually contain Indium as we left out $InCl_3$ from the recipe. No bump was observed at 480nm.

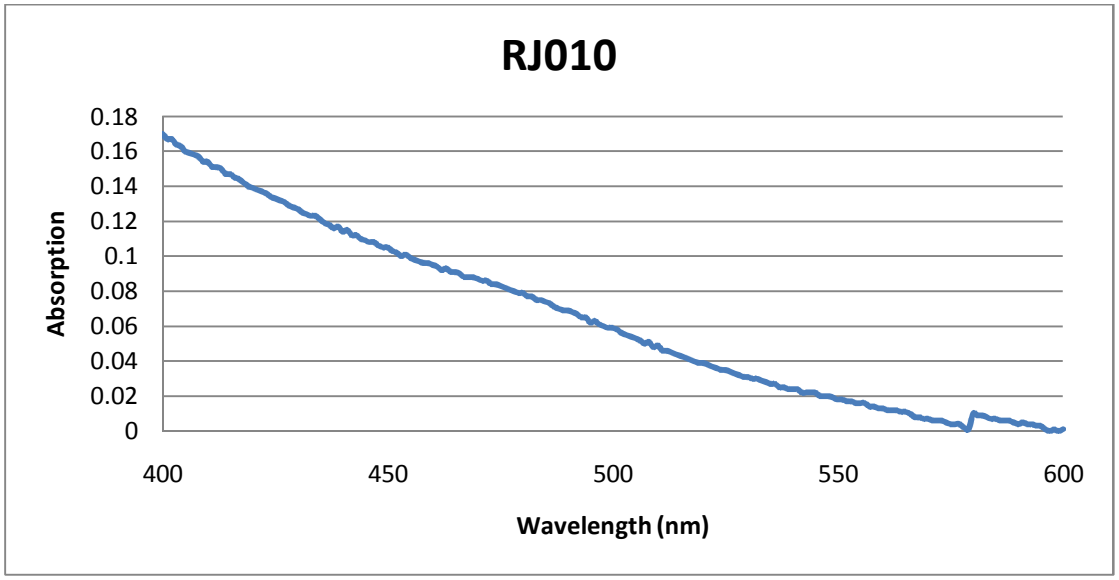

Figure 34 UV-Vis spectrum from InLAB synthesis replacing InCl3 with HCl acid. The HCl acid was used to extract HMVA back into the organic phase. Note, the final solution does not actually contain Indium as we left out InCl3 from the recipe. No bump was observed at 480nm.

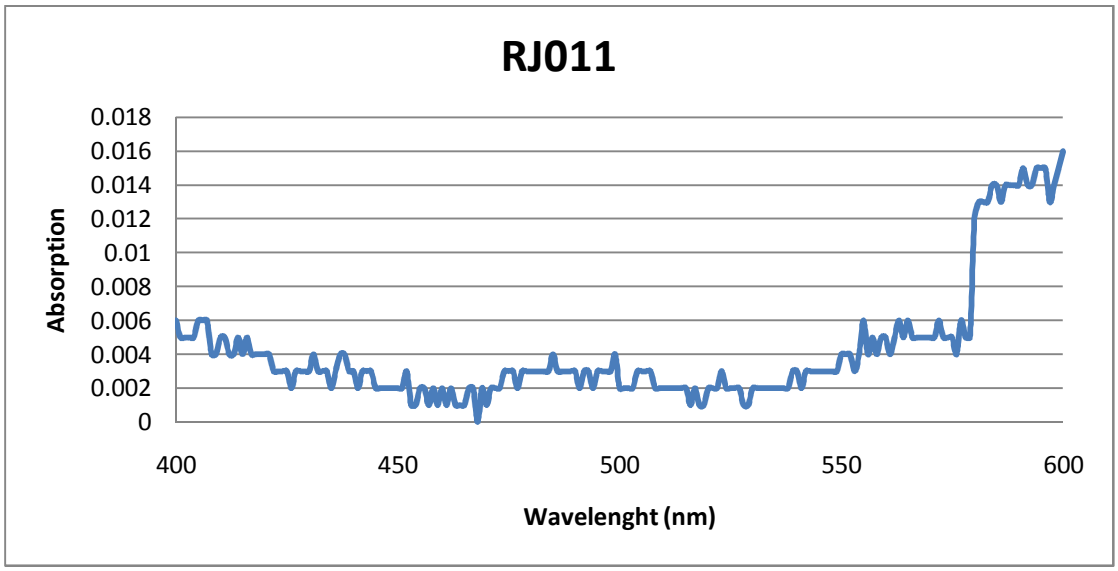

Figure 35 UV-Vis spectrum of an InLAB sample using the recipe for RR012 with the addition of twice purification of the $InCl_3$ using Toluene-TBPO. The 480nm bump is drastically reduced.

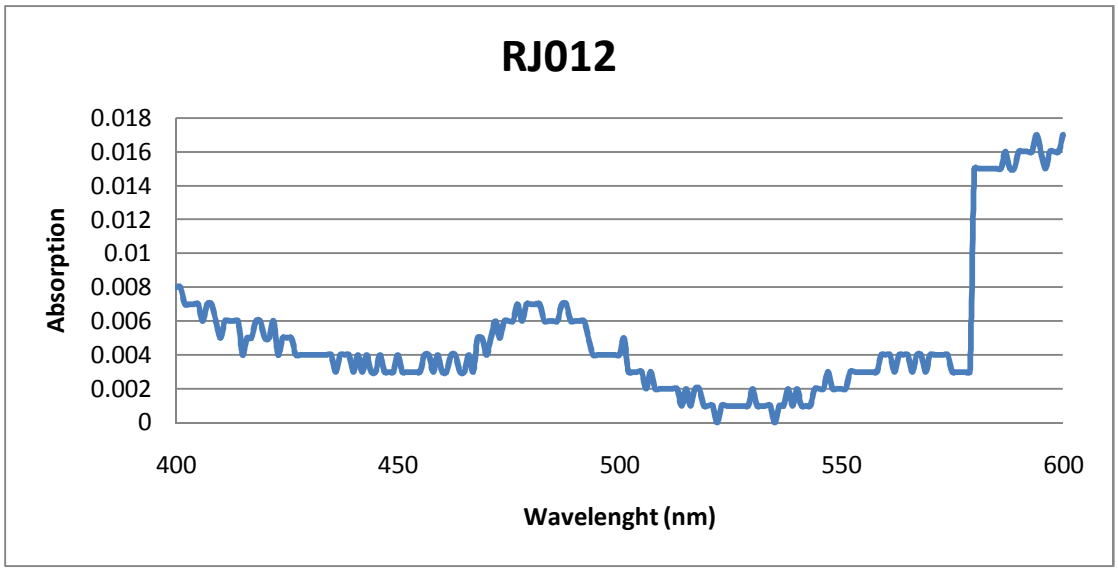

Figure 36 UV-Vis spectrum of an InLAB sample using the same recipe as RJ011, but leaving out the twice Toluene-TBPO purification of $InCL_3$. The 480nm bump reappears.

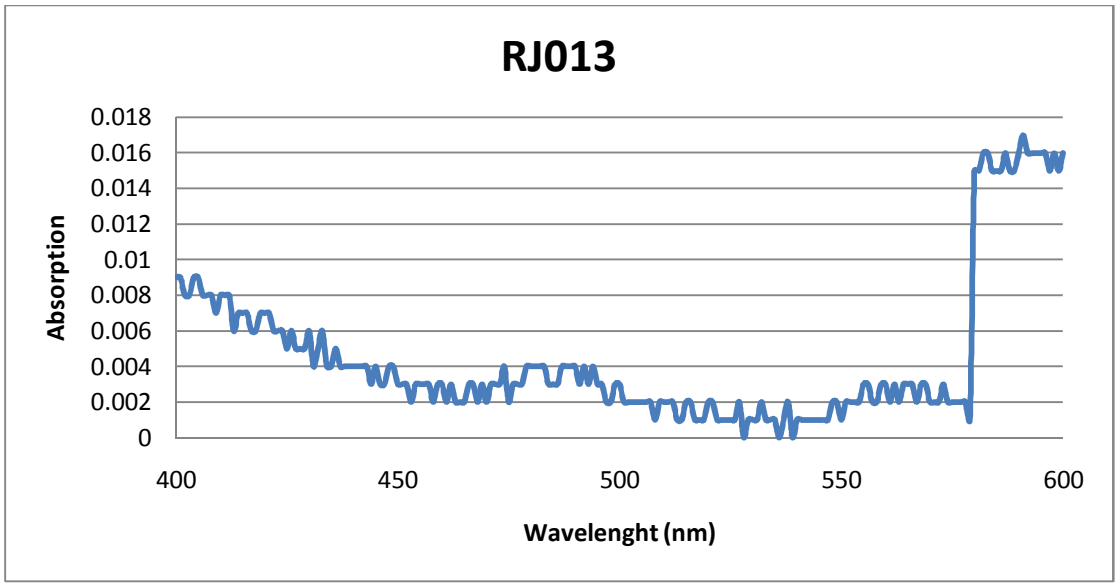

Figure 37 UV-Vis spectrum of an InLAB sample using the recipe for RR012 with the addition of twice purification of the InCl3 using Toluene-TBPO (repeat of RJ011). The 480nm bump is drastically reduced.

3.6.4 Conclusions of 480nm bump in InLAB investigation

We found that the randomly occurring bump at 480nm is a result of contaminated $InCl_3$ that can be removed by solvent extraction of $InCl_3$ using Toluene-TBPO. The origin of the contamination is unknown, but a possibility discussed is leaching of organic compounds from the bottles in which our $InCl_3$ solution is stored. Unlike previous work, the solution of $InCl_3$ used here was taken from a stockpile of $InCl_3$ solutions that had been stored for more than 24 months in plastic (LDPE) bottles in a closed box (Note: the age of the $InCl_3$ used in the RRXXX series, which yielded a small absorbance bump at 480nm, was of the same age; however, it had been partially used when it was new). Recently these results were discussed in the LENS Scintillator Group Meeting at BNL. [64] Discussions in those proceedings concluded that this contamination from $InCl_3$ should be looked into again by means of GC-MS analysis of our $InCl_3$ solution and InLAB scintillators (MS only) that exhibit this bump at 480nm.

3.7 Current endeavors in InLS

From preliminary work with InLAB, VT and BNL have concluded a large portion of InLAB degradation with time is due to oxidization of free HMVA in the scintillator.

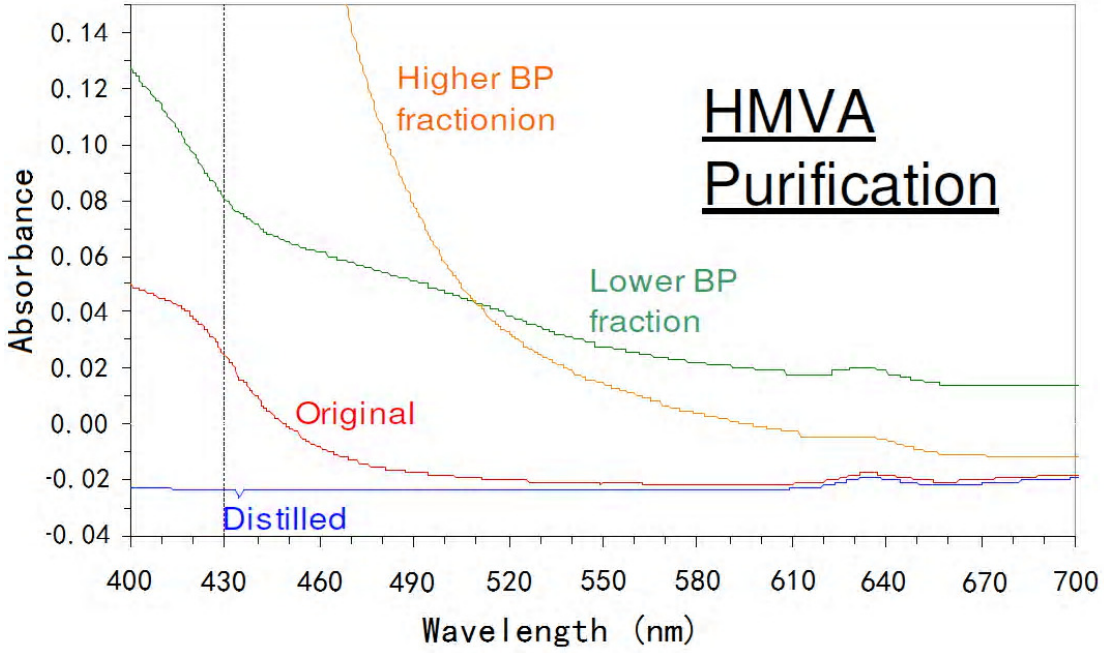

Figure 38HMVA Purification.

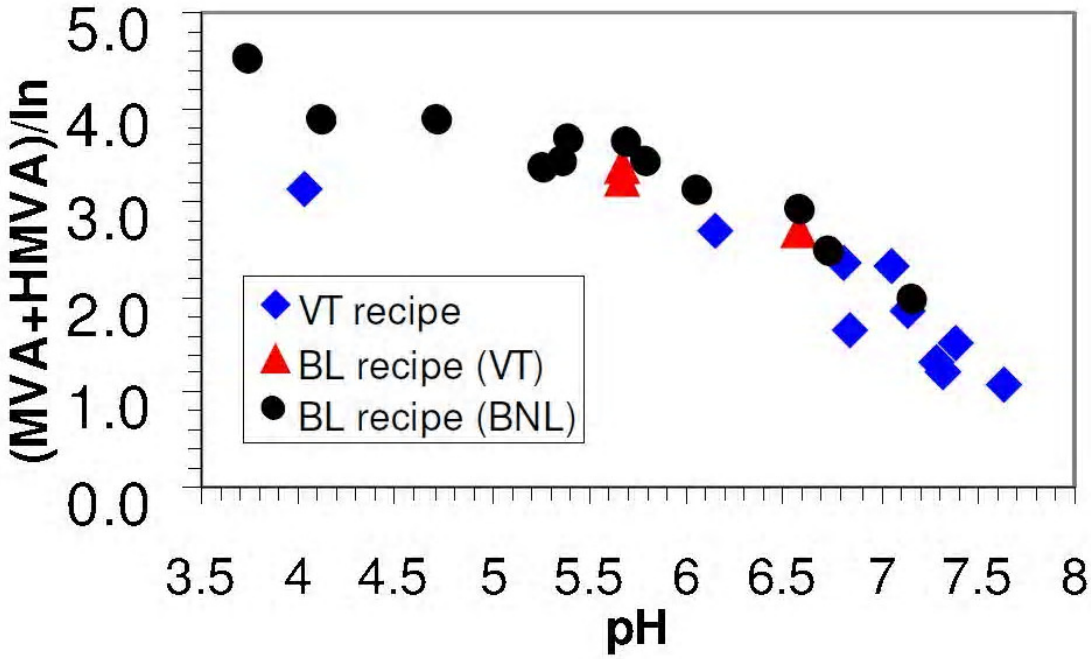

Figure 39 Measurement of (MVA+HMVA)/In in InPC samples.

Figure 38, shows absorbance spectra for HMVA as delivered from the supplier and the spectra of the three distillation fractions. As distilled HMVA ages in a closed bottle with atmospheric gas, the absorption spectra degrades to that of the pre-distillation spectra. This means that if InLS has free HMVA in it, it too will degrade with a similar time scale. This was observed in RRXXX series after ~2 months the $L_{1/e}$ from 8m to 2m, and the HMVA used in that series showed similar degradation. An additional argument that free HMVA is the culprit of $L_{1/e}$ degradation is shown by data in Figure 39 a measurement of the (MVA+HMVA) per Indium for InPC samples. Those samples produce at Virginia Tech with extraction pH~6.5 to 7 (low concentration of free HMVA) showed an initial drop in $L_{1/e}$ from ~12m to 8m over the course of 2 months, and then stabilized at 8m for over 9 months. The slight degradation is believed to be from a very small amount of free HMVA which once oxidized stops contributing to $L_{1/e}$ degradation. Decreasing the (MVA+HMVA) per Indium is beneficial for $S\%_{PC}$ as well due to the increased density of aromatic compounds. InLAB extractions attempting to reach these higher pH at Virginia Tech have failed; therefore, another approach to reducing $L_{1/e}$ degradation must be taken. Even in InPC, going to higher extraction pH leads to increased OH^- in the In(III) compounds. These compounds are subject to polymerization and creating them should be avoided due to larger molecules precipitating out of solution.

Both BNL and VT are attempting to rid the free HMVA degradation problem. VT is creating a nearly anaerobic system (non critical components are purified then loaded into the system while critical components are purified anaerobically and loaded anaerobically into the system) flushed with argon gas to eliminate the oxidization of free HMVA, and BNL is attempting to remove the free HMVA post synthesis by "washing" the InLAB with fine tuned pH water. Both methods seem promising, and the final synthesis will likely encompass both, anaerobic InLAB synthesis and post synthesis anaerobic tuned water "washing."

3.7.1 Closed System Small Scale InLAB Factory

At VT we constructed a closed system to synthesize InLAB to eliminate oxidization of free acid in the synthesis. The major components are vacuum distillation

system with reservoir for distilled HMVA, neutralization chamber, liquid-liquid extraction chamber, and Hexane evaporation system.

The vacuum distillation system is shown in Figure 40. The three reservoirs for raw HMVA, distilled HMVA and distillation waste are continuously purged with argon, and vent to a one way trap designed so that atmospheric gasses cannot flow into the

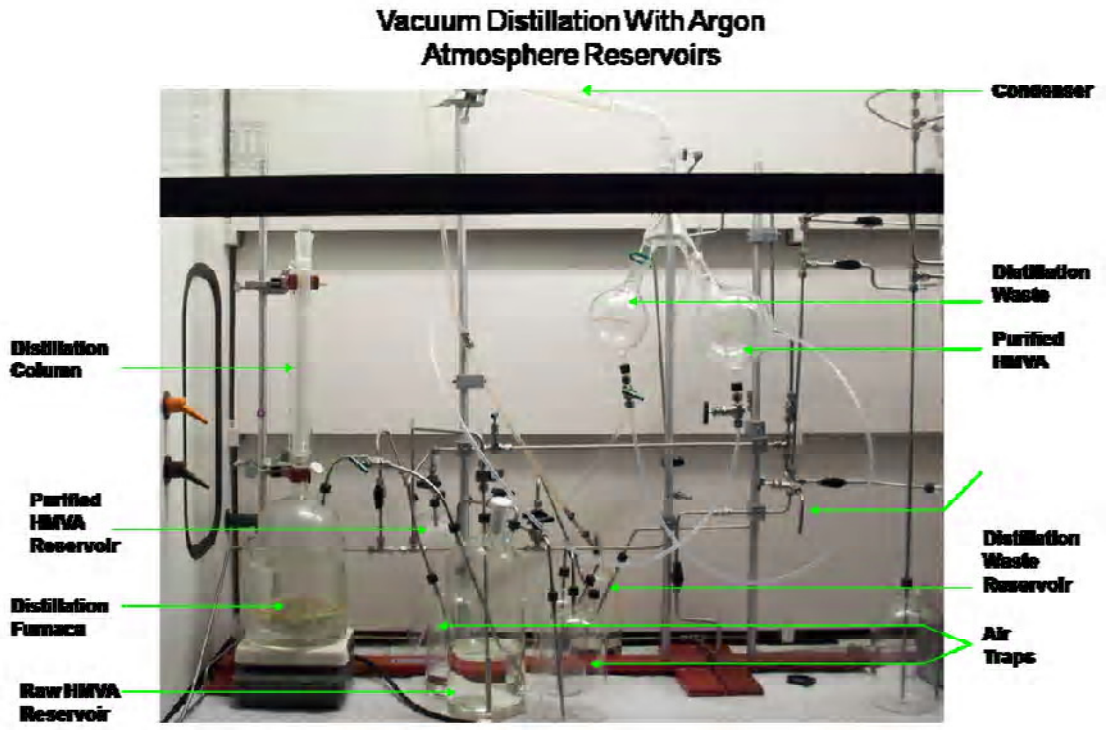

Figure 40 Vacuum Distillation system with Argon Atmosphere Reservoir. This system contains a distillation furnace heated via a hotplate, a column packed with Teflon coils, a condenser, and collection flasks for low boiling point fraction and distilled HMVA, as well as a reservoir for holding up to 4L of distilled HMVA in an argon atmosphere.

reservoirs. Once the low boiling point fraction is collected (~5% of the raw HMVA volume), the bulbs for distillation waste and distilled HMVA are rotated such that the distilled product drips into the distilled HMVA bulb. Once this bulb has reached maximum capacity the vacuum line is shut off, and the argon line is opened allowing argon to flush the system. Once atmospheric pressure is reach, valves to drain the distilled and waste HMVA bulbs are opened, and the liquids flow into their respective reservoirs. Valves can then be reset to their prior positions and the distillation continued till ~5% of the original volume remains in the distillation furnace.

After distillation, distilled HMVA from the distilled HMVA reservoir, Figure 40, is sampled by closing the reservoir vent, and opening the sample spout valve. A UV-Vis spectrum is taken of the sample. If the UV-Vis spectrum passes our quality control (QC)

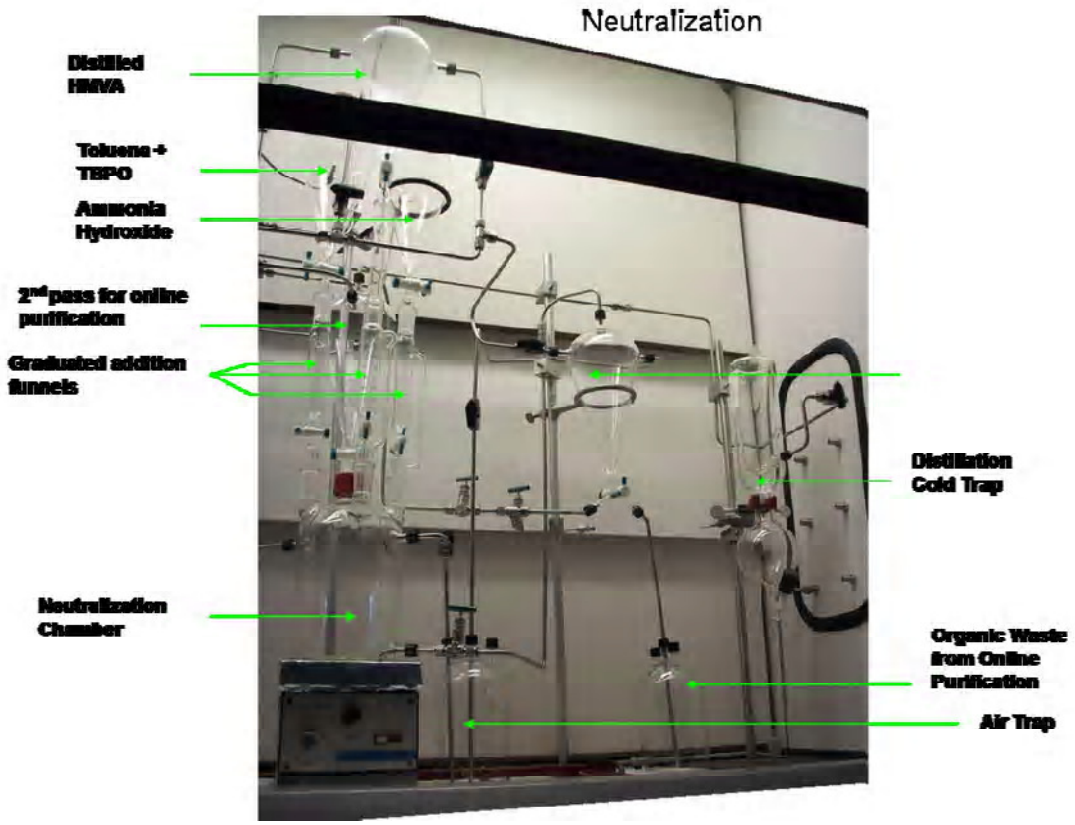

Figure 41 Neutralization Chamber System— this system contains a vessel for neutralization of HMVA with NH_4OH, four squibb funnels that are attached to addition funnels allowing volume controlled addition of NH_4OH, Toluene-TBPO, distilled HMVA, 2^{nd} pass NH_4OH HMVA purification to the neutralization chamber, and a separation funnel to separate aqueous and organic phases after purification. All vessels contain a common argon line and vent line to a one way trap with the exception of the NH_4OH funnel which has its own vent line due to initial system tests which showed ammonia gas migration into the other funnels.

measures, absorption < 0.005 at 430nm in a 10cm (further QC definitions are being considered), then the distilled HMVA is pumped into the distilled HMVA funnel of the neutralization chamber system, Figure 41. The neutralization chamber system contains a vessel for neutralization of HMVA with NH_4OH, four squibb funnels with argon purge and vent lines are attached to addition funnels allowing volume controlled addition of NH_4OH, Toluene-TBPO, distilled HMVA, and 2^{nd} pass NH_4OH+HMVA purification to the neutralization chamber. HMVA is neutralized with NH_4OH, and the pH is monitored via a pH probe port in the bottom of the neutralization chamber. After neutralization and

the first Toluene-TBPO purification the solution goes into a separatory funnel which allows the aqueous portion to be loaded into the 2nd pass online purification funnel, purified via Toluene-TBPO purification a 2nd time, and separated again, this time loading the solution into the neutralized HMVA funnel of the liquid-liquid extraction system, Figure 42 (during both separations, the organic phase is discarded). All vessels contain a common argon line and vent line to a one way trap with the exception of the NH_4OH funnel which has its own vent line due to initial system tests which showed ammonia gas migration into the other funnels.

Now that distilled, neutralized, and purified HMVA has reached the HMVA funnel of the liquid-liquid extraction system, Figure 42, indium can be extracted into an organic liquid. The liquid-liquid extraction system much like the neutralization system contains a vessel for liquid-liquid extraction with a pH probe port at the bottom, four squibb attached to addition funnels allowing volume controlled addition of NH_4OH+HMVA, $InCl_3$, Hexane, and LAB, and a separation funnel to separate organic and liquid phases. Unlike the neutralization system, the aqueous portion of the liquid-liquid extraction is the waste product, and the organic portion is loaded into the Hexane evaporation system, Figure 43. All vessels contain a common argon line and vent line to a one way trap.

Once a solution of InLAB+Hexane is produced in the liquid-liquid extraction system, the solution is separated from the aqueous waste of that system, and pumped into the Hexane evaporation system. This system contains a rotovapor for hexane evaporation and a condenser to reclaim the evaporated hexane which can be recycled in the system. The final product is InLAB synthesized in an oxygen free environment.

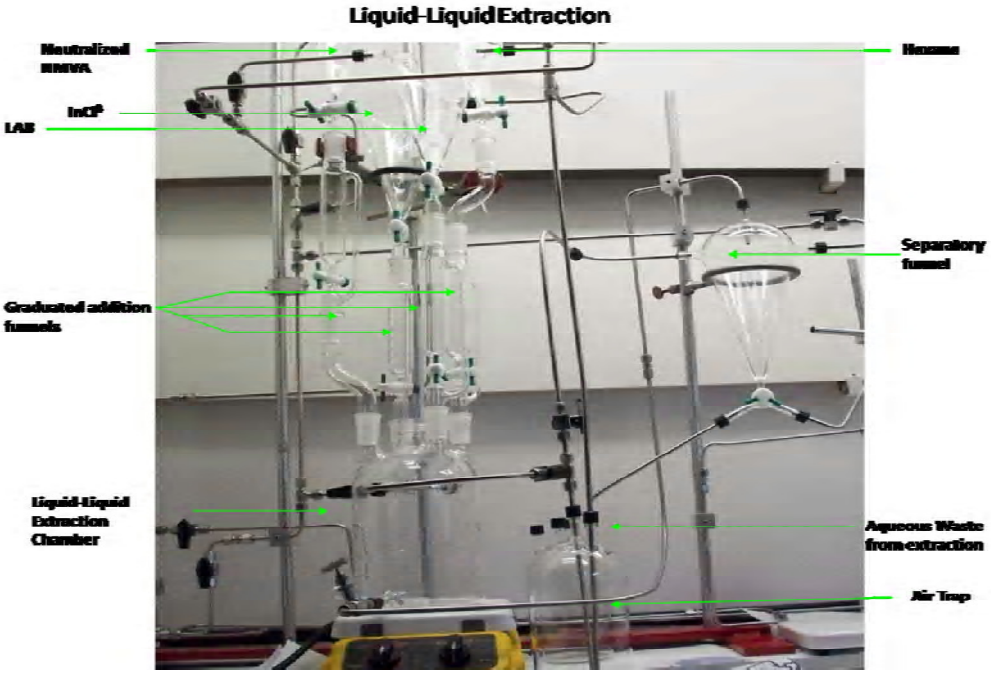

Figure 42 Liquid-Liquid Extraction Chamber System— this system contains a vessel for $InHMVA_3$ into Hexane and LAB, four squibb funnels that are attached to addition funnels allowing volume controlled addition of neutralized HMVA, $InCl_3$ (pre purified with Toluene-TBPO), LAB, and Hexane, and a separation funnel for separating organic and aqueous phases. All vessels contain a common argon line and vent line to a one way trap.

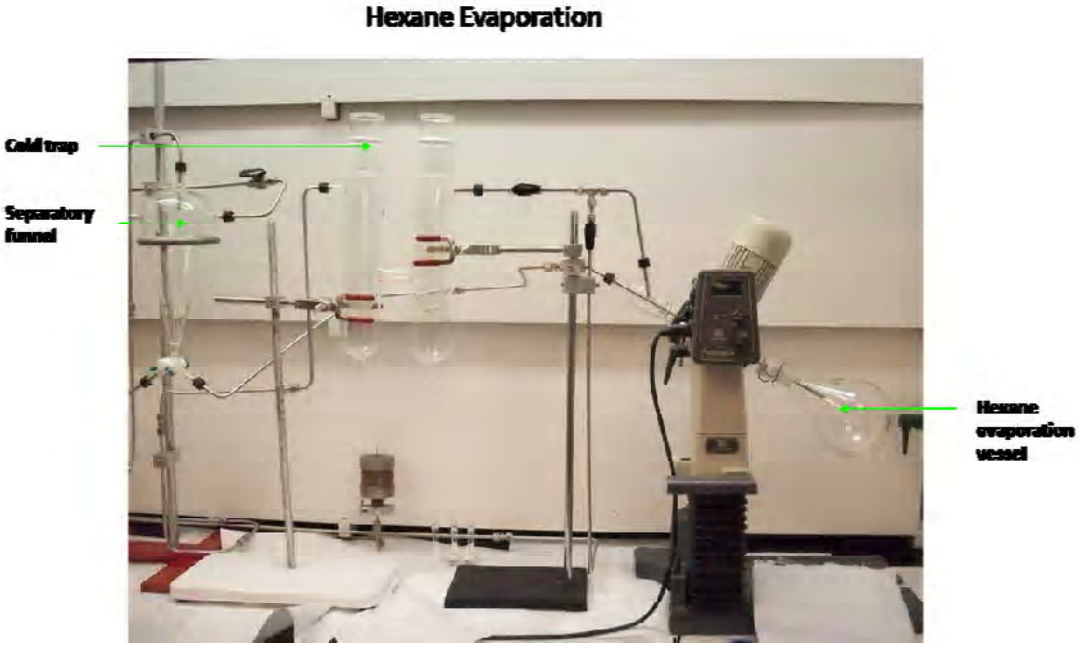

Figure 43 Hexane Evaporation System— this system consists of a rotavapor allowing for vacuum evaporation of Hexane from the InLAB+Hexane solution created in the Liquid-Liquid Extraction System, Figure 42.

The entire closed system small scale InLAB factory has undergone initial tests, and a few small modifications have been made to improve performance. Unfortunately, a poor quality batch of HMVA was received for the initial system development, and much time was spent trying to distil the HMVA to meet our QC measures. We have recently changed suppliers, and will resume tests as soon as new HMVA supplies are available.

3.8 Results of InPC Synthesis and initial InLAB Synthesis

In conclusion, initial results for both InLAB and InPC are very promising, and we are confident the degradation of attenuation length in InLAB will be eliminated soon with closed system synthesis and water washing techniques. Exact data pertaining to all InLS extractions at VT can be viewed in Appendix B: Indium Liquid Scintillator Recipes.

Metal loaded OLS status	**PC**	**InLAB**
1. Indium concentration	**8%**	**8%**
2. Scintillation signal efficiency	**~7000 hν/MeV**	**~4600 hν/MeV**
3. Transparency at 430 nm: L(1/e) (working value):	**10m**	**8m**
4. Light yield (Y%pc) (working value):	**55%**	**36%**
5. Chemical and Optical Stability:	**Stable for greater than 1 yr**	**Optics degrade after a month ~2m**
6. InLS Chemistry	**Robust**	**Robust**

Table 6 Results of preliminary InLS work for both LAB and PC.

Chapter 4: Scintillation Lattice (SL)

The Indium neutrino tag requires detection of time and space coincidences of nuclear events in self induced background. Let M be the detector target mass, and m be the target mass per unit volume of the detector. This gives a signal, S∝M, and random coincidence of In β-decay, N∝m^2g where g=M/m—the detector granularity. This gives a S:N∝1/m. Thus the LENS design must fundamentally incorporate detector granularity. The "classical" LENS segmentation design is a close packed array of longitudinal modules each with a pair of PMTs at either end, Figure 44. The module address along with location of the event by time-of-flight (TOF) along module's primary axis provides 3-D event localization.

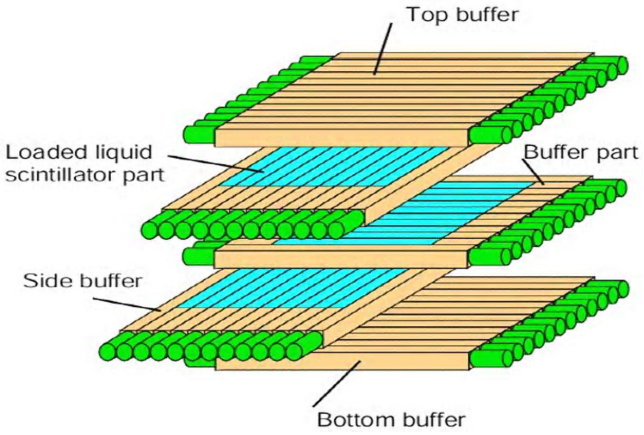

Figure 44 "Classical" LENS design. Orthogonal modules along with time-of-flight allow for position reconstruction of nuclear events in the original LENS design.

Figure 45: Acrylic cube scintillation lattice. This physical model was made by stacking 342 acrylic cubes, and one piece of scintillator somewhere inside the array, creating a 7x7x7 cube model. The hidden scintillator is illuminated by a UV-LED. The scintillator shifts the wavelength to the shifted light output (violet) of the plastic scintillator, simulating a neutrino signal event.

A more advanced design for 3-D event localization has been developed at Virginia Tech. The basic Idea extends the basic idea of the 1-D light piping properties of the "classical" design to a 3-D scintillation lattice (SL) chamber, Figure 46. The lattice design offers significant operational advantages over the 1-D module design:

- High definition of the hit cell in the lattice design—physical volume of the cell with digital detector read out not analog.
- Location accuracy is independent of the energy of the hit (detected photoelectron (pe) statistics). This is particularly important for low energy events <100 keV.

- The device operates as a "chamber", displaying tracks of particles such as muons (for tagging cosmogenic activity) and 3-D structures of γ-showers— both important for identifying event types, topologies and origins.
- Higher light collection due to light channeling along three axes opposed to one.

This chapter will discuss the optics associated with building a SL and the design of SL's starting with a solid detection media and moving to the development of a liquid detection media SL. Simulation results for the LENS SL detector design are presented in Chapter 5: Background Events.

4.1 Introduction and optical properties of the SL

The SL is a novel detector design that uses optical segmentation (instead of typical time of flight methods) for precision location of nuclear events in a large volume detector. The method allows for precision localization of short ranged events such as β-decays, and enhanced topological analysis for longer ranged events such as moderate energy gamma showers. This is a key technology for the modern LENS design. The concept is based on optical channeling of scintillation light down the primary coordinate axes using index of refraction barriers. The idea is to construct a lattice that channels isotropic light along the three primary axes of the detector. The lattice is constructed of a low index of refraction material in a high index of refraction media. The white lines in the detector,

Material	Index Of Refraction
Teflon FEP	1.34
Water	1.33
Perfluorohexane	1.27
Air	1.00

Table 7 Some low index materials that have been considered for the LENS SL.

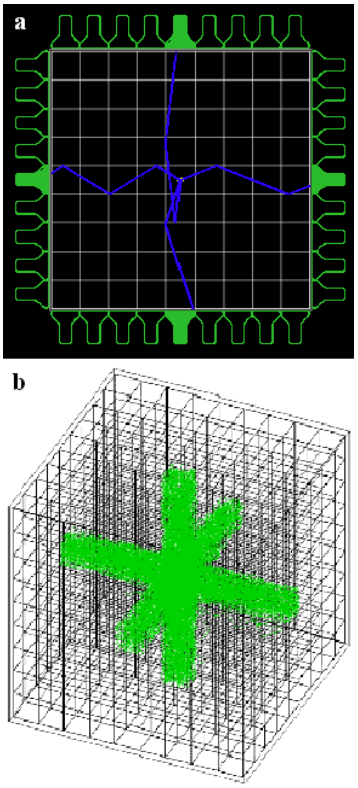

Figure 46 Light channeling in Scintillation Lattice. a: A cartoon drawing of light path in a 2-D SL. The white lines are lower index of refraction material than the bulk area. **b:** GEANT4 simulation of light channeling in scintillation lattice constructed of thin low index of refraction film in a higher index of refraction media.

Figure 46a, are low index of refraction material such as those in Table 7, and the bulk volume of the detector is organic liquid scintillator such as pseudo-cumene (n=1.504) or Linear Alkyl Benzene (n=1.482) doped with Indium. The angle which light is reflected off of the low index material is dominated by:

$$\Theta_{crit} = \sin^{-1}\left(\frac{n_{mat}}{n_{solvent}}\right)$$

Equation 7 Snell's Law for critical angle

Where n_{mat} is the index of the low index material and $n_{solvent}$ is the index of the organic scintillator. Figure 46a shows this in two dimensions. Figure 46b shows a GEANT4 simulation of this concept in 3-D. It is easy to see that the spatial resolution of the detector is equal to the size of the individual cells.

For $n_{solvent}$=1.52 and $\Theta_{crit} = 45^{O}$, n_{mat} would need to be approximately 1.07—this would provide an index barrier that would allow for no light leakage from the SL channels. For $n_{solvent}$=1.52 and $\Theta_{crit} = 54.7^{O}$, n_{mat} would need to be approximately 1.24—

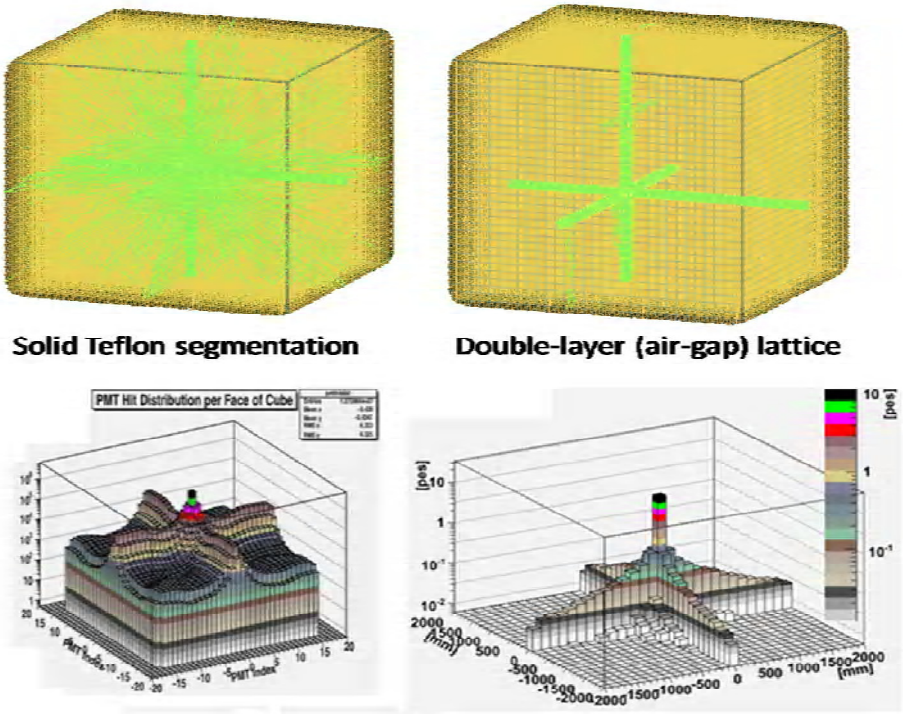

Figure 47 GEANT4 LENS simulations. These graphs were produced with GEANT4. The top shows the light traces for a high index of refraction lattice on the left, and a low index of refraction lattice on the right. The bottom shows te distribution of light on one of the 6 detector surfaces. Simmulation results by Jeff Blackmon presented at LUNO-LENS meeting.

this would provide an index barrier that would allow for no light trapping in the event vertex cell. There exist no good materials for the SL at either of these indexes; therefore, we must look into materials with slightly higher and lower indexes of refraction. In our selection of materials we consider a few index dependent aspects of the SL—light trapping, light leaks, Fresnel Reflections, and photon time to PMT as well as material compatibility aspects for the plastic films with organic liquid scintillators.

4.1.1 Light Trapping, Light Leaks, Photon Time to PMT and Fresnel Reflections

For a Θ_{crit} less than 54.7^{O} a portion of light will be trapped in the central cell. If Θ_{crit} is greater than 45^{O} a portion of light will be unchanelled. There is little advantage to a scheme with a critical angle less than 54.7^{O} over that of a critical angle less than 45^{O}. The scheme with a critical angle greater than 45^{O} allows for greater light collection, Figure 47 and therefore greater energy resolution, as well as, sharper photon arrival at the PMTs, Figure 50.

$$R_s = \left[\frac{n_1\cos\theta_i - n_2\sqrt{1-\left(\frac{n_1}{n_2}\sin\theta_i\right)^2}}{n_1\cos\theta_i + n_2\sqrt{1-\left(\frac{n_1}{n_2}\sin\theta_i\right)^2}}\right]^2$$

Equation 8 Fresnel reflection coefficient for s-polarized light.

$$R_p = \left[\frac{n_1\sqrt{1-\left(\frac{n_1}{n_2}\sin\theta_i\right)^2} - n_2\cos\theta_i}{n_1\sqrt{1-\left(\frac{n_1}{n_2}\sin\theta_i\right)^2} + n_2\cos\theta_i}\right]^2$$

Equation 9 Fresnel reflection coefficient for p-polarized light.

$$R = \left[\frac{n_1 - n_2}{n_1 + n_2}\right]^2$$

Equation 10 Fresnel reflection for perpendicularly incident light.

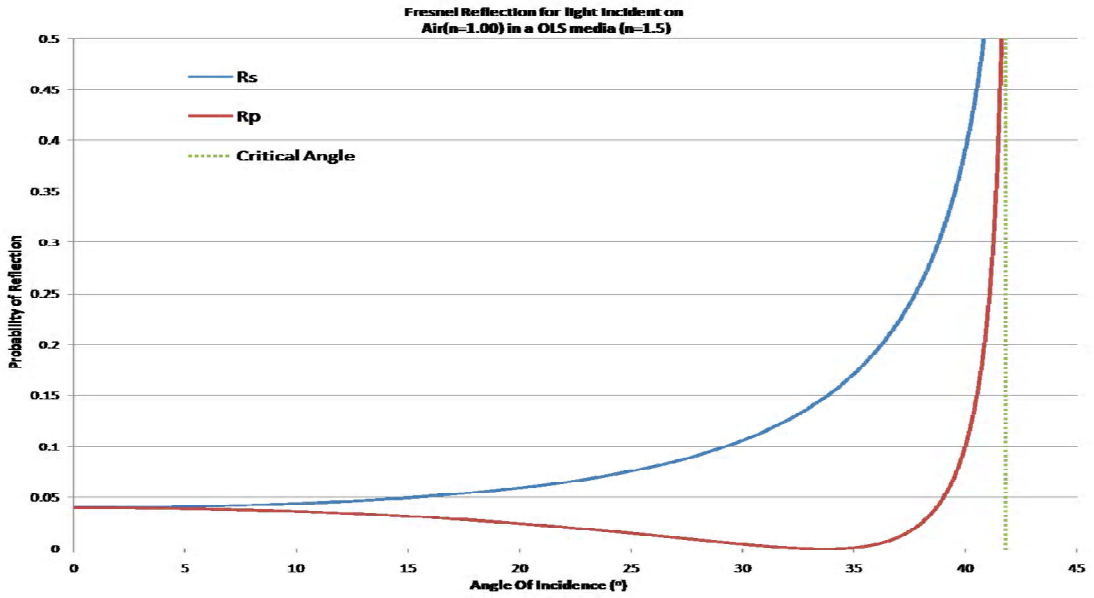

Figure 48 Fresnel affect for p and s polarized light in an OLS media incident on an air interface.

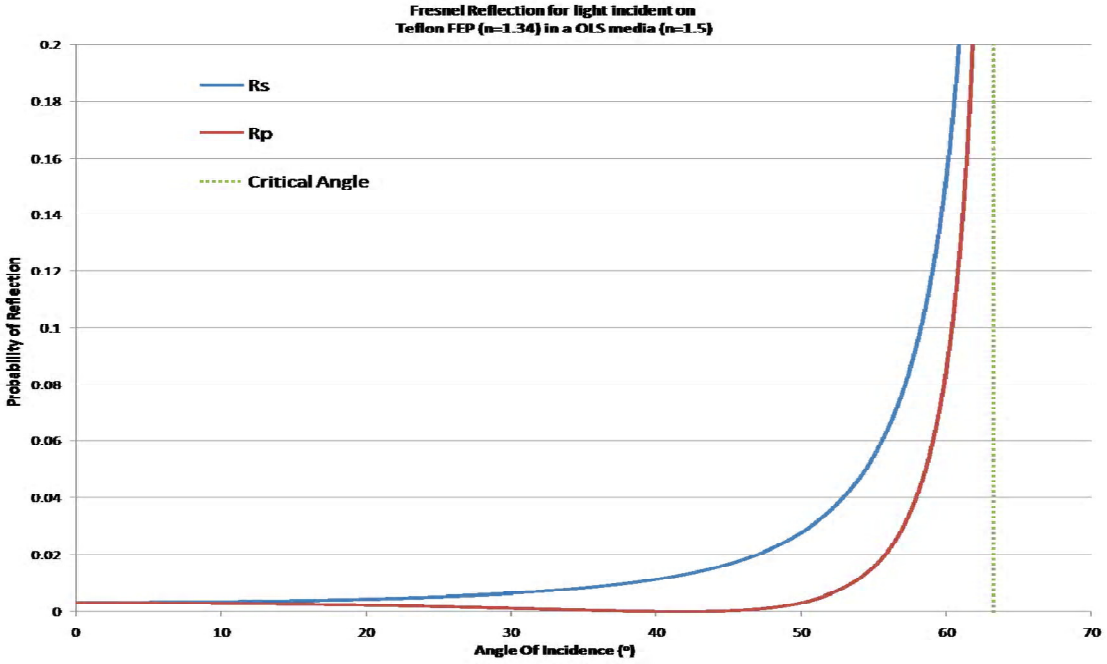

Figure 49 Fresnel affect for p and s polarized light in an OLS media incident on a Teflon FEP interface.

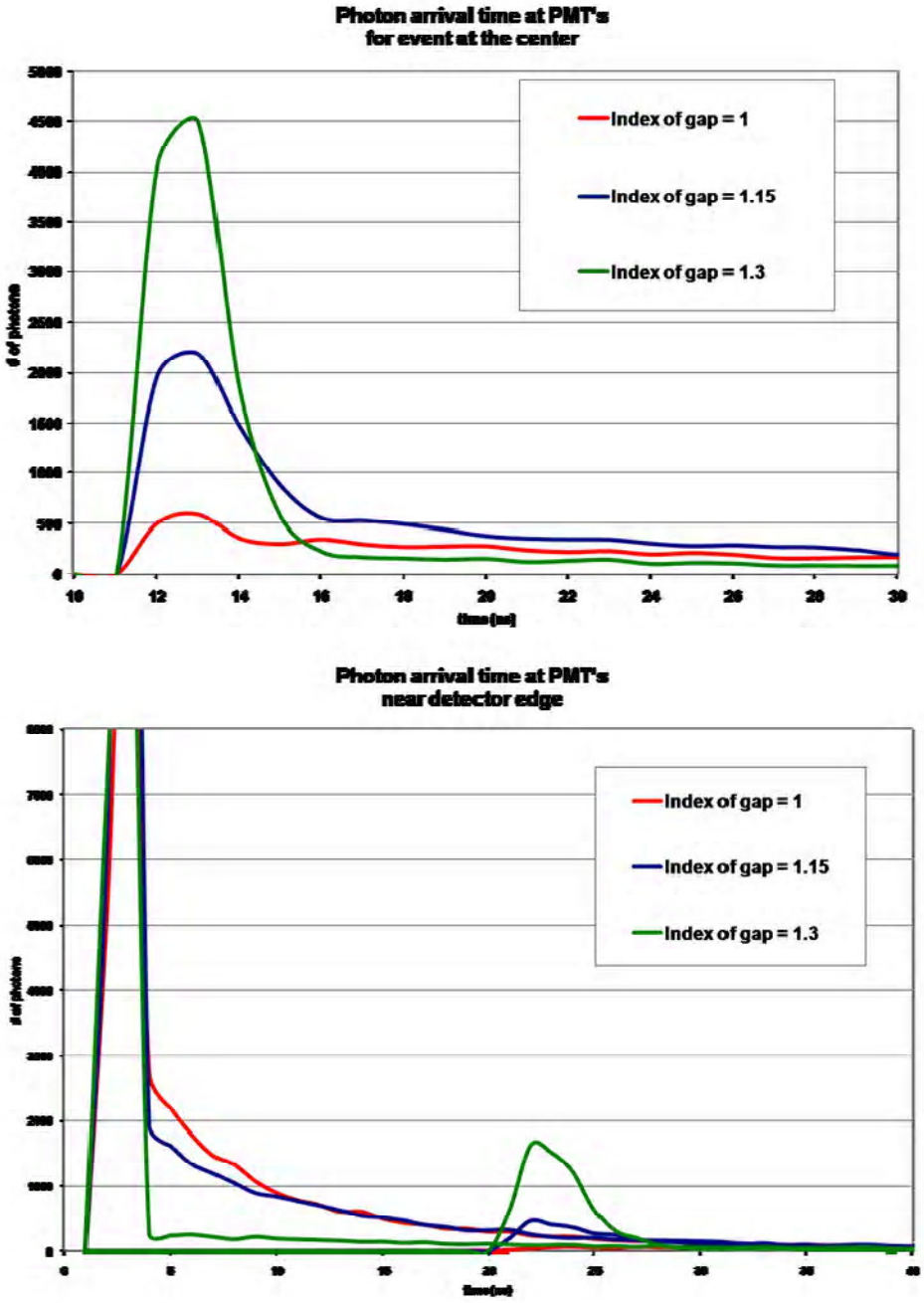

Figure 50 Photon to PMT time in LENS. The upper graph here shows the expected timing distribution for photons that are produced in the central cell of the LENS detector, index barriers, 1, 1.15, and 1.3. The lower graph shows the same event occuring near the edge of the detector. Higher index materials give a sharper time resolution.

Equation 8 to Equation 10 are the Fresnel equations which with attenuation length through materials govern the optics of the SL, and Figure 48Figure 49 are graphs of the Fresnel reflection coefficients for p and s polarized light vs. angle of incidence for OLS to air and OLS to Teflon interfaces respectively.

Figure 50 shows the effects of the Fresnel reflections in the vertex channels of the SL for various indexes of refraction; n=1, n=1.15, and n=1.3. The top graph shows the photon arrival time distribution at the PMTs for the vertex cell. It is easily seen here that the higher index has a much sharper peak. The bottom graph shows the photon arrival time distribution for an event located near the edge of the detector. The first peak is the near PMT, and the second peak is the PMT on the far side of the detector. All indexes have good rise time on the near PMT, but the decay time for the near PMT is much better for the high index material, while the far PMT receives very few photons for the low index material, and a significant peak for the higher index material. The conclusion is, higher index materials allow for adequate position resolution and better light collection on the detector faces, while lower index materials exhibit poorer timing and larger effective attenuation lengths due to Fresnel reflections.

4.2 Realization

As shown above the theory of the scintillation lattice is simple, but how does one go about constructing such a device? If the detection medium were a solid with index of refraction ~1.5 (glass, quartz, acrylic, etc) it is quite easy—one can simply cut cubes of equal size and stack them together, Figure 45. The air trapped between the blocks will act as the index of refraction barrier. If one needed a higher index of refraction barrier, then the medium in which the cubes are stacked could be liquid (water, mineral oil, etc.) with the required index.

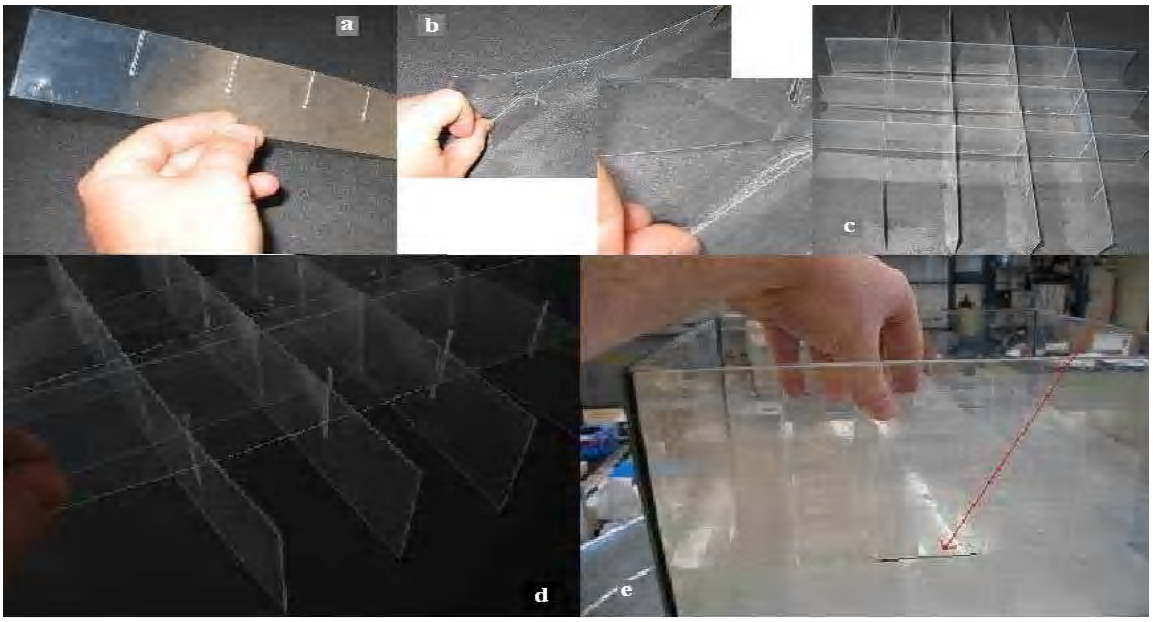

Figure 51 The primary building block of the SL. **a:** A strip of support structure material and Teflon FEP, with notches cut in it. **b:** The layering of the support structure material and the low index film. **c:** Here the strips have been interlocked. **d:** The last strip of one layer is being put in place **e:** The red arrow points to, the large sheet placed between the comb structures (the black line highlights a segment of this layer).

For a SL, with the bulk volume being liquid, the task is more difficult. Rather than introducing the bulk volume into a low index volume and having the low index flow around the cubes to form thin layers, we must now introduce the thin layers, and structure to support them into a liquid medium. While we have methods for both solid and fluid (sealing the fluid between two layers of support structure) index barriers, we focused on the solid barriers i.e. Teflon FEP, due to ease of construction.

The mechanical structure is provided by a secondary thin clear film/sheet that is much more rigid than Teflon FEP, and has index comparable to that of the liquid. PET and Acrylic meet these specifications. The Teflon FEP and support structure material are cut with notches in them Figure 51a; such that, when an identical piece is lined up at 90^{O} the notches slide into one another Figure 51c&d. Large sheets, composed of FEP and support structure material, are placed on top of these grids, and the grids are stacked to the desired height Figure 51e.

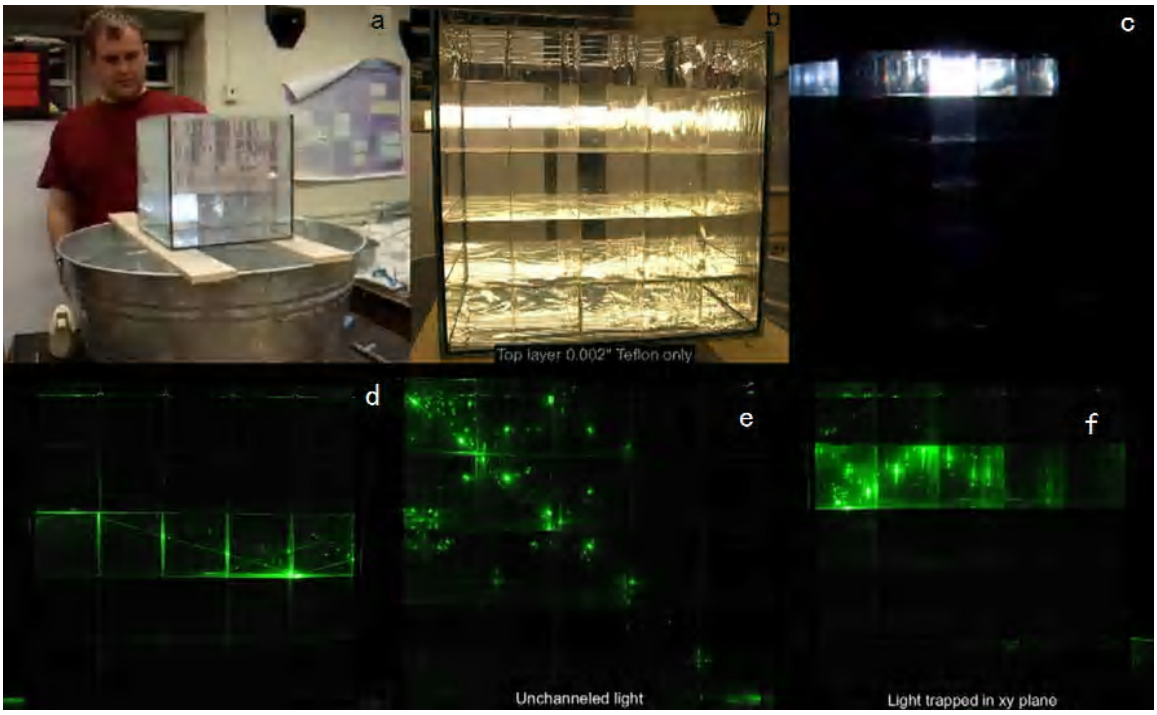

Figure 53 The first test of a SL in liquid, picoLENS. The lattice size is 2 inches and is made with Teflon FEP and PET for support. The liquid is ethylene glycol a: Christian Grieb shines a flashlight down one channel of PicoLENS. b: a close up view of one side under normal room lights. c: a flashlight being shown down on channel of PicoLENS in a dark room. d: a green tapped in a single channel. e: A green laser demonstrating unchaneled light. f: A green laser being channeled within the x-y plane.

Figure 53 shows the first SL we constructed in a liquid media, picoLENS, and various paths of a laser being shown through the SL. PicoLENS (10"x10"x10") is segmented into 125 (2"x2"x2") cells. Figure 52 is a demonstration of the microLENS detector, a 19.5"x19.5"x19.5" detector with 216 (3.25"x3.25"x3.25") cells. The microLENS detector will be instrumented with PMTs on three sides and VM2000 reflective film

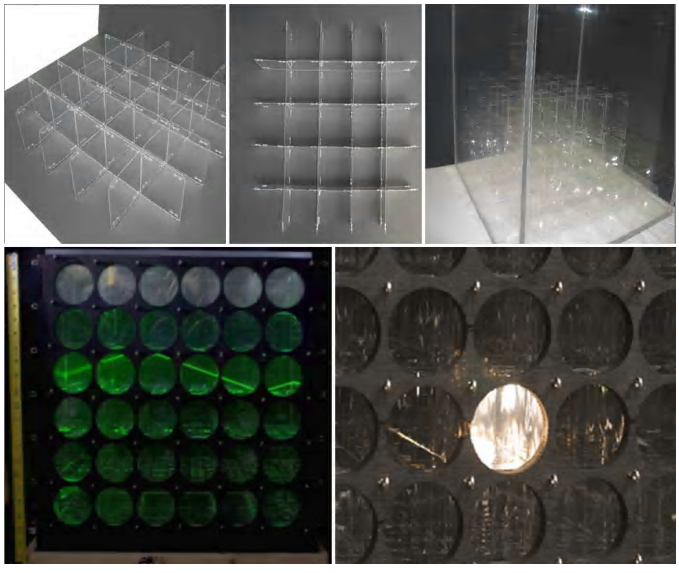

Figure 52 microLENS is a test model that was constructed to test the construction methods for the miniLENS detector (top: microLENS during construction). The lattice is $(8.25\text{cm})^3$, and is made with Teflon FEP tacked to thin acrylic using a stapling method. Note the excellent light channeling.

on the opposite three sides. With this instrumentation setup microLENS will study the optics and spectroscopy of the SL with artificial sources.

4.3 Film Materials

The selection of material is mainly based on chemical compatibility, absorption within the bulk material, the index of refraction, and radio purity, Table 8 to Table 10 list these properties. Secondary is the ease of construction; solid material is much easier to work with. We refer to the solid material method as single foil and the fluid material method as double foil due to the fluid needing to be sealed between two layers of film.

For the single foil SL the best materials were likely those discussed in the previous section; however, THVP 2030 GX, Teflon PFA and Teflon AF are other options we have considered.

THVP 2030 GX, Teflon PFA and AF may be alternatives in the future. THVP 2030 GX is a fairly new product we are looking at, it has much better attenuation length than Teflon FEP and comparable index of refraction; however, we have observed some self adhesion in the lab which we are investigating. The short comings of Teflon PFA are the higher index of refraction and lower attenuation length, Table 8. Teflon AF may become a viable candidate for the SL in the future, but at this time, it is more expensive than Teflon FEP as well as much more difficult to procure.

The construction of a double foil SL with a fluid index (i.e. water) barrier is similar to that of the single foil SL. The main difference being that the index barrier must be trapped between two layers of support material. This can be accomplished by wetting the surface and sealing the edges via heat or adhesive. The final pieces with fluid sealed within them are shaped like the sections in Figure 51, and fit together in the same manner. Fluids considered for this method are air, water, and perflourohexane. The support materials considered for encapsulating these fluids are Acrylic, PET, and Nylon.

Material	Method/reference	Teflon FEP	Teflon PFA	Teflon AF
Supplier		CS Hyde	CS Hyde	Dupont
L(1/e) (cm) @430nm	Calculated from Transmission Data of 1mil and 2mil material measured At Virginia Tech with an Evolution 600 UV/Vis	0.27	0.12	N/A
Transmission (%) @ 430nm of 2mil material	Measured at Virginia Tech with an Evolution 600 UV/Vis	92.5	89.5	N/A
Refractive Index	ASTM D-542 Dupont.com	1.341-1.347	1.35	1.29-1.31
Solar Transmission	ASTM E-424 Dupont.com	96%	96%	>95%
Specific Gravity	ASTM D-1505	2.15	2.15	N/A
Availability		CS Hyde	CS Hyde	Special contracts and confidentiality agreements with Dupont*
Is the material compatible with InPC	Material placed in solvent and monitored for degradation over a 6 month period	Yes	Yes	N/A
Is the material compatible with InLAB	Material placed in solvent and monitored for degradation over a 6 month period	Yes	Yes	N/A

Table 8 Optical properties for clear fluoropolymers, that may be suitable for the LENS single foil SL

*restrictions for obtaining Teflon AF have eased since this work was done, but Teflon AF film is not yet commercially available.

Material	Method/reference	Air	Water	Perfluoro-hexane
Supplier				Fisher Scientific
Index of Refraction	http://en.wikipedia.org/wiki/List_of_refractive_indices	1.0003	1.33	1.25
L(1/e) (cm) @430nm	Measued via absorption in a 10cm cell in an Evolution 600 UV/Vis	>10m	>10m	N/A
Availability		procurement not necessary	DI water source	Fisher Scientific

Table 9Optical properties of fluids that may be suitable for the LENS double foil SL

Material	^{232}Th (mBq/kg)	^{238}U (mBq/kg)	^{40}K (mBq/kg)
Acrylic (plexiglass)	0.016	1.20E-01	0.02
Teflon (PTFE)	<20	<15	80
Glass fiber	<20		600
Mylar (alluminized)	0.16	6.80E-01	0.68
Water (distilled)	3.70E-05	9.88E-05	2.60E-04

Table 11 Radiopurity data for potential SL construction materials. The data was obtained from http://radiopurity.in2p3.fr/

Material	Method/reference	Nylon 6,6	Polyester/ Mylar	Acrylic
Supplier		Dupont	Dupont	Optical Polymers
L(1/e) (cm) @430nm	Calculated from Transmision Data of variable thickness material measured At Virginia Tech with an Evolution 600 UV/Vis	N/A	0.12	N/A
Transmision (%) @ 430nm of 2mil material	Measued at Virginia Tech with an Evolution 600 UV/Vis	92.5	82.5	92.25
Availability		CS Hyde	CS Hyde	Optical Polymers
Is the material Compatible with InLAB	Material was placed in InLAB with a ¼ radius bend. And Monitored over 6 months.	No	N/A	Yes
Is the material compatible with InPC	Material was placed in InPC with a ¼ radius bend. And Monitored over 6 months.	No	N/A	Not under stress

Table 10 Optical properties of support material that may be suitable for the LENS single foil SL

4.4 Future Considerations

It is worth noting there are a few other ideas that have considered in the development of the LENS SL:

1) Antireflective films for the lower index (n~1.00) SL option.
    a. Thick "antireflective" films (n~1.22 typically made very thin, ~120nm, but may be able to made thicker) in place of the low index material.
2) Single film SL with wire supports
3) Multilayer films
4) Teflon laminated acrylic or other substrate

4.4.1 Antireflective films

If air is chosen as the low index of refraction material for the SL it is likely we will need to reduce the effects of Fresnel reflections by adding antireflective coatings to

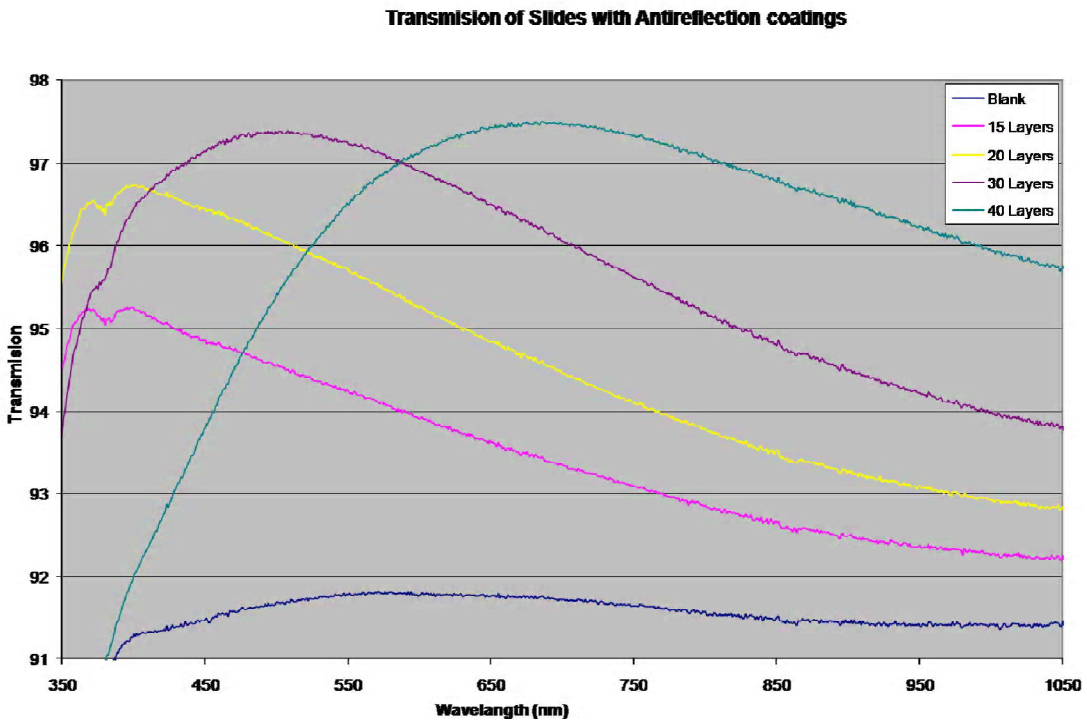

Figure 54 Transmission of glass slides with antireflective coatings.

the surface of the films containing the air. Antireflective coating work by adding a material to the surface ¼ the wavelength of interest thick and that has an index of refraction of $n_1 = \sqrt{n_0 n_s}$, where n_1 is the index of the material added to a substrate with index of refraction n_s and n_0 is air. For an incident wave of the wavelength of interest the reflected portion of the wave at the n_0 to n_1 interface and the reflected wave at the n_1 to n_s interface are 180 degrees out of phase with equal amplitudes providing destructive interference and allowing for 100% transmission. For an air to glass interface (close to air to plastic) n_1 needs to be ~1.22. A film with n~1.22 has not yet been developed; however, porous silica nanoparticle films have been developed using ionically self assembled monolayer (ISAM) methods. These films have porous structures providing for very low effective indexes of refraction (n~1.26-1.3). [65]

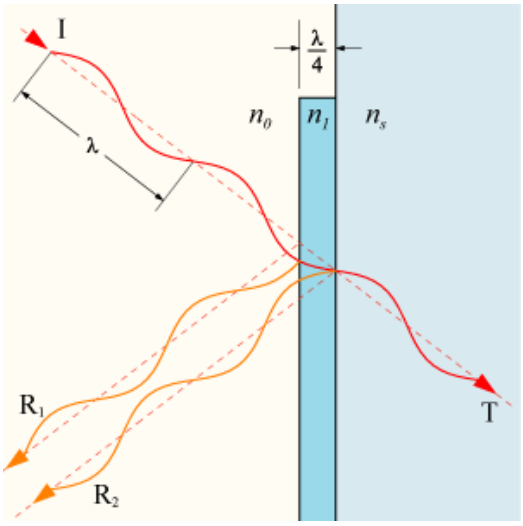

Figure 55 Quarter wavelength thick antireflective coating. Image taken from http://en.wikipedia.org/wiki/Anti-reflective_coating. The reflected waves from the n0 and n1 interface and the n1 and n2 interface are equal in amplitude and 180 degrees out of phase; therefore, completely canceling and giving a 100% transmission.

The basic method is ISAM. The substrate (a glass slide for this work) is dipped in a polymer solution ionically binding the polymer to the substrate then dipped in a silica nanopartical solution allowing the nanoparticles to ionically bind to the polymer. This completes a single layer. The procedure can be repeated until the desired thickness is reached. Transmission data for a blank slide and slides with 10, 20, 30, and 40 layers are shown in Figure 54. As expected due to Fresnel reflection the transmission of a blank glass slide is ~92% for all wavelengths. This survey of samples shows ~30 layers would be appropriate to maximize the transmission of the wavelength of interest in LENS (~430nm).

It is worth noting the index of these films is also good for creating the SL index barrier. If one can produce thicker films with long attenuation lengths this may be a direction of interest for the LENS SL in the future.

4.4.2 Single Film SL with Wire supports

A SL design which has been considered in the past was recently tested for ease of construction and film alignment for the miniLENS detector. This design uses only 0.002 inch FEP Teflon film with 400 micron quartz fibers. The design ensures 'perfect' alignment and minimal mass of support materials. While the approach would also work for LENS proper, the weight of the Teflon film 60 cubes high is about 150 grams per cell corner. The quartz fibers (two per corner) are plenty strong, but the bottom plane vertical film may itself buckle under the weight. This can be easily tested, and is not a problem for a miniLENS scale detector.

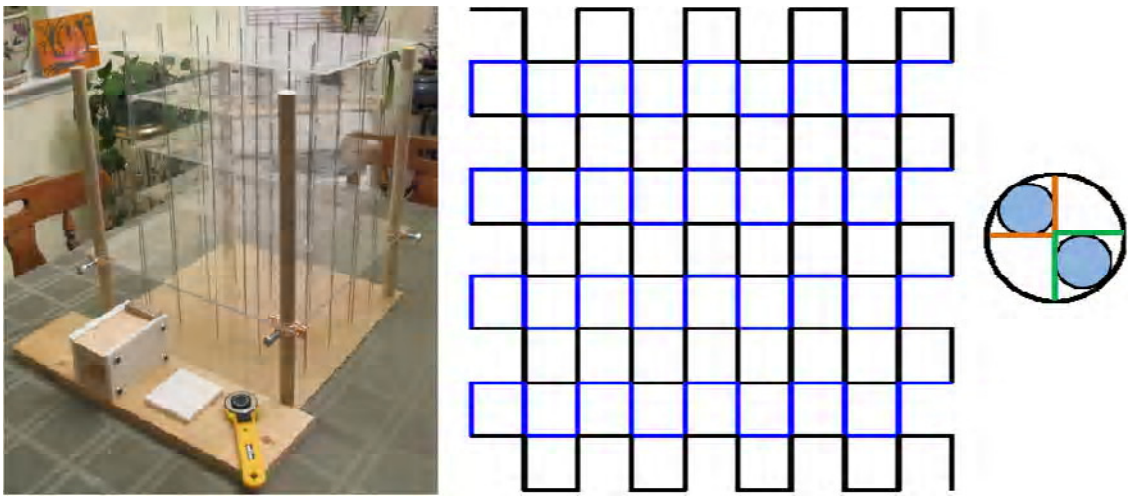

Figure 56 Single Film SL with wire supports. Left: a model of a single film SL supported by vertical wires. Middle: the weaving pattern for the film through the wires. Right: a cross sectional view of a corner held by two wires. This method of building a SL reduces the support material mass and internal radioactivity of the detector.

A model of such a structure is shown in Figure 56 left. In the model the vertical 'beams' are stainless steel welding rods. These would be 400 micron bare quartz fibers in the real system. For corners where two films meet there are two vertical fibers through a single hole in the horizontal plane, Figure 58. One of the vertical film strips goes around one of the fibers, and the other film strip around the other fiber. Note the acrylic plate being supported by the structure in Figure 56 left, which is twice the mass of the film for miniLENS. The vertical planes are formed by a 3.25 inch Teflon FEP strips, pre-creased every 3.25 inches. These strips can be made by winding the film onto a spool, mounting it on a lathe, and then using a round, rolling, razor blade to part off 3.25 inch

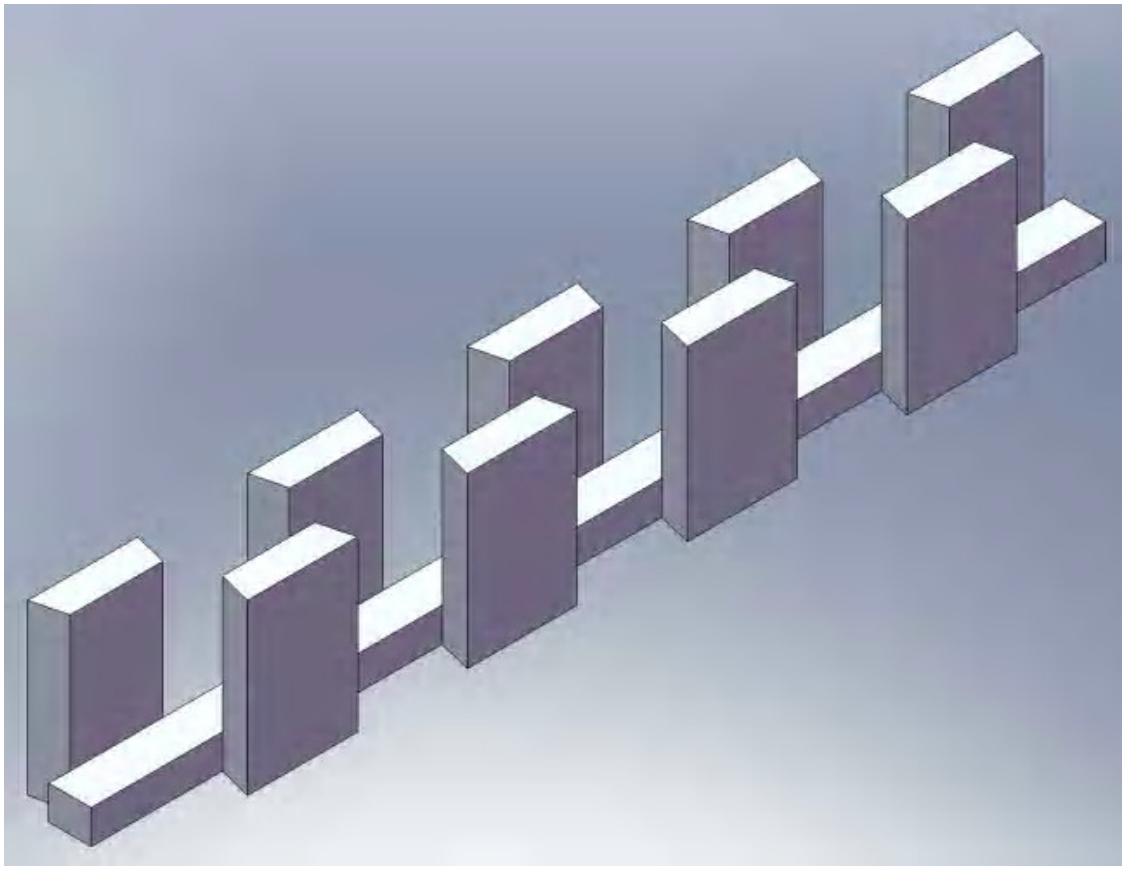

Figure 57 Teflon strip creasing apparatus. The film is weaved through the fixture, pulled taught, the bottom edge resting on the strong-back, and then the creases 'set' by using a rubber roller along the 'knife' edges.

strips. A simple fixture can be used to set the creases with excellent precision Figure 57. The film is weaved through the fixture, pulled taught, the bottom edge resting on the strong-back, and then the creases 'set' by using a rubber roller along the 'knife' edges (the creases were set for the demonstrator by hand using the apparatus below the demonstrator in Figure 56 left).

In principle, an entire plane of miniLENS can be made from a single strip, only attached at two ends. Should this prove unwieldy, strips between two opposite sides can be mounted individually (black lines and blue lines of Figure 56 middle). The strip ends are bent back over the quartz fiber and stapled to themselves to hold them against pulling free. At the end of the strip runs, there is also a second fiber, to ensure the folded back film lies back flat against itself. The horizontal planes have small holes on a 3.25 inch square grid pattern, along with small pin-holes in the center of each grid to avoid air trapping during detector filling. The sides are extended by 3.25 inches and then folded

down (along dotted lines in diagram below) to provide the side Teflon film (except for the very bottom plane). This results in a double layer of Teflon every other channel, but should have minimal impact. It also stiffens the edges of the horizontal sheet, and enables the fibers to have fully confining holes against the detectors edge. Since commercially available FEP film is only 24 inches wide, multiple horizontal sheets will be overlapped slightly, with the same quartz fibers going through holes in both providing good alignment.

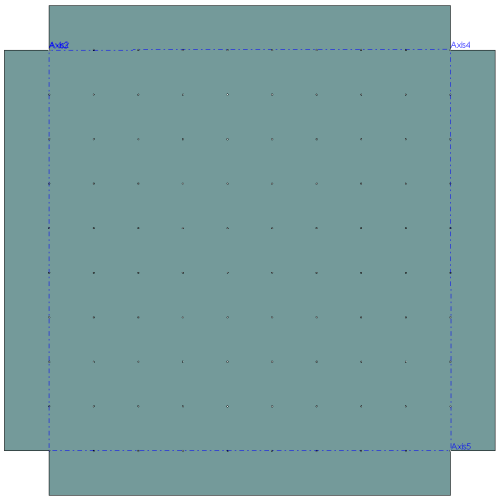

Figure 58 Horizontal Teflon FEP sheet for the miniLENS wire frame scheme. Holes are placed on a 3.25" x 3.25" gird to allow quartz fibers to pass through the plane.

Assembly is done from the top. Shallow holes are drilled in the bottom of the detector, defining vertical channels to hold the quartz fibers. The bottom Teflon sheet is started from the top and then slid down the fibers about 5 inches. The first vertical strip(s) is then weaved through the fibers. The second Teflon sheet is then added, and the combination slid down the fibers. This repeats until all the layers are in place. The fibers extending out the top of the detector are then clipped to length, and the top detector face put in place. The fibers are thus only marginally confined at their top and bottom, but are held vertical by the eight intervening horizontal planes.

One major advantage of this design is that it allows complete compatibility with a PC based scintillator.

Chapter 5: Background Events

The primary backgrounds in the LENS detector will arise from the β-decay of ^{115}In; however, there are other background events we will look at as well, mainly gammas from Uranium, Thorium and Potassium (UTK backgrounds) and their daughters.

The backgrounds are broken into two major categories: 1) internal – those nuclides located within the detector vessel (UTK contamination of scintillator and lattice structure) and 2) external – those backgrounds outside of the vessel (UTK from PMTs, shielding, and rock as well as ^{60}Co from construction and shielding steel) and the vessel itself.

5.1 Internal Background Backgrounds

Internal backgrounds in LENS primarily arise due to β-decay of ^{115}In in coincidence with some decay or group of decays that satisfy the solar-ν signal tag. The following sections discusses the mimicking of solar-ν events by ^{115}In in great detail, and plans for studying non-^{115}In internal backgrounds due to primordial radio nuclides and their daughters and cosmogenic radio nuclides. [66] It is important to note—these simulations were run prior to the development of the SL and have optimistic assumptions regarding attenuation length of SL films, light yield (including no quenching), detector size. The LENS collaboration is currently working on updated simulations using measured parameters for multiple detector designs.

5.1.1 Indium Induced Backgrounds

The primary background in LENS arises from random coincidences of 115—Indium β-decay spectrum that overlaps the pp-ν signal. The focus of the background analysis has been modeling of the ^{115}In background with sufficient statistics and the development of background suppression techniques to maximize the ν detection efficiency and the signal to noise ratio. In the following discussion, e_1 represents the prompt electron from a solar ν event, γ_2 represents the gamma emitted from the de-excitation of ^{115}Sn $7/2^+$ to $5/2^+$ state, and γ_3 represents the gamma (approximately half the

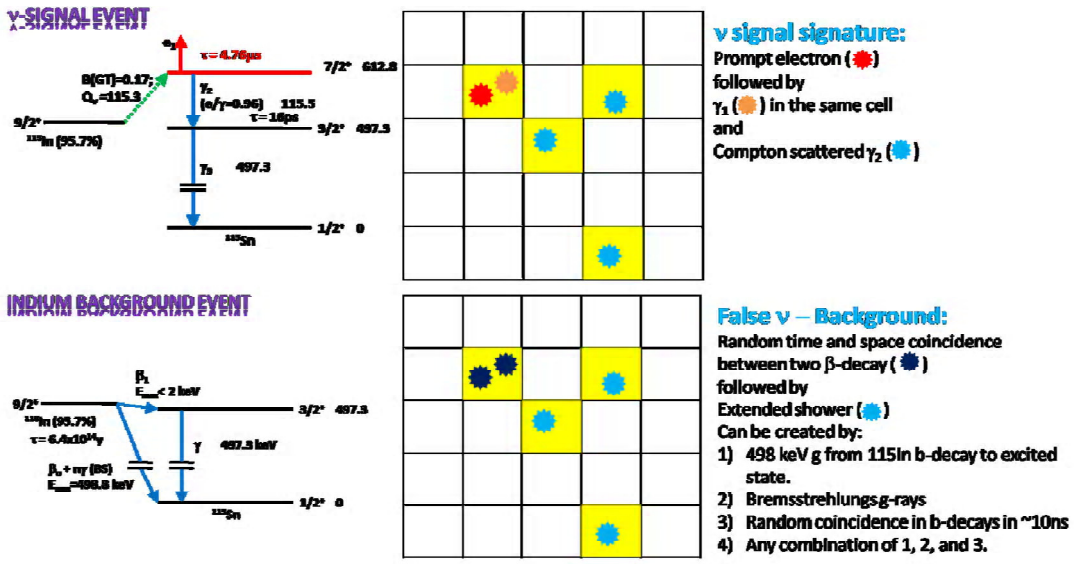

Figure 59 Shown above is the radiation schemes and event topology for ^{115}In decay and neutrino tag. The neutrino tag (top) consists of a 115.3 keV gamma ray (γ_2) or conversion electron (each with a 50% branching ratio), and a 497.3 keV gamma ray (γ_3). The total energy of the gamma tag is $\gamma_2 + \gamma_3$ = 612.6 keV. The neutrino event sequence starts with the, solar ν-signal electron, e_1 ($E_e = E_\nu - 115.3$ keV), in the vertex cell. After a mean lifetime of 4.76μs (10μs time window) the $\gamma_2 + \gamma_3$ tag appears with γ_2 in the vertex cell (space coincidence). The penetrating 497.3 keV gamma, γ_3, escapes from the vertex cell and creates a shower in the vicinity of the vertex. N_{hit} is the number of cells in the gamma shower, and is used as a cut in data analysis. Such an event pattern is used as a template for filtering out random non-solar tag candidates. The tag can be mimicked, most likely ^{115}In β-decays. One (or more) ^{115}In β-decays can mimic the entire neutrino tag. Any coincidence of a ^{115}In β-decay in the prior 10μs to the mimicked tag, will result in a false ν-event (bottom). Figures reproduced from Ref. **(66)**.

time a conversion electron is emitted instead) emitted from the de-excitation of ^{115}Sn $3/2^+$ to $½^+$ state, Figure 59.

The main trigger scheme is designed to detect the basic topology of a candidate shower event—two events in the same cell (the "vertex") within 10μs, the second event occurring with a shower of N cells hit, N_{hit}, within 10ns of the second vertex event. The main trigger selects only time/space with $N_{hit} \geq 2$ coincident events—at least two cells are hit in the delayed tag. This occurs at a rate of ~40Hz for 7.5cm cells in the full scale LENS detector (~10t ^{115}In). The ^{115}In β-decay can occur in three different modes:

1) Pure β
2) β + γ (from bremsstrahlung radiation)
3) Pure γ from weak (1.2×10^{-6}) low energy β-decay (<2keV) of ^{115}In to the 498keV $3/2^+$ state of ^{115}Sn (refe).

The mimicked tag can occur with multiple ^{115}In decays, each of which can emit radiation of one of the above modes. In order to be mistaken for a ν tag multiple events must occur in prompt succession, $\tau \leq 10$ns. Several analysis cuts are applied to a candidate shower.

i) $N_{hit} \geq 3$

We impose a restriction on the number of cells hit by $\gamma_2 + \gamma_3$, γ_2 must hit in the vertex cell (the cell which e_1 hit) and γ_3 must hit at least two cells outside the vertex cell, Figure 59. In the background shower the vertex cell is unknown; therefore, all hits in the background shower are candidates for the vertex. The N_{hit} condition requires three individual ^{115}In β-decays in very short coincidence ($\tau \leq 10$ns), the production of a gamma ray via bremsstrahlung from a ^{115}In β-decay, or a gamma from ^{115}In β-decay to ^{115}Sn $3/2^+$ excited state (which has low probability, 1.2x10-6) to mimic the $N_{hit} \geq 3$ cut.

ii) Topological cuts

a. "Shower Radius"

γ_3 in the tag cascade is of relatively low energy and therefore is typically contained in a small volume. This allows us to constrain the tag shower of γ_3 to a "sphere" around the vertex cell. The acceptance volume is chosen large enough to contain most real event, but is small compared to the total detector volume, thus providing significant background rejection.

b. "Shower Continuity"

By limiting the maximum distance of any one hit from its nearest neighboring hit we are able to significantly reduce background events. This condition recognizes the difference in a Compton shower and a certain multiple β-decay false tag where one β-decay produces a low-energy gamma via bremsstrahlung that has enough energy to cross over into a neighboring cell, and is in coincidence with another random β-decay providing the third hit necessary for a valid tag (see i above). This second

β-decay occurs on average far away from the other two cells hit; therefore, making it distinguishable from a Compton shower.

iii) Energy cut

The total tag energy must be 612.6 keV. The ^{115}In β-decay endpoint is E_o=498keV, 115keV (ΔE) less than the tag energy. The energy resolution δE/E expected in LENS is ~4.7% at 500keV (δE ~23keV). Therefore, the separation ΔE/ δE~5 provides a very powerful background suppression due to false tag from a single ^{115}In β-decay.

For multiple ^{115}In β-decays the combined energies will naturally span the 612.6 keV energy window; however, these events are strongly suppressed due to the fact they must occur in very fast coincidence ($\tau \leq 10$ns) to mimic the timing structure of a Compton shower.

Background Description		Relative Importance
One ^{115}In decay in the delayed tag	A_1 = β + Bremsstrahlung γ (E_{point} = 499keV)	x1
	A_2 = Sn $3/2^+$ --> Sn $1/2^+$ (E_{tot} = 498kev)	x 1
Two ^{115}In decay in the delayed tag	B = β + β with at least one Bremsstrahlung γ	x τ
Three ^{115}In decay in the delayed tag	C = 3 β-decays	x τ^2
Four ^{115}In decay in the delayed tag	D = 4 β-decays	x τ^3

Table 13 Classification of 115In backgrounds in LENS.

Analysis Cut Descriptions	**Signal (yr^{-1} t_{In}^{-1})**	**Background total (yr^{-1} t_{In}^{-1})**	**Background type (yr^{-1} t_{In}^{-1})**		
			A_1	**A_2**	**B**
RAW	62.5	$79x10^{11}$			
Valid Space/Time. A prompt signal electron and delayed tag with a common cell hit	50	$2.76x10^5$	$8.3x10^4$	$2.8x10^3$	$1.9x10^5$
$N_{hit} \geq 3$	46	$2.96x10^4$	$2.6x10^4$	$2.5x10^3$	$1.4x10^3$
Tag Energy = 612.6 keV	44	306	0.57	4.5	293
Tag Topology	40	13±0.6	0.57	4	8.35

Table 12 Role of esperimental cuts in LENS background analysis. The analysis cuts result in an overall background suppression by a factor of ~$6x10^{11}$ at the cost of a signal loss by a factor ~1.6.

Table 13 gives a summary of possibly ^{115}In backgrounds, and their relative importance based on multiple event probability. A_1 and A_2 type backgrounds from single ^{115}In β-decays can easily fulfill the $N_{hit} \geq 3$ requirement and the topology cuts due to the fact that the events produce real Compton showers; however, these backgrounds are virtually eliminated when an energy cut is applied $\gamma_2 + \gamma_3 = 612.6$ keV compared to a maximum energy of 499keV for A_1 and A_2 , tabl. B, C, and D type backgrounds from multiple ^{115}In β-decays are suppressed by a requirement of fast coincidence ($\tau \leq 10$ns) between the ^{115}In β-decays, factors τ^n in Table 13; therefore, the primary multiple ^{115}In decay background is type B with the least stringent coincidence condition, and is relatively unaffected by energy cuts due to reason discussed in iii) Energy cut above.

Type B backgrounds are two ^{115}In β-decays in fast coincidence ($\tau \leq 10$ns) with one resulting in a Bremsstrahlung γ ray (BS-γ), producing $N_{hit} \geq 3$ within the shower volume. B backgrounds increase as the cube of the distance between the BS-γ and the lone ^{115}In β-decay; therefore, the main tool for suppressing type B backgrounds is the b. "Shower Continuity" topology cut discussed above. Even after the topology cut B persists, tabe, because type B backgrounds with $N_{hit} > 3$ have events where the lone ^{115}In β-decay discussed above are also accompanied by a BS-γ. These are largely not suppressed by this topology cut, but the residual type B background events are already small enough to yield a favorable signal to noise ratio of 3:1. Type C and D backgrounds are highly suppressed by τ^3 and τ^4, and the Mote Carlo simulations have shown them to be negligible. We will continue studying pattern matching algorithms to further reduce B-type backgrounds, but the current results yield a favorable 3:1, signal to noise ratio.

Table 12 lists the roles and effects of experimental cuts in suppressing the ^{115}In background. The initial ^{115}In β-decay singles rate is ~8 x 10^{12} events / (year x ton ^{115}In); however, the cut constraining e_1 and γ_2 to the same cell with a time separation of less than 10μs gives a "free" reduction by ~3x10^7, line 2; such that, the burden of background suppression via analysis cuts is only 3 x 10^5 events / (year x ton ^{115}In). It is thus sufficient to generate some 3 x 10^6 ntuples of all types of ^{115}In events (A-D) for reasonable precision in the analysis; all events are created using the Cern GEAN4 simulation toolkit. The $N_{hit} \geq 3$ and energy cuts, line 3 and 4 respectively, combined give

practically eliminate the type-A backgrounds, and provide and overall background reduction factor of ~10^2, hence the importance of energy resolution in LENS. The type-B backgrounds largely survive the energy cut, requiring "shower radius" and "shower continuity" topology cuts, line 4. These cuts contribute a factor of ~2 x 10^2 to background reduction, and increase the signal to noise ratio to a respectable 3:1.

The present LENS technology and strategies have resulted in an overall ^{115}In background reduction by a factor of ~6 x 10^{11} at a signal loss cost of a factor of ~1.6, demonstrating that the famous LENS ^{115}In background problem is manageable.

A new cut strategy in the LENS analysis led to major improvements in the overall LENS detection efficiency. Fige (bottom pane) shows that the background is suppressed by different factors dependent on the size of N_{hit}. Larger values of N_{hit} yield larger reductions. Thus events are first grouped according to the factor N_{hit}. Different cut patterns are then applied for different values of N_{hit}, relaxing constraints as N_{hit} increases. The procedure results in increasing the overall efficiency to ~64% from early estimates as low as 11% in 2003.

The LENS detector has been optimized via the Monte Carlo work discussed above. Based on input parameters of 8% wt ^{115}In in liquid scinitillator, $L_{1/e}$ = 10m, Y(InLS) = 9000 hν/MeV, and scintillation detection efficiency = 900 pe/MeV. Tabe presents design parameters (size, mass, count rate, etc) for full scale LENS based on the input parameters..

5.1.2 UTK and Daughter Internal Backgrounds

Backgrounds from the primordial radio nuclides Uranium, Thorium, Potassium, and their daughters (UTK) will be present in some degree in the scintillator, and scintillation lattice construction materials. The first step to understanding the performance of the LENS detector with regards to these backgrounds is to quantify the levels of each background isotope in the scintillator and lattice materials. VT has two germanium detectors underground at the Kimballton Underground Research Facility (KURF) near Virginia Tech, and we have started a queue of materials (Teflon, Acrylic, InLS, and all liquids involved in InLS synthesis) to count for radiopurity in these detectors. Once these levels are known we will run Monte Carlo simulations to find out

the detector response to each decay mode, and run through the same cut sequence outlined in It is important to note—these simulations were run prior to the development of the SL and have optimistic assumptions regarding attenuation length of SL films, light yield (including no quenching), detector size. The LENS collaboration is currently working on updated simulations using measured parameters for multiple detector designs.
5.1.1 Indium Induced Backgrounds.

5.2 External

As with the UTK backgrounds discussed in 5.1.2 UTK and Daughter Internal Backgrounds, the first step to understanding the performance of the LENS detector with regards to external backgrounds is to quantify the rates and types of backgrounds in the environment around the detector. This includes backgrounds from the vessel, PMTs, cosmogenics, rock walls of the experimental hall, and shielding. These materials will be counted for radiopurity in germanium detectors at KURF near Virginia Tech. As stated before, the first step in analyzing these backgrounds is to quantify the level of radiation from each source

Chapter 6: Kimballton Underground Research Facility (KURF)

KURF is an underground laboratory operated by Virginia Tech Physics Department. [67] The Kimballton mine operated by Chemical lime [68] is a high purity limestone mine with large caverns suitable for housing underground physics experiments. The site was one of five considered in the selection process for the Deep Underground Science and Engineering Laboratory (DUSEL) in the USA. Although the site was not selected for DUSEL, Virginia Tech has continued to pursue the site as a facility for small underground experiments and prototypes targeted for DUSEL in the Homestake Mine in Lead, SD, USA. [69] [70] As a result, KURF is the only underground science laboratory on the east coast of the US, and is quickly becoming a leader in underground science research.

Figure 60 Kimballton Underground Research Facility (KURF) near Virginia Tech. S. Derek Rountree and R. Bruce Vogelaar in KURF during construction. The inclosure is 40'x100' and 20' high at the roof's peak.

Radio Nuclide	KURF Sample 1 (Bq/kg)	KURF Sample 2 (Bq/kg)	LNGS (Bq/kg)
^{40}K	18±1	13±1	15
^{226}Ra	1.2±0.1	1.9±0.2	5
^{232}Th	0.6±0.1	0.9±0.2	0.3
^{222}Rn	14.8 Bq/m^3		40-70 Bq/m^3

Table 14 KURF radioactivity measurements with radioactivity measurments from LNGS for comparison.

6.1 KURF Radiopurity

Underground physics is generally concerned with the level of natural radioactivity of the surrounding rock, since it may require significant amounts of shielding to reduce to appropriate levels. Two samples of limestone from the KURF area were measured at the Max Plank Institut für Kernphysik in Heidelberg Germany the results are reported in along with radon concentrations measured by the mine in compliance with Mine Safety and Health Administration (MSHA) requirements. In comparison to the KURF radioactivity measurements Laboratori Nazionali del Gran Sasso (LNGS), the foremost underground user facility in the world, radioactivity

measurements are reported are reported alongside KURF's. KURF radiopurity measurements are comparable to LNGS with lower ^{222}Rn, making it a suitable location for low background experiments.

6.2 Science at KURF

The driving force behind the KURF facility was a site for the LENS prototype miniLENS; however the facility was designed with the ability to house other experiments as well, including double beta decay [71] [72], low background counting [73], and dark matter searches.

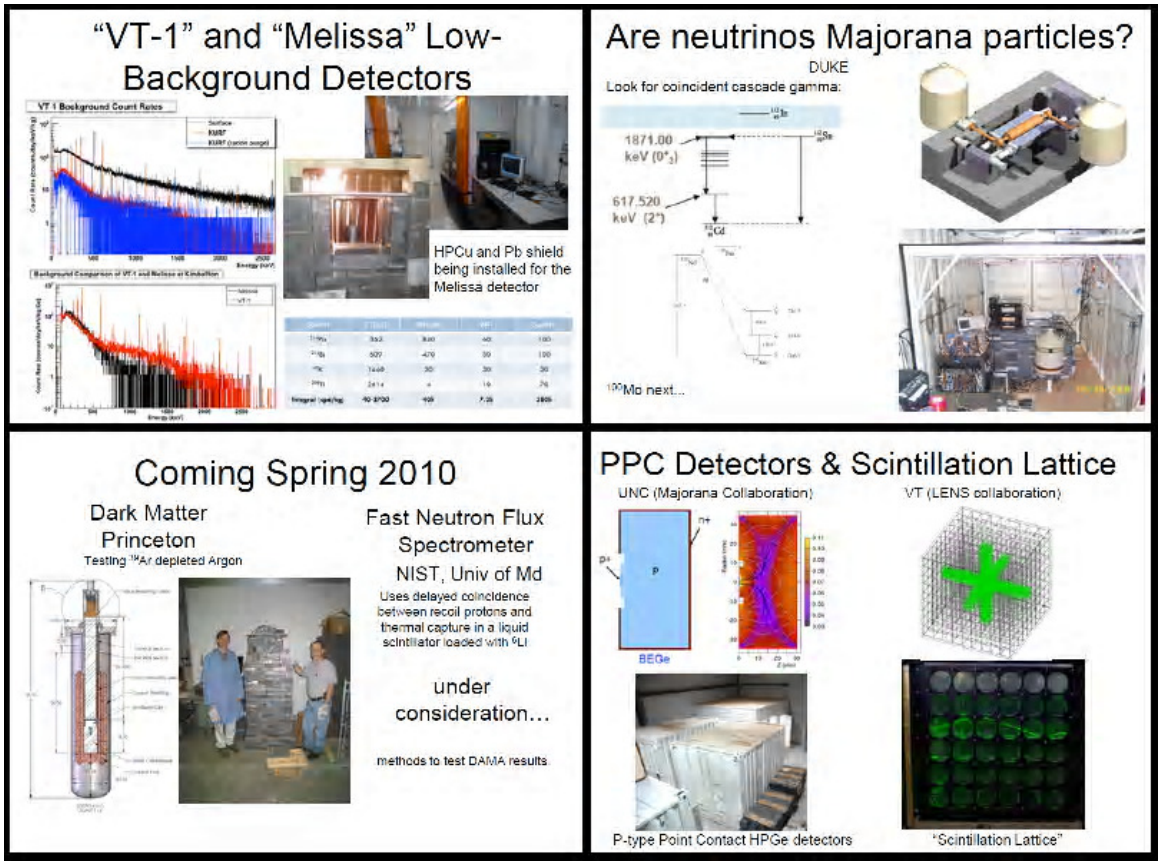

Figure 61 Science experiments at KURF. Top left: Low background counting Ge detectors for material assay. Top right: Experiments from DUKE exploring the Majorana nature of neutrinos. [71] [72] Bottom left upcoming experiments at KURF. Bottom right: PPC detector prototypes for the Majorana collaboration and LENS Scintillation Lattice. Pictures taken from **(78)**

Chapter 7: MiniLENS

As a feasibility test for LENS we are constructing a small prototype, miniLENS. While miniLENS's small scale will prohibit solar neutrino detection, it will allow us to test the scintillation lattice optics, characterize the background and detector response due to indium, and benchmark the MiniLENS and LENS Monte Carlo Simulations. The design choices are based on laboratory test results, simulations, and well-known electronic and engineering principles; however, only implementation of a well designed prototype can confirm these designs for a scale up to LENS. [74]

7.1 MiniLENS Tasks

Stage I of the miniLENS program is complete construction of miniLENS, installation of major systems (the detector, OLS handling systems, and electronics) in KURF, and filling miniLENS with non Indium LAB.

Stage II will be the initial miniLENS run with LAB. We will operate a fully multiplexed data acquisition system with external trigger, develop event analysis software, study spectroscopic features with external sources, measure background rates in KURF (thus allowing us to specify shielding needs), characterized background topologies, benchmark the miniLENS and LENS Monte-Carlo simulations, and produce InLS for the next run cycle.

Stage III-a will begin by draining the detector and filling it with InLAB (we will run two stages the first with InLAB and the second with InPC), calibrate the detector with Indium b-decay, analyze event topology and background rejection efficiencies, and continue benchmarking simulations.

Stage III-b will replace InLAB with InPC giving us a full understanding of miniLENS with the two lead OLS candidates for InLS.

In parrallel to these stages of miniLENS the LENS collaboration will continue work on a trigger scheme for LENS, InOLSs improvements, and other SL construction methods and improvements. Any of these parrallel projects may be incorporated and tested in the miniLENS project.

7.2 Mechanical Design

The scintillation lattice, see Chapter 4: Scintillation Lattice (SL), as the basic detector design is key to the LENS experiment. Monte Carlo models of LENS and miniLENS have been studied to determine the best choices for cell size and lattice material. We found that an $(8cm)^3$ cell provides the proper balance between selective event topology based on the gamma cascade and light loss due to the number of optical boundaries (Fresnel reflections resulting in increase effective path length and bulk absorption). We also studied the difference in index of refraction materials for lattice construction, and indicated the best solution to be Teflon FEP (TFEP) thin films. The TFEP films (n=1.33) give a critical angle of ~62^o which results in ~60% of isotropically emitted light to be channeled (sufficient for event localization and topology determination), and the unchanneled light mostly follows a direct path to the edge of the detector resulting in greater total light collection than if we were to use air as an index barrier, Figure 62.

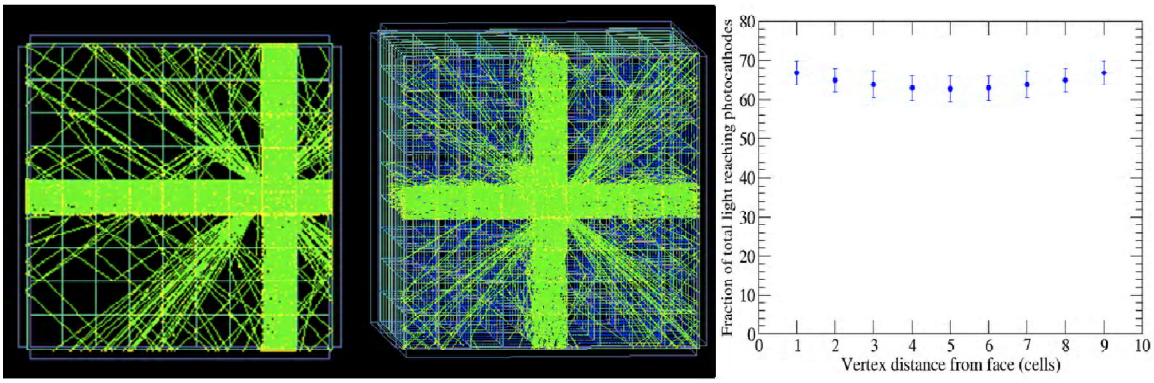

Figure 62 Geant4 simulations for miniLENS. Shown in green are photon traces through the miniLENS detector for a single event from two different viewpoints (left and middle). The fraction of the total photons produced that reach any PMT photocathode verses vertex distance from detector face is plotted (right). Reproduced from Ref. **(74)**.

Another study was made to determine the need or lack thereof for an active non-Indium loaded exterior buffer region in the detector. While this approach decreases the cost of the detector, there are significant difficulties in segmenting the detector to allow separation of Indium loaded scintillator and non-loaded scintillator. The study concluded that the fiducial volume is not significantly increased by the active buffer as events near the edge have a high probability of being rejected either way, and we are therefore moving forward constructing a homogenous detector with only InOLS.

The miniLENS final design is a 9x9x9 array of cubic cells (8.25cm on a side), approximately 0.0338% the volume being considered for LENS. The miniLENS design mimics the planned construction of LENS in every practical sense to make the scalability as straight forward as possible.

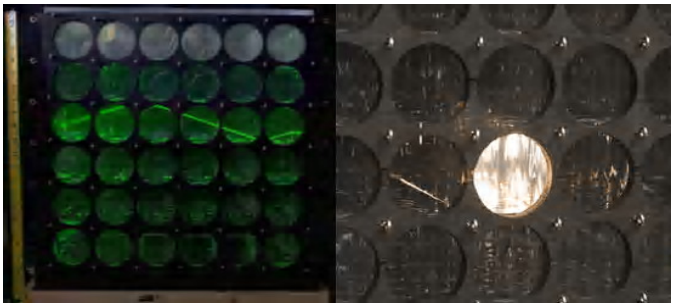

Figure 63 microLENS is a test model that was constructed to test the construction methods for the miniLENS detector. The lattice is $(8.25cm)^3$, and is made with Teflon FEP tacked to thin acrylic using a stapling method. Note the excellent light channeling.

7.2.1 Scintillation Lattice

The lattice for miniLENS has been tested and prototyped, Figure 63. Due to the light attenuation of TFEP ($L_{1/e}$~0.3cm) we use 50μm film. The mechanical structure is provided by tacking the TFEP to 0.4mm acrylic sheets. We use the abbreviation TA to denote one of these composite layers. Both materials are compatible with LAB based In-LS. The base lattice is built by laser cutting the TFEP and Acrylic into 'combs', then tacking these together to create TA 'combs'. Sixteen of these combs (8 combs perpendicular to the other 8) are then interlocked to form a 9x9 array of cubic cells. Finally nine of the 9x9 arrays are stacked with TA planes separating them to create the completed 9x9x9 lattice.

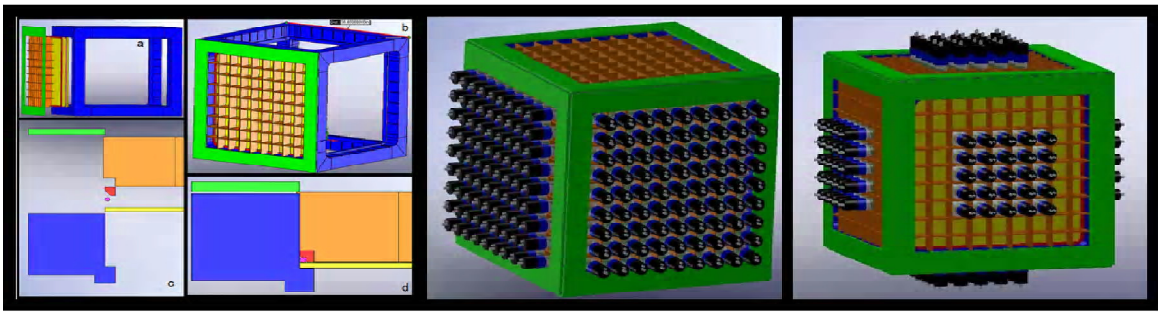

Figure 64 miniLENS Vessel. One side of miniLENS vessel assembly (left). Left c&d show a cross-section of how the detector is sealed. In yellow is the acrylic panel, followed by an o-ring (pink) with an o-ring compression plate (red). The PMT mounting lattice (orange) holds the o-ring compression plate in place, and the PMT mounting lattice is held against the acrylic plane via a compression plate (green). Middle, miniLENS with 162 PMTs fully instrumenting two sides. Right, 150 PMTs instrumenting the 5x5 core of miniLENS.

7.2.2 Containment Vessel

The miniLENS lattice and liquid scintillator will be contained in a UV transparent acrylic vessel, consisting of a metal frame to which six planes of acrylic are sealed via gasket compression. The compression is supplied over the entire surface of the plane by the PMT mounting grid, Figure 64. All six sides are removable, thus providing for good access to the scintillation lattice construction. In addition, external access to the PMTs allows us to test multiple configurations, Figure 64 middle and right, and to compare them with simulations. We are also able to replace faulty PMTs with great ease.

While the radiopurity requirements for LENS are three orders of magnitude lower than those of Borexino, the numerous number of surfaces in LENS require that the scintillation lattice and vessel be assembled in a dust free environment to maintain the best light transmission possible.

Oxygen is a major light quencher in OLS in particular InOLS. Therefore, we will displace the air in the detector with Argon gas prior to filling with scintillator. Argon is heavier than air and provides a true displacement of the air in the detector opposed to a simple nitrogen flushing. Once the detector is filled with Argon, we begin slow bottom filling with scintillator to avoid undue stress to the scintillation lattice.

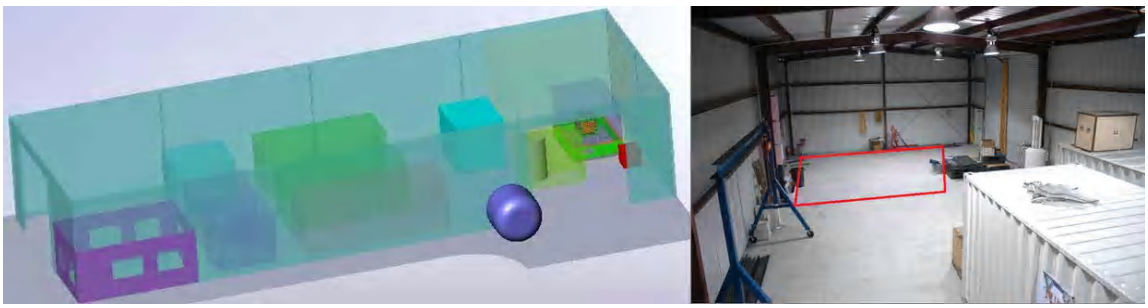

Figure 65 Placement of miniLENS in KURF. Drawn here is a solid model of KURF with experiments (left). On the right side of the model is the miniLENS clean area housing the shielding, dark box, and miniLENS. The picture is an elevated shot from the front of the building (right). The red box is the approximate footprint and location of the miniLENS experiment and infrastructure.

7.2.3 Environment

The miniLENS detector will be constructed and housed in a custom clean area in the Kimballton Underground Research Facillity in Ripplemead, Va, Figure 65 (~30 minute drive from Virginia Tech). Within the clean area we will have 15cm of steel shielding covering the floor space of the detector. On top of the steel shielding will be a

secondary knee high containment vessel (spill tank) with HV, BNC, and piping feed throughs towards the top. An open bottom box will extend up from this knee high vessel creating a light tight box. We will be able to lift the top portion of the box vertically to allow access to the detector.

7.3 Organic Liquid Scintillator (OLS) for MiniLENS

The miniLENS experiment will run with three phases of scintillator, LAB, InLAB, and InPC. This section, will discuss the components of both scintillators, the procurement of materials, fluid handling, quality control, radiopurity, material compatibility monitoring, system installation, and filling procedures.

7.3.1 Linear Alkylbenzene Scintillator (LAB)

The pure scintillator phase of the detector will be filled with Linear Alkylbenzene (LAB) scintillator. The scintillator will consist of 15g/L 2,5-Diphenyloxazole (PPO) and 3mg/L p-Bis(o-methylstyryl)benzene (Bis-MSB). The PPO and Bis-MSB will be dissolved in pseudo cumene such that the final scintillator contains 12.5mL/L of the pseudo cumene and fluor solution in LAB.

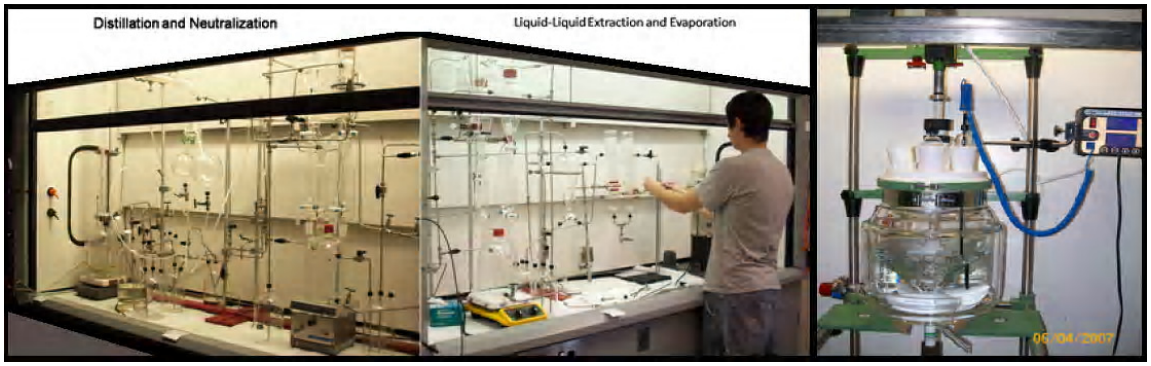

Figure 66 Metal Loaded Liquid scintillator synthesis systems. Left, undergraduate Micah Eassa works on the InLAB anaerobic synthesis system at Virginia Tech. From left to right in the system are modules for distillation, neutralization, liquid-liquid extraction, and hexane evaporation. Right is the BNL continuous extraction reactor.

7.3.2 InOLS (InLAB and InPC) for MiniLENS

An anaerobic continuous chemical synthesis apparatus for InOLS has been built at Virginia Tech, Figure 66 left. This facility is designed for production on the liter scale, and is primarily charged with bench tests and optimization of synthesis procedures.

A reactor for continuous solvent-extraction used at Brookhaven National Laboratory, Figure 66 right, will be used in the preparation of hundreds of liters of InLS for miniLENS (410L).

These facilities will also perform synthesis module studies as a prelude to development of an industrial scale system capable of producing a few tons per batch for LENS. See

Chapter 3: Metal Loaded Organic Liquid Scintillator (MLLS) Technology for details of InOLS chemical synthesis.

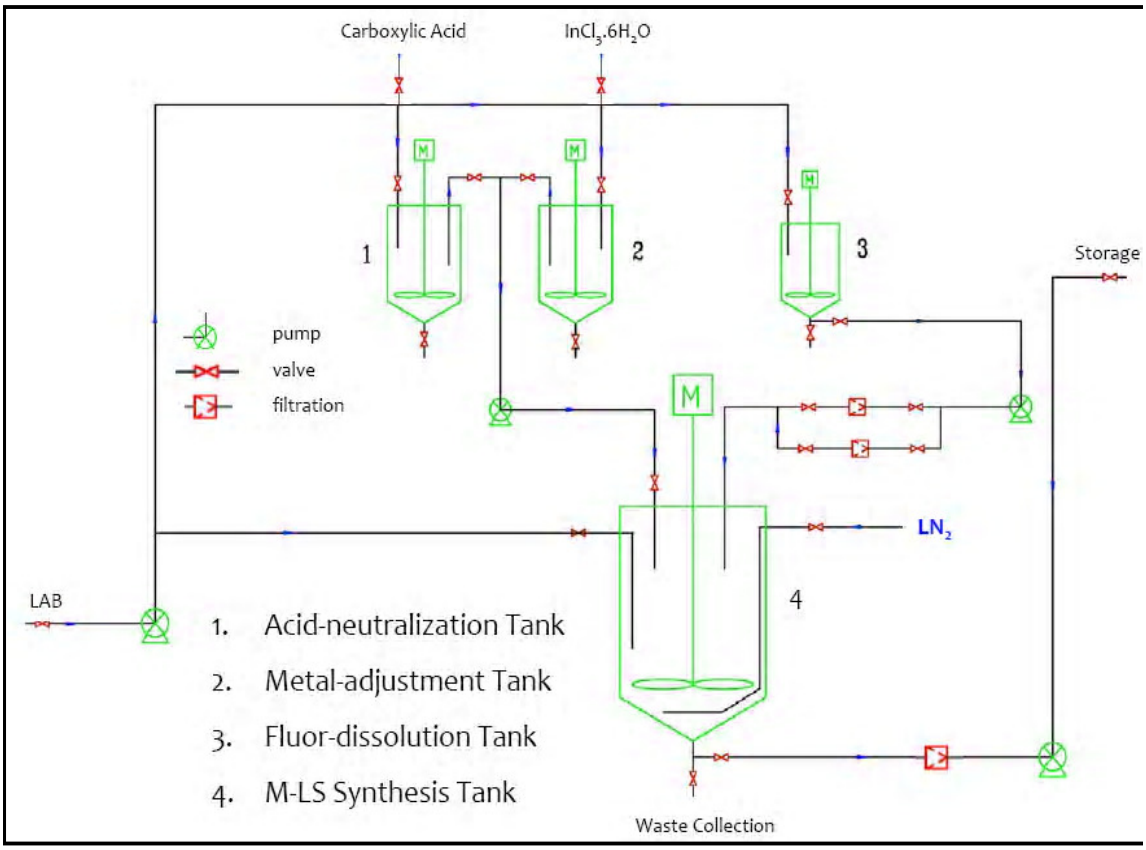

Figure 67 Indium Liquid Scintillator synthesis flow chart. Reproduced from Ref. **(74)**

7.3.3 Procurement and Quality Control of Materials, and Fluid Handling

Indium chloride ($InCl_3$), 2-methylvaleric acid (HMVA), PC and LAB are the basic components of the In-LS. It's known that chemical qualities from different suppliers often behave differently due to variances in commercial production methods. The differences in the raw materials could impact the quality of the synthesized InOLS.

We are in the process of testing samples from different vendors, and developing quality-assurance (QA) criteria for bulk chemical acceptance which will be implemented at the InLS plant as a result.

After acquiring all chemical ingredients, three main production phases for miniLENS are proposed:

1) Purification of the starting chemicals,

2) pH adjustment of HMVA with ammonium hydroxide to produce carboxylate anions that can complex the indium cations
3) Synthesis of the In-MVA complex that is immediately dissolved in OLS.

Specific chemical ingredients need pH adjustments before synthesis:

1) HMVA neutralization with NH_4OH
2) $InCl_3$ modification, with NH_4OH and HCl as needed.

Two reaction vessels, numbered 1 and 2 in Figure 67, equipped with pH and temperature monitoring sensors, are connected to provide liquid and ultra high purity N_2 transport. These vessels are engineered to handle the liquids in miniLENS InLS production**.**

Key known issues for miniLENS liquid handling are: storage of tens to hundreds of liters of feed chemicals, i.e., HMVA, $InCl_3$ and LAB before and after purification and hundreds of liters of synthesized In-LS before filling of the detector vessel, all under controlled ambience/atmosphere; and logistics of transporting In-LS at constant temperature from BNL to KURF.

7.3.4 Radiopurity

We are developing an extensive radioactive counting plan for all materials in miniLENS to be implemented using germanium detectors at KURF. We will count samples of all raw chemical materials as well as radio purified materials and the final InLS.

Traditional methods of radio purifying materials such as ion exchange and solvent washing for removal of U and Th in aqueous raw materials have been considered; however, these methods require long chemical operation and high material costs. Therefore, we are limiting radio purification to a self-scavenging method developed at BNL using simple chemical preparations and no additional chemicals. This method is highly effective at removing Th from lanthanide-chloride compounds, and will be applied to clean the $InCl_3$ compounds for miniLENS InLS production.

7.3.5 Material Compatibility Monitoring

An ongoing material compatibility test program has been set up at BNL for miniLENS. The goal is to confirm long-term compatibility of the organic liquids with the contacted materials. These materials are the:

1) Optical cage material (Acrylic and Teflon)
2) Storage tanks
3) Detector vessels
4) Calibration units
5) Fluid and gas piping

Two main considerations are:

1) The effects of the liquids on the contacted materials
2) The impact of leaching from the materials into the liquids.

7.3.6 Filling and Installation

As noted at the beginning of this chapter miniLENS operations will follow a two-phase sequence. In the first year we will use unloaded LAB scintillator and in the second year InLAB. If the second year of operations indicates a need for a buffer region of pure unloaded scintillator, we will implement the necessary detector modifications in year three. For either unloaded LAB or InLAB scintillator anaerobicity in all phases of production, storage, handling, and transportation is mandatory.

The plan is to produce the scintillator for both phases, as nearly completely as possible, at BNL and then transport the scintillator to KURF. A surface trailer will be installed for temporary storage and preliminary measurements before transferring the scintillator material underground. The last stage of assembly of the miniLENS detector is the filling and installation. The scintillator storage tanks will be outfitted with exit ports that will connect to a centralized, instrumented system with plumbing designed to allow filling. The details of the filling procedure and monitoring tools are being developed.

Some additional considerations are secondary containment in case of leakage or spills (the detector itself is housed in a knee wall containment vessel, 7.2.3 Environment) of the liquids and local monthly temperature variations for best timing of detector filling.

7.4 Data Acquisition and Electronics

MiniLENS requires a flexible, cost-effective data acquisition (DAQ) system for the program of measurements; however, miniLENS also provides a

Figure 68 Photonis XP3300 PMT with base. This is the PMT model that will be used for miniLENS

platform for developing and testing more sophisticated triggering schemes and DAQ architectures that would be well suited for the full scale LENS detector. Keeping these factors in mind, we have developed an approach to miniLENS electronics that while intrinsically not scalable to LENS, balances near-term miniLENS requirements and provides a powerful framework for the development of full scale LENS DAQ and electronics.

7.4.1 PMTs

One hundred fifty three-inch photonis XP3300 PMTs, Figure 68, have been purchased for miniLENS. These are 10-stage tubes with bi-alkali photocathodes. They have gain of ~10^6 and low potassium borosilicate glass windows. The PMT signal rise time is still being looked at, but preliminary results suggest it is ~15ns. While we do not currently have enough tubes to fully instrument the detector, with an additional 12 tubes and modest electronics, see 7.4.2 Basic Structure for MiniLENS DAQ, we can instrument both arrangements in Figure 64 (the 6 side 5x5 can be done with current PMTs and electronics). Instrumenting two full sides is an important configuration as it allows for complete vertex characterization over the complete detector. A combination of various PMT arrangements will be studied to robustly benchmark our Monte Carlo simulation.

7.4.2 Basic Structure for MiniLENS DAQ

The basic structure developed for the miniLENS DAQ involves analog, time-delayed multiplexing of a few PMT signals into 500-MHz sampling VME ADCs. A relatively simple system (delay, multiplexing, hardware trigger and simple readout for 120 channels) is to be ready for integration with miniLENS during the fall of 2010. A simplified schematic representation is shown in Figure 69 along with oscilloscope output from the multiplexed signals. Fast sampling ADC's are important from an R&D perspective since they provide for acquisition and logging of full waveform data from each PMT; this "maximum information" approach is expected to enhance our understanding of the detector performance. Commercial ADC modules represent the single greatest expense in the electronics (~$800/channel), thus analog multiplexing was pursued as a means of allowing more PMT's to be implemented at a reduced cost, while retaining waveform information for each pulse. This approach, while tractable in

miniLENS due to the modest rates per channel and number of channels, is not scalable to LENS. However, detailed waveform information obtained in miniLENS will help in developing solutions for triggering and electronics for the full-scale LENS instrument.

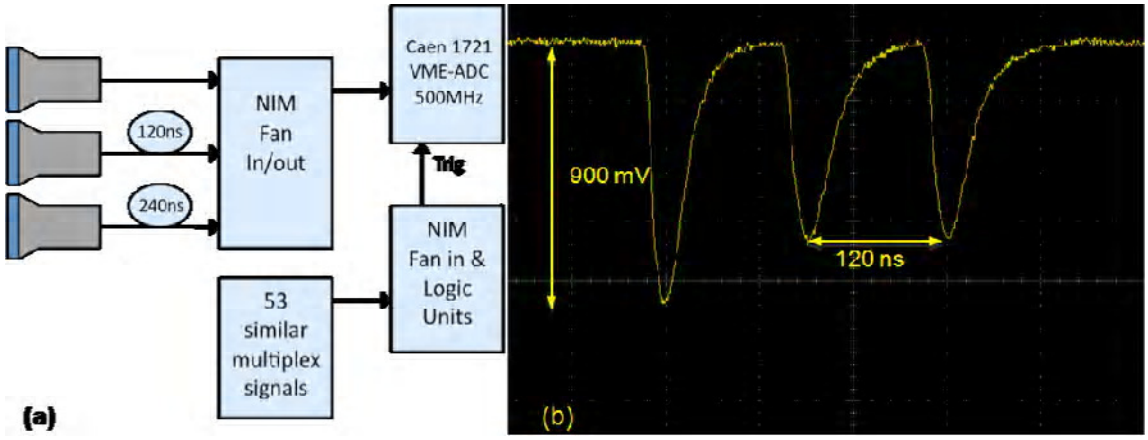

Figure 69 Basic miniLENS electronics approach. (a) Simplified schematic of the basic approach to the miniLENS data acquisition system, and (b) an analog multiplexing approach demonstration, 3 PMTs are combined looking at a signal from a ^{137}Cs source. Reproduced from Ref. **(74)**

As originally proposed, miniLENS was to be instrumented with 150 PMT's with 4 PMT's multiplexed into each digitizer channel. An analog multiplexing scheme was developed and demonstrated by the LSU group. While several approaches were investigated, a simple cable-delay scheme was selected because it is robust, straightforward, and cost-effective. However, measurements with the single light-channel prototype at LSU discovered that the combination of the scintillator response and reflections in the instrument require longer delay times than expected (more than 100 ns) in order to adequately distinguish multiplexed signals. Signal attenuation in the cable delay further exacerbates this problem. An example of 3 signals multiplexed using no delay, 120 ns, and 240 ns delay is shown in Figure 69, which also illustrates signal degradation. About 20% of the pulse amplitude is lost in the first 80 ns of cable delay, but the total charge is nearly constant. While the rise time of the pulse is lengthened, we find no loss in time resolution.

Given the demonstrated time width for multiplexed signals, there are significant concerns regarding multiplexing more than 3 signals per channel. This limits the total number of PMTs that can currently be instrumented to 120. While much of the initial miniLENS program can be conducted with this implementation, it does not allow full

instrumentation of two faces of the $(9\ \text{cell})^3$ miniLENS detector. This adversely impacts an important part of the program— understanding how the fiducial cut reduces the efficiency for real events— as this requires full topological reconstruction of the interior region with complete coverage of the outer fiducial volume; therefore, we intend to aquire addition electronics in the first year of miniLENS construction.

We have implemented a hardware trigger (external to the digitizers) based upon NIM fan in/outs and logic modules that can be easily modified for different measurements/configurations. This provides maximum flexibility for setting the trigger conditions and the most straightforward DAQ approach. The LSU group is currently developing a simple DAQ readout mode whereby waveforms from zero-suppressed channels are taken based upon the external hardware trigger. This system will be used for initial miniLENS operations, but the capabilities of this system are limited and all but the most basic analysis software will remain to be developed.

During the miniLENS construction phase, we will develop the miniLENS analysis routines for a variety of configurations both with and without indium-loading. We will also extend the DAQ to 162 channels and perform measurements with 2 full faces of miniLENS instrumented. The results of measurements will be compared to Monte Carlo simulations to characterize the performance of miniLENS.

We also propose to develop more sophisticated approaches to the DAQ and triggering that are scalable to larger geometries. Collaborators at the University of North Carolina and Indiana University will assist in these efforts. One obvious path for development is to program signal processing and triggering algorithms into the onboard FPGA's to greatly reduce the quantity of data transferred over the VME backplane. We will also explore alternate approaches, e.g. digitizing all signals in an inexpensive module like that being developed for SciBath and transferring digital information to a second-level event builder. We propose to develop these approaches to determine the most cost-effective path for a full-scale LENS implementation.

7.5 MiniLENS Operational Plan

The primary goals of miniLENS are to demonstrate the performance of the scintillation lattice and understand how the performance scales with detector size. We

have developed an operational plan for miniLENS to accomplish these goals through a variety of detector configurations which will benchmark Monte Carlo simulations. An integral part of this program involves regular calibration and performance monitoring, and a program of how measurements integrate with Monte Carlo simulation. The underground operational plan is broken into two major phases: 1) operations with unloaded LAB scintillator and 2) operations with InLAB. Within the two phases a plan of measurements is laid out.

7.5.1 Monitoring and Calibrations

The analysis scheme involves energy and timing cuts; therefore, regular time and charge calibration of the system is essential. In a similar application, in the Borexino experiment, a multiplexed system of optical fibers driven by a single diode laser was used to illuminate all of the PMTs. [75] We have adopted as a baseline this type of system for miniLENS, along with regular source calibrations.

7.5.2 Simmulation

A simulation package using GEANT4 has been developed and used extensively for the miniLENS experimental design. While we have laid out an experiment that performs well under simulation, and is relatively insensitive to input parameters (i.e. cell size, attenuation length, light output, etc), a complete understanding of the detector performance requires a better understanding of input parameters dealing with the lattice (mainly fraction of specular reflection from the Teflon film) which can only be gained through experimental measurements in miniLENS. The simulation package will be continually used and updated during the development and various runs of the miniLENS prototype. An upcoming key task of the simulation package will be to generate "fake data" in the same event format as real data and use it to benchmark both the robustness and speed of the data analysis engine.

7.5.3 Pure LAB Scintillator Measurement

A pure scintillator measurement will allow us to understand the performance of the scintillation lattice and internal and external backgrounds without the presence of the significant internal background from introducing indium. Measurements using gamma

and beta sources in various locations and with differing PMT configurations will be used to study light propagation and attenuation within the lattice. These measurements can be conducted with relatively modest PMT coverage, isolated to the regions of interest. By combining measurements using a number of configurations, we can come to a complete understanding of light propagation within the lattice.

Other prototypes using pure LAB scintillator are being used along with miniLENS. The primary goal of these prototypes is to understand the scintillation lattice construction; however, they have been constructed in a manner that they may be instrumented and used as pre-prototype detectors. LSU has constructed a 9x1x1 3.25" cell array, and VT has constructed a lattice test chamber that is a 6x6x6 3.25" cell cube, Figure 63. Measurements from these pre-prototype detectors will complement the miniLENS measurement by establishing how the as-built performance scales with increasing detector size.

Measurements directed toward understanding the external background have been shown to be of great importance in initial GEANT4 simulations dealing with PMT induced backgrounds in the full scale LENS detector. This measurement will also allow us to characterize the shielding needs for LENS. The external background measurements will require full coverage of the outer detector regions. This can be accomplished by fully instrumenting two full sides of the detector (162 PMTs).

7.5.4 (InLAB and InPC) InOLS Measurements

Measurements with InOLSs are the crucial step towards understanding the full performance of the instrument. Understanding the topology of the indium-decay background and the combination of this background with other background sources can only be accomplished through studies with InOLSs. Measurements with sources are also important with InOLSs to demonstrate the level of sensitivity with which the gamma cascade can be distinguished in the presence of the indium-decay background. For this program of measurements it will be important to fully instrument two complete detector faces so that the topology of different types of events can be accurately characterized. The ^{115}In beta spectrum also provides a precise internal energy calibration reference due to the fact that it is a unique fourth forbidden beta decay with a precisely known Q value.

7.5.5 'Proxy' Detection

After the completion of the LAB and InLAB phases of the detector runs, there are a few possibilities to demonstrate pp-ν like events in the detector. ^{115}Sn has a high spin isomer state at 713.6 keV with a lifetime of 231 μs, Figure 70, that decays by the emission of a 100.8 keV γ that is 5.7 times more likely to come out via a conversion electron than a pure γ. After the 713.6 keV state decays, the resulting state is the 7/2$^+$ state that we see in neutrino capture. This gives us a near perfect mimic for pp-ν events followed by the solar tag (the decay of Sn 7/2$^+$).

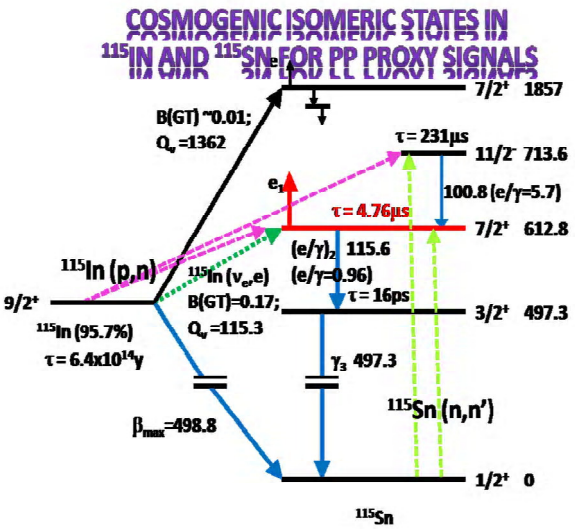

Figure 70 Cosmogenic isomeric states in ^{115}In and ^{115}Sn for pp proxy signals. The magenta lines show ^{115}In(p,n) reactions, and the light green shows ^{115}Sn(n,n') reactions.

The 11/2$^+$ state of ^{115}Sn can be passively reached by cosmic protons via ^{115}In(p,n); however, at a depth of 1400 mwe in KURF the flux of cosmic ray protons is not sufficient. Nevertheless we will look for these events during the InLAB phase of detector operation.

An active method of reaching the ^{115}Sn 11/2$^+$ state is to have an ^{115}Sn foil target in the detector and bring in external neutrons from a source. The ^{115}Sn 11/2$^+$ state is reached via the ^{115}Sn(n,n') reaction. The ^{115}Sn(n,n') reaction can be uniquely tagged by either recoil protons from the incident neutron and/or via In(n,γ) with σ=3000b.

This 100 keV pretaggable event looks identical to a pp-ν signal in energy and is followed by the same tag cascade as solar ν events. These events are sufficient to demonstrate solar neutrino signal detection in a high ^{115}In background. Since the formation of the proxy is identified, the tagged proxy signal rate directly measures the detection efficiency of the ν tag experimentally. This detection will allow for Monte-Carlo simulations to be further benchmarked.

The overall proxy detection method additionally serves to estimate the general neutron-induced background and possible interference with the solar ν tag. The proxy detection scheme will be further developed and needed resources will be identified during the construction phase of miniLENS.

Appendix A: Plastic Film Transmission and Other Optical Properties

The spectrums reported in Appendix A where measured in the LENS laboratory using a UV/Vis spectrometer with adjustable slide holders in the sample and reference beams, Figure 71.

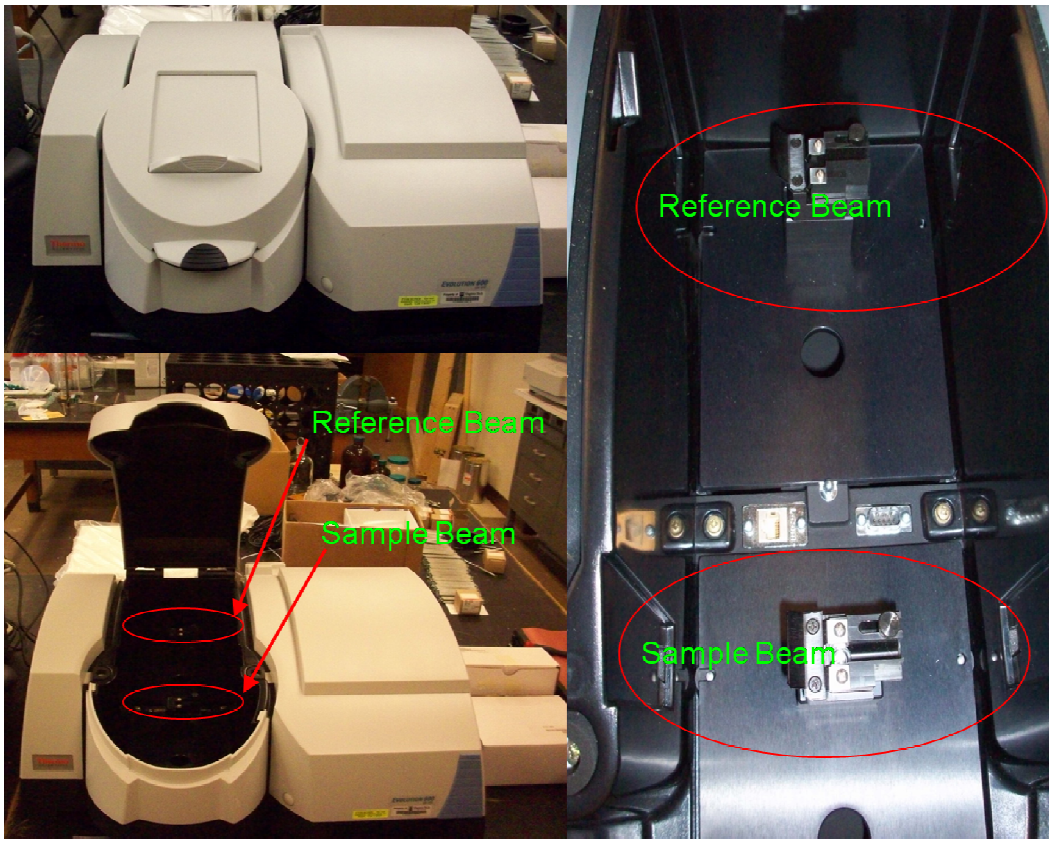

Figure 71 UV/Vis Spectrometer

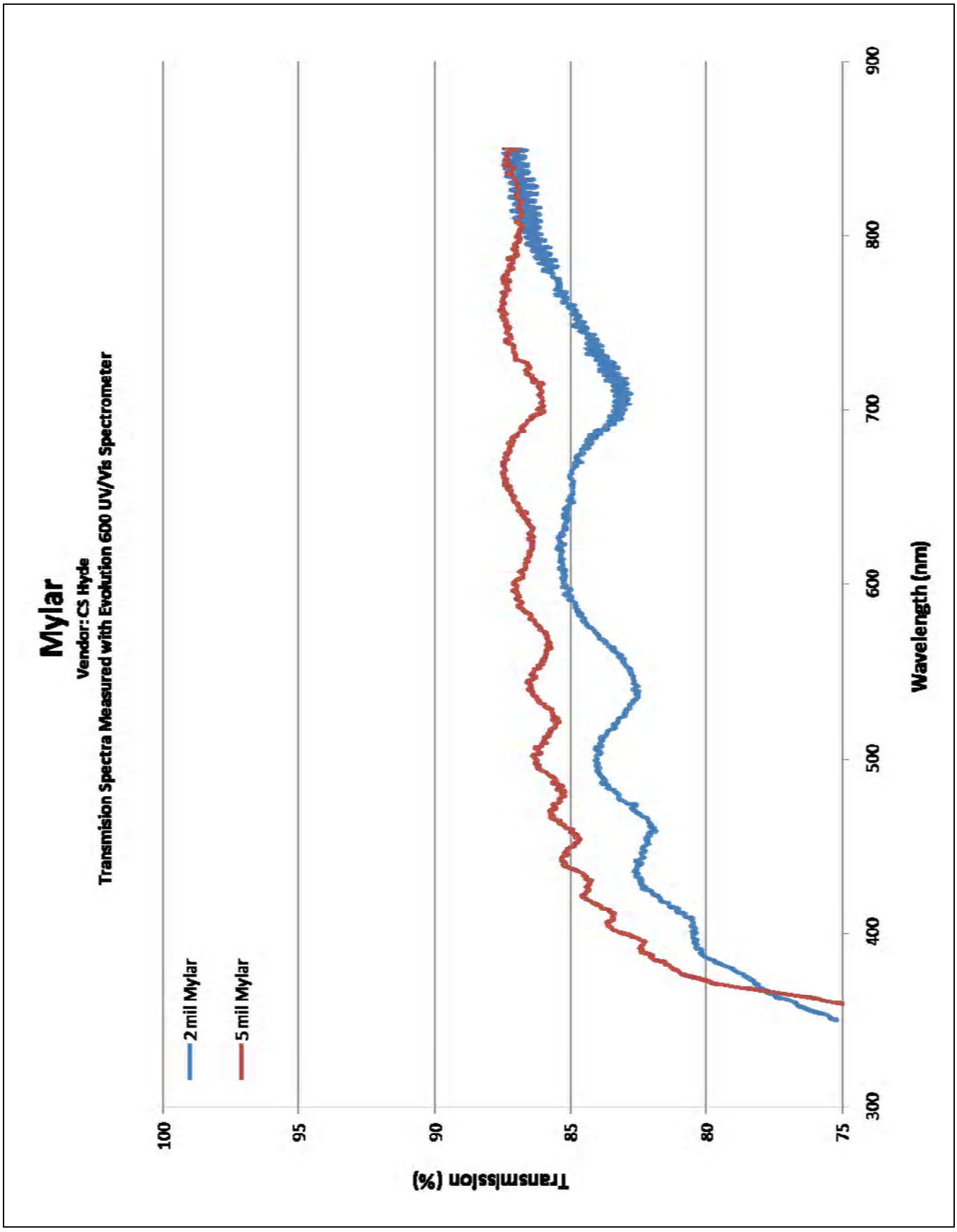
Mylar
Vendor: CS Hyde
Transmission Spectra Measured with Evolution 600 UV/Vis Spectrometer
2 mil Mylar
5 mil Mylar
100
95
90
85
80
75
Transmission (%)
300
400
500
600
700
800
900
Wavelength (nm)

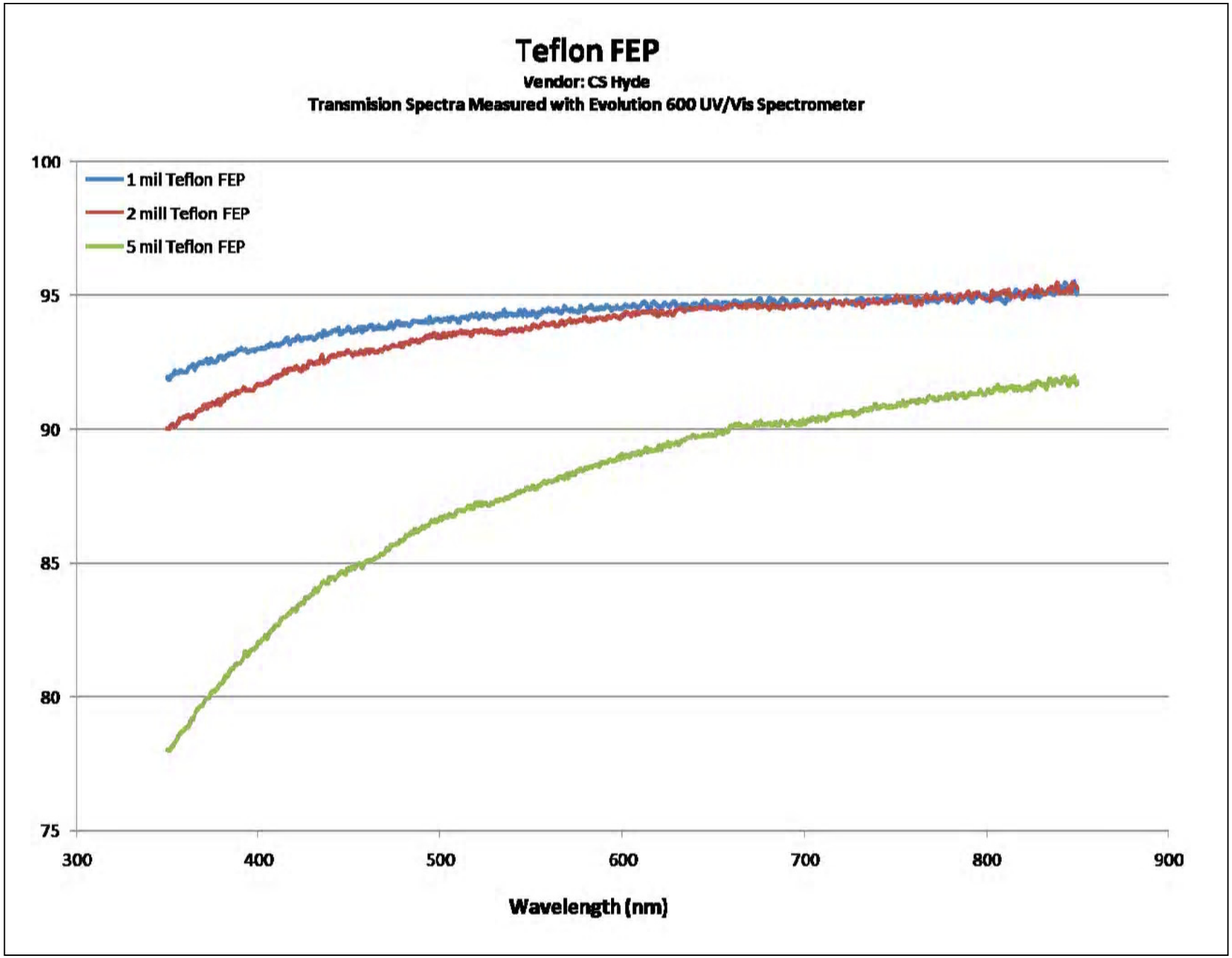
Teflon FEP
Vendor: CS Hyde
Transmision Spectra Measured with Evolution 600 UV/Vis Spectrometer
1 mil Teflon FEP
2 mill Teflon FEP
5 mil Teflon FEP
100
95
90
85
80
75
300
400
500
600
700
800
900
Wavelength (nm)

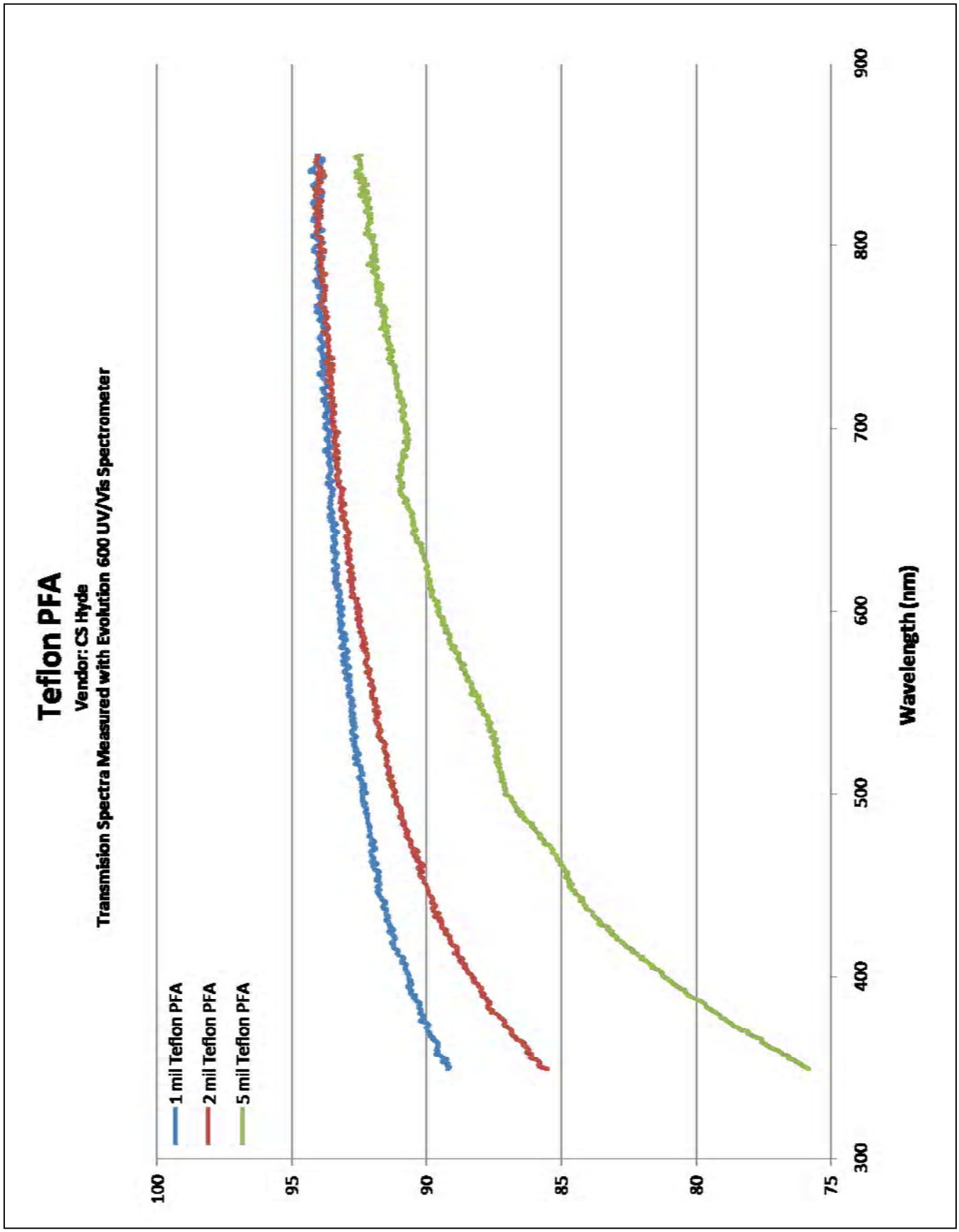
Teflon PFA
Vendor: CS Hyde
Transmission Spectra Measured with Evolution 600 UV/Vis Spectrometer
1 mil Teflon PFA
2 mil Teflon PFA
5 mil Teflon PFA
100
95
90
85
80
75
300
400
500
600
700
800
900
Wavelength (nm)

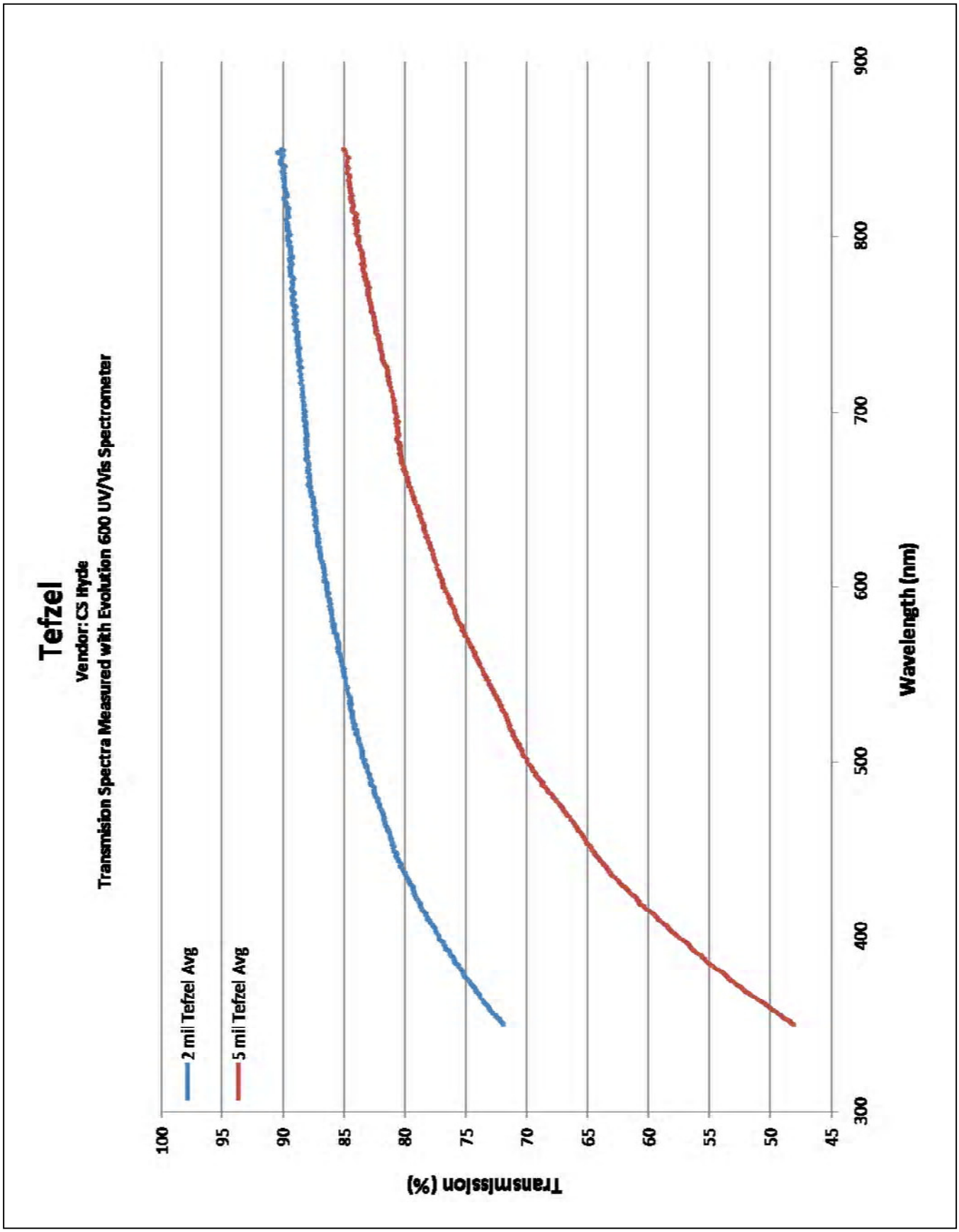
Tefzel
Vendor: CS Hyde
Transmission Spectra Measured with Evolution 600 UV/Vis Spectrometer
2 mil Tefzel Avg
5 mil Tefzel Avg
Transmission (%)
100
95
90
85
80
75
70
65
60
55
50
45
Wavelength (nm)
300
400
500
600
700
800
900

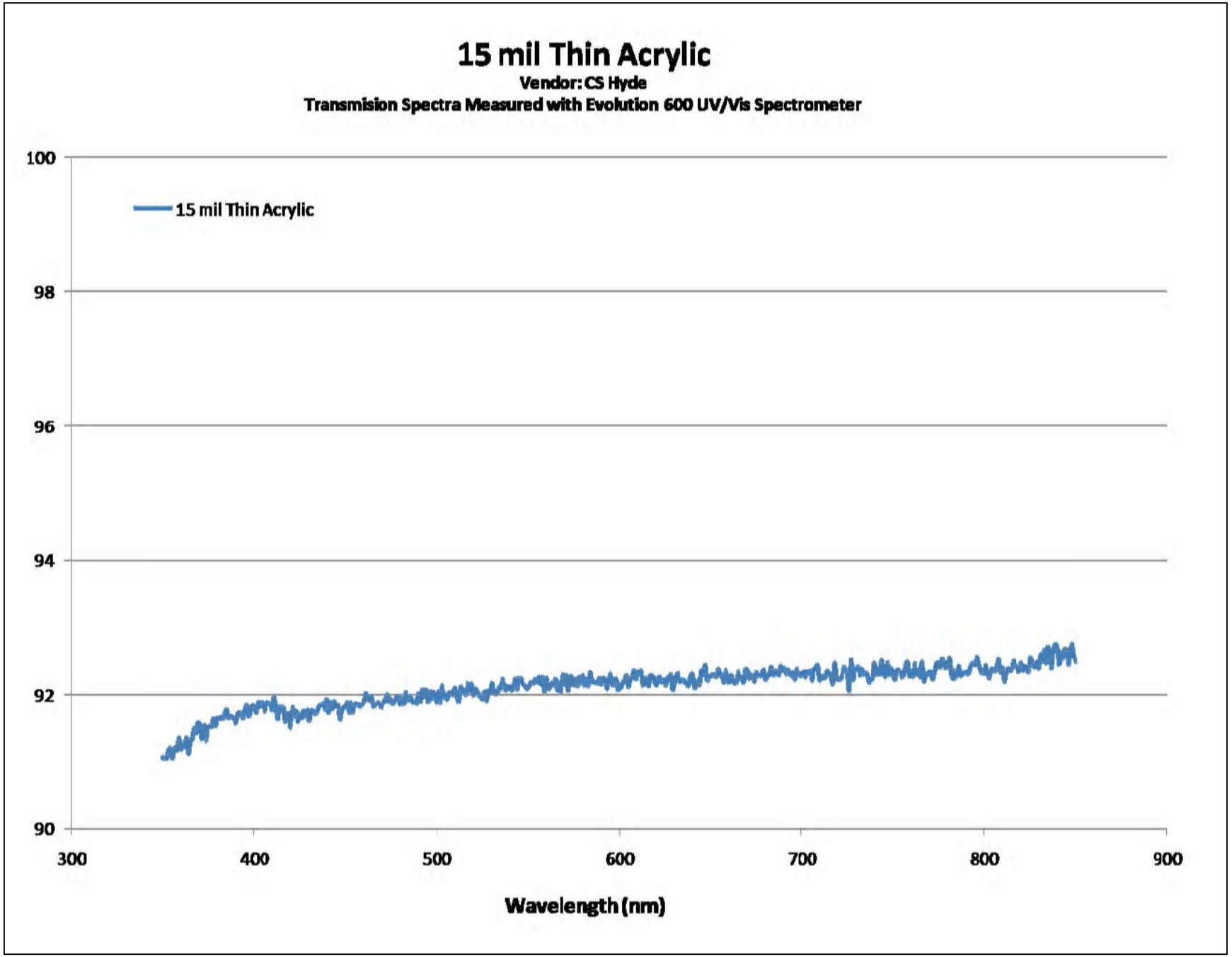
15 mil Thin Acrylic
Vendor: CS Hyde
Transmision Spectra Measured with Evolution 600 UV/Vis Spectrometer
15 mil Thin Acrylic
100
98
96
94
92
90
300
400
500
600
700
800
900
Wavelength (nm)

Appendix B: Indium Liquid Scintillator Recipes

BNL (Raghavan) Recipe--

Step I: Neutralization

1. Mix 2-Methylvaleric Acid (HMVA) and NH_4OH and H_2O in the proportions of Table 1. This reaction is exothermic; wait for the resulting solution to cool to room temperature

Step II: In-line purification

2. Add equal volume of Toluene containing 50g/L TBPO
3. Stir for maximum mixing for 10 min
4. Transfer to separatory funnel and drain off water phase. Discard Toluene phase.
5. Repeat 2 through 4 with fresh Toluene + TBPO
6. Measure pH, pH_1, of purified water phase.

Step III: Add PC to purified aqueous solution

Step IV: Extraction

7. Purify Indium Corporation of America $InCl_3$ solution (ICA) with Toluene + TBPO. Due to the high density difference this must be done according to James Bond: "shaken, not stirred!"
8. Add purified ICA to water phase ~2mL at a time with the water phase + PC stirred at high speed to maximize surface area between the two solutions. Each time ICA is added a white turgidity appears and within ~15 seconds disappears, dissolving in the PC completely. The total solution under stirring then becomes as clear as an organic + water emulsion.
9. Continue adding ICA till complete. The whole process on the 50mM scale takes ~30min.
10. Transfer to separatory funnel. Wait for 30 min until all bubbles disappear and a clean clear phase separation occurs. Bubbling and foaming is a problem at $pH_{extraction}$ >6.7, thus the range measured in Fig. 3 is below this pH.
11. Remove water phase (this will be at the bottom of the funnel for the above Indium concentration).
12. Measure water phase $pH_{extraction}$ and density. For 100% Indium transfer, the density should be ~1.0, for no Indium transfer (which is increasingly possible for $pH_{extraction}$~4) the water density is ~1.1.

Step V: Dehydration

13. Drain organic phase (slightly more viscous than unloaded PC) into filter paper (Wattman #2 paper) with Na_2SO_4 powder (granular crystals from Aldrich). The typical yield of ~65g takes about 20 min to filter out.
14. Measure density of organic phase, ~.96g/mL The final solution should be crystal clear.

Step VI: Scintillator

15. Add Bis-MSB. Because of the small quantity, prepare beforehand a solution of PC + MSB with 1mg MSB/mL solution. Typically the InLS from #13,14 needs about 0.5 mg of this solution for InLS stock of ~35g.
16. Add pTP at 3g/L of final InLS (105mg for 35g InLS). Dissolve under stirring. This takes a long time (several hours).

VT (Zheng) Recipe
Differences from BNL Recipe are highlighted in yellow.
Step I: Neutralization
1. Mix 2-Methylvaleric Acid (HMVA) and NH_4OH and H_2O in the proportions of Table 1. This reaction is exothermic; wait for the resulting solution to cool to room temperature

Step II: In-line purification
2. Add equal volume of Toluene containing 0.5g/L TBPO
3. Stir for maximum mixing for 10 min
4. Transfer to separatory funnel and drain off water phase. Discard Toluene phase.
5. Repeat 2 through 4 with fresh Toluene + TBPO
6. Measure pH, pH_1, of purified water phase.

Step III: Add Hexane to purified aqueous solution

Step IV: Extraction
7. Purify Indium Corporation of America $InCl_3$ solution (ICA) with Toluene + TBPO. Due to the high density difference this must be done according to James Bond: "shaken, not stirred!"
8. Mix Ammonium Acetate and water.
9. Add purified ICA simultaneously with Ammonium Acetate to water phase ~2mL at a time with the water phase + Hexane stirred at high speed to maximize surface area between the two solutions. Each time ICA is added a white turgidity appears and within ~15 seconds disappears, dissolving in the Hexane completely. The total solution under stirring then becomes as clear as an organic + water emulsion.
10. Continue adding ICA till complete. The whole process on the 50mM scale takes ~30min.
11. Transfer to separatory funnel. Wait for 30 min until all bubbles disappear and a clean clear phase separation occurs.
12. Remove water phase (this will be at the bottom of the funnel for the above Indium concentration).
13. Measure water phase $pH_{extraction}$ and density. For 100% Indium transfer, the density should be ~1.0, for no Indium transfer (which is increasingly possible for $pH_{extraction}$~4) the water density is ~1.1.

Step V: Evaporation
14. Put the solution into a Rota vapor, pull vacuum on the solution, and allow the hexane to evaporate.
15. Once "crystals" form place solid CO_2 around the Rota vapor bulb, and freeze dry the "crystals." Note, the solid looks crystalline, but has no crystal structure when viewed with crystallography equipment.
16. Weigh solid.

Step V: Dissolve solid Indium $HMVA_2$ OH in PC
17. Dissolve Indium $HMVA_2$ OH in PC.
18. Measure density of solution. For $8\%_{wt}$ Indium solution, the density should be ~0.96mg/mL

Step VI: Scintillator
19. Add Bis-MSB. Because of the small quantity, prepare beforehand a solution of PC + MSB with 1.2 mg MSB/mL solution. Typically the InLS from #18 needs about 0.25mL of this solution for InLS stock of 20mL.
20. Add ~3g/L PPO

VT (Rountree and Raghavan) Recipe
Differences from VT (Zheng.) Recipe are highlighted in blue.
Step I: Neutralization
1. Mix 2-Methylvaleric Acid (HMVA) and NH_4OH and H_2O in the proportions of Table 1. This reaction is exothermic; wait for the resulting solution to cool to room temperature

Step II: In-line purification
2. Add equal volume of Toluene containing 0.5g/L TBPO
3. Stir for maximum mixing for 10 min
4. Transfer to separatory funnel and drain off water phase. Discard Toluene phase.
5. Repeat 2 through 4 with fresh Toluene + TBPO
6. Measure pH, pH_1, of purified water phase.

Step III: Add Hexane to purified aqueous solution

Step IV: Extraction
7. Purify Indium Corporation of America $InCl_3$ solution (ICA) with Toluene + TBPO. Due to the high density difference this must be done according to James Bond: "shaken, not stirred!"
8. Add purified ICA to water phase ~2mL at a time with the water phase + Hexane stirred at high speed to maximize surface area between the two solutions. Each time ICA is added a white turgidity appears and within ~15 seconds disappears, dissolving in the Hexane completely. The total solution under stirring then becomes as clear as an organic + water emulsion.
9. Continue adding ICA till complete. The whole process on the 50mM scale takes ~30min.
10. Transfer to separatory funnel. Wait for 30 min until all bubbles disappear and a clean clear phase separation occurs.
11. Remove water phase (this will be at the bottom of the funnel for the above Indium concentration).
12. Measure water phase $pH_{extraction}$ and density. For 100% Indium transfer, the density should be ~1.0, for no Indium transfer (which is increasingly possible for $pH_{extraction}$~4) the water density is ~1.1.
13. Add Linear Alkylbenzene to Hexane Indium $HMVA_3$ solution.

Step V: Evaporation
13. Put the solution into a Rota vapor, pull vacuum on the solution, and allow the hexane to evaporate.
14. Once the solution becomes viscous stop rotation and keep the solution under vacuum for ~5 hours to remove any residual Heaxane.
17. Measure density of solution. For $8\%_{wt}$ Indium solution, the density should be ~0.96mg/mL

Step VI: Scintillator
18. Add Bis-MSB. Because of the small quantity, prepare beforehand a solution of PC + MSB with 1.2 mg MSB/mL solution. Typically the InLS from #18 needs about 0.25mL of this solution for InLS stock of 20mL.
19. Add ~3g/L PPO

Zheng Preliminary InPC Work						
Sample	pH	UV-Vis	S%	In% by wt	In [mol/L]	MVA per In
ZVt003	5.7	0.006	F1 41, F2 42, F3 55	7.83	0.66	3.69
ZVt001	6.6	0.01	F1 46	8.71	0.74	3.08
ZVt002	5.6	0.005	40	7.73	0.65	3.84
ZVt002-Ac	7.1	0.03	48	5.69	0.47	2.95
ZVt004-Ac	6.2	0.007	46	6.32	0.53	3.72
ZVt005-Ac	6.6	0.008	41	7.4	0.63	3.71
ZVt006-Ac	7.2	0.02	42	8.5	0.72	2.91
ZVt007-Ac	7.6	precipitate				
ZVt014-Hex-Ac	7.1	0.22		10.31	0.7	2.04
ZVt008-Hex	4	0.008		14.1	1.2	3.65
ZVt009-Hex	6.1	0.008		9.71	0.7	3
ZVt012-Hex	7.1	0.035		10.96	0.78	2.4
ZVt013-Hex	6.8			10.62	0.76	2.53
ZVt008-PC		0.01	44	4.16	0.51	3.6
ZVt009-PC		0.012	47	6.34	0.52	3.09
ZVt012-PC		0.011	49	8.21	0.69	2.67
ZVt013-PC		0.011	49	7.92	0.67	2.7
ZVt014-PC		0.015	55	8.53	0.72	2.12

Sample	pH	UV-Vis	S%	In% by wt	In [mol/L]	MVA per In
ZVt020-Hex-Ac	7.4	0.053				1.48
ZVt021-Hex-Ac	7.6	0.053				1.04
ZVt022-Hex-Ac	7.5	0.09				1.52
ZVt020-PC		0.01				1.52
ZVt021-PC		0.006				1.08
ZVt022-PC		0.006				
ZVt023-Hex-Ac	7.5					
ZVt015-Hex-Ac	7.3	0.23		10.29		1.26
ZVt016-Hex-Ac	7.3	0.04		7.07		1.16
ZVt017-Hex-Ac	7.7	Gel				
ZVt018-Hex-Ac	6.8	0.028		6.98		1.2
ZVt015-PC		0.01		58	8.85	1.33
ZVt016-PC		0.005		64	8.67	1.23
ZVt018-PC		0.004		65	8.76	1.22
ZVt019-PC		0.01		62	8.04	1.67
ZVt020-PC		0.01		63/58	8.21	1.52
ZVt021-PC		0.001		67/64		

Table 15 Zheng Preliminary InPC Work.

Zheng Great InPC						
Sample #	pH	UV-Vis	S%	In	MVA per In	S(In 8%)
ZVt012	5.6	0.005	40	7.73	3.84	40
ZVt013	5.7	0.006	41	7.83	3.69	41
ZVt012-Hex	7.1	0.011	49	8.21	2.67	46
ZVt013-HexAc	6.8	0.011	49	7.92	2.7	44
ZVt014-HexAc	7.14	0.015	55	8.53	2.12	62
ZVt016-HexAc	7.32	0.005	64	8.85	1.23	62
ZVt018-HexAc	6.84	0.0035	65	8.76	1.22	62
ZVt020-HexAc	7.39	0.01		8.21	1.52	62.5
ZVt021-HexAc	7.62	0.006	64 ?	8.21	1.08	69
ZVt015	7.29	0.01		8	1.33	58
ZVt022-HexAc	7.45	0.006	68	?	?	68

Table 16 Zheng Great InPC.

Zheng Super InPC										
Sample #	AC- (eq)	Hex (eq)	NH3 (eq)	pH	UV of Hex	UV of pc	S%	In%	[In]	MVA per In
ZVt44pc	10	40	5.1	6.88	0.017	0.004	55			
ZVt45pc	8	40	5.1	6.88	0.017	0.003	54			
ZVt38pc	12	35	5.8	6.94	0.03	0.002	64			
ZVt42pc	12	35	5.1	6.96	0.15	0.004	56			
ZVt46pc	10	40	5.4	6.98	0.019	0.004				
ZVt41pc	12	35	5.4	7.09	0.025	0.003	59			
ZVt34pc	12	35	6	7.21	0.024	0.004	60			
ZVt40pc	12	35	5.7	7.22	0.022	0.001	63			
ZVt39pc	12	35	6	7.24	0.025	0.001	66			
ZVt36pc	12	35	6	7.31	0.06	0.002	67			
ZVt29	10	30	6.3	7.57	0.024	0.003	67	7.72	0.65	1.06
ZVt27	15	32	5.75	7.65	0.025	0.004	69	8.22	0.7	1.01
ZVt28	12.5	32	6.3	7.7	0.025	0.002	66	8.07	0.68	0.99
ZVt32	13	35	6.3	7.76	0.022	0.002	70	8.87	0.75	0.85
ZVt33pc	12	35	6.1	7.76	0.023	0.008	68			
ZVt30	8.73	35	6.3	7.79	0.13	0.008	73	8.57	0.72	0.88
ZVt31	13	35	6.3	7.8	0.024	0.005	73	8.48	0.72	0.89

Table 17 Zheng Super InPC.

Rountree & Raghavan's Initial Survey of InLAB scintillator

Series #	Solvent	Scale (mM/ %In)	In % by weight	HMVA (eq)	NH_3 (eq)	AmAcet (eq)	$InCl_3$ (g)	Solvent Hexane/ LAB (g)	pH_1	pH_2	rho (kg/L)	S%	UV-Vis	UV-Vis after 3 to 4 months	Comments
RR12	LAB			3	4.5	none	22.63	102.02/ 48.80	5.34	5.34	0.955	34	0.004	0.016	
RR13	LAB			3	4.5	none	22.68	102.61/ 48.78	9.58	6.62					
RR14	LAB	50/ 12%	12	3	4.5	none	45.92	162.67/ 50.07	9.52	6.93					failed
RR15	LAB	50/ 12%	12	3	4	none	45.27	218/ 49.18	9.28	6.42	1.014	22.5			
RR16	LAB	50/ 8%	8	3	4	none	22.66	150/ 49.00	9.16	5.56	0.952	35	0.006	0.018	pH1 adjusted using HCL
RR17	LAB	50/ 8%	8	3	4	none	22.62	0/49	9.11	5.53	0.952	25.7	0.008		pH1 adjusted using HCL
RR18	LAB	50/ 8%	8		5.1	8			9.87	6					milky after Hex evap
RR19	LAB	50/ 8%	8	3	4.5	8			9.49	6.73	0.955	37	0.06		all clear
RR20	LAB	75/ 8%	8	3	4.3	8			9.38	6.45	0.95	38.5	0.008	0.02	all clear
RR21	same as 20 but without hexane---Failed														
RR22	PC	75/ 8%	8	3	4.3	8			9.48	6.59	0.934 low	55			clear / evap dry / add PC
RR23	PC	75/ 8%	8	3	4.3					6.4	0.96			0.015	all clear
RR23	LAB	75/ 8%	8	3	4.3	8				6.4	0.948	38	0.016		all clear
RR24	LAB	75/ 8%	8	3	5	8			9.65	6.99	final milky/add 1.5ml HMVA/ cleared				
RR25	LAB	75/ 8%	8	3	6.3	8			9.75	7.17	final milky/add 1.5ml HMVA/ cleared				add 3ml
RR26	LAB	100/ 8%	8	3.5	5	8			9.86	6.76	0.952	29	0.01	0.02	clean
RR26	PC	100/ 8%	8	3.5	5	8			9.86	6.76	0.944 low				

Table 18 Rountree & Raghavan's Initial Survey of InLAB Scintillator.

Bibliography

1. **Williams, W.S.C.** *Nuclear And Particle Physics.* Great Britain : The Bath Press, 2006. 0-19-852046-8.

2. Solar Physics. [Online] NASA. http://solarscience.msfc.nasa.gov/interior.shtml.

3. Sun Fact Sheet. [Online] NASA. http://nssdc.gsfc.nasa.gov/planetary/factsheet/sunfact.html.

4. *Inverse Beta decay of 115In --> 115Sn*: A New Possibility for Detecting Solar Neutrinos from the Proton-Proton Reaction.* **Raghavan, R. S.** 1976, Physical Review Letters, pp. 259-262.

5. *The Scattering of α and β Particles by Matter and the Structure of the Atom.* **Rutherford, E.** 6, s.l. : Philosophical Magazine, 1911, Vol. 21.

6. **Chadwick, James.** 383, s.l. : Verh. Deutsch. Phys. Ges., 1914, Vol. 16.

7. *ON THE RAMAN EFFECT IN DIATOMIC GASES. II.* **Rasetti, Franco.** NoRMAN BRIDGU LABORATORY, CALIFORNIA INSTITUTE oF TZCHNOLOGY : PNAS, 1929. Proceedings of the National Academy of Sciences of the United States of America. Vol. 15. 515.

8. *The idea of the neutrino.* **Brown, L. M.** s.l. : American Institute of Physics, September 1978, Physics Today.

9. *Detection of the Free Neutrino.* **Cowan, F. Reines and C. L.** s.l. : Physical Review, 1953, Vol. 92. http://link.aps.org/doi/10.1103/PhysRev.92.830.

10. *The Neutrino Nature 178, 446 (1956).* **Frederick Reines and Clyde L. Cowan, Jr.** s.l. : Nature Publishing Group, September 1, 1956, Nature, Vol. 178, pp. 446-449.

11. *The neutrino: from poltergeist to particle.* **Reines, F.** 2, s.l. : The American Physical Society, 1996, Reviews of Modern Physics, Vol. 68. http://link.aps.org/doi/10.1103/RevModPhys.68.317.

12. *The Mass-Spectra of Chemical Elements.* **Aston, Francis.** s.l. : Philosophical Magazine and Journal of Science, 1920, Vol. 39, pp. 611-625.

13. **Bahcall, John.** How The Sun Shines. *NobelPrize.org.* [Online] June 29, 2000. http://nobelprize.org/nobel_prizes/physics/articles/fusion/index.html.

14. *Energy production in Stars.* **Bethe, H.A.** s.l. : Physical Review, 1939, Vol. 55.

15. *NEW SOLAR OPACITIES, ABUNDANCES, HELIOSEISMOLOGY, AND NEUTRINO FLUXES.* **John N. Bahcall, Aldo M. Serenelli, and Sarbani Basu.** L85-L88, s.l. : The Astrophysical Journal, 2005, Vol. 621. astroph/0412440, http://iopscience.iop.org/1538-4357/621/1/L85/pdf/1538-4357_621_1_L85.pdf.

16. *Chalk River Laboratory Report PD-205.* **Pontecorvo, Bruno.** s.l. : (unpublished), 1948.

17. *Search For Neutrinos From The Sun.* **Raymond Davis, Jr., Don S. Harmer, and Kenneth C. Hoffman.** 21, s.l. : Physical Review Letters, April 16, 1968, Vol. 20.

18. *Present Status Of The Theoretical Predictions For The 37Ar Solar-Neutrino Experiment.* **J.N. Bahcall, N.A. Bahcall, and Giora Shaviv.** 21, s.l. : Physical Review Letters, May 20, 1968, Vol. 20.

19. Neutrino Oscillation. *Wikipedia.* [Online] http://en.wikipedia.org/wiki/Neutrino_oscillation.

20. *Measurement of the Rate of ve+d→p+p+e- Interactions Produced by 8B Solar Neutrinos at the Sudbury Neutrino Observatory.* **Ahmad, Q.R. et al. (SNO Collaboration).** 7, s.l. : Physical Review Letters, July 25, 2001, Vol. 87.

21. *A simple Parameterization of Matter Effects on Neutrino Oscillations.* **M. Honda, et al.** s.l. : arXiv, Feb 13, 2006. http://arxiv.org/PS_cache/hep-ph/pdf/0602/0602115v1.pdf.

22. **al., S. Eidelman et.** Chapter 15: Neutrino mass mixing, and flavor. *Physics Letters B.* 2004, Vol. 592.

23. *Update of the solar neutrino oscillation analysis with the 766 Ty KamLAND spectrum.* **Abhijit Bandyopadhyay, Sandhya Choubey, Srubabati Goswami, S.T. Petcov, and D.P. Roy.** 1-2, s.l. : Physics Letters B, 2005, Vol. 608.

24. *Evidence for an Oscillatory Signature in Atmospheric Neutrino Oscillations.* **Collaboration), Y. Ashie et al. (The Super-Kamiokande.** 10, s.l. : Physical Review Letters, 2004, Vol. 93.

25. *Number of Neutrino Types and Sum of Neutrino Masses.* **Karlen, D.** 1-4, s.l. : Physics Letters B, 2004, Lepton Partical Listings, Vol. 592, p. 445.

26. *The Liquid Scintillator Neutrino Detector and LAMPF Neutrino Source.* **C. Athanassopoulos, et al.** 1-2, s.l. : Elsevier Science B.V. , 1997, Nuclear Instruments & Methods In Physics Research Section A, Vol. 388.

27. *A Search for Electron Neutrino Appearance at the Δm2 ~ 1 eV2 Scale.* **Collaboration, A.A. Auilar-Arevalo et al. MiniBooNE.** 23, s.l. : Physical Review Letters, 2007, Vol. 98.

28. Bugey. [Online] http://www.nu.to.infn.it/exp/all/bugey/.

29. *Active-sterile neutrino transformation solution for r-process nucleosynthesis.* **G.C. McLaughlin, J.M. Fetter, A.B. Balantekin, and G.M Fuller.** 5, s.l. : Physics Review C, May 1999, Vol. 59.

30. *Probing Active to Sterile Neutrino Oscillations in the LENS Detector.* **Christian Grieb, Jonathan Link, R. S. Raghavan.** arXiv:hep-ph/0611178v3.

31. *The luminosity constraint on solar neutrino fluxes.* **Bahcall, John N.** 2, s.l. : Physical Review C., Febuary 2002, Vol. 65. 025801.

32. **Carlos Pena-Garay, Aldo Serenelli.** *Solar neutrinos and the solar composition problem.* s.l. : arxiv.org, 2008. arXiv:0811.2424v1.

33. *Direct measurement of the Be-7 solar neutrino flux with 192 days of Borexino data.* **Arpesella, C et al. (Borexino Collaboration).** 9, s.l. : Physical Review Letters, August 29, 2008, Vol. 101. 091302.

34. *Smallest Known Q Value of Any Nuclear Decay: The Rare β- Decay of 115In(9/2+)◊115Sn(3/2+).* **J. S. E. Wieslander, J. Suhonen, T. Eronen, M. Hult, V.-V. Elomaa, A. Jokinen, G. Marissens, M. Misiaszek, M. T. Mustonen, S. Rahaman, C. Weber, and J. A¨ ysto.** s.l. : Physical Review Letters, 2009, Vol. 103. 122501.

35. *Q Value of 115In◊115Sn(3/2+): The Lowest Known Energy beta-Decay.* **Brianna J. Mount, Matthew Redshaw, and Edmund G. Myers.** s.l. : Physical Review Letters, 2009, Vol. 103. 122502.

36. *Solar-Neutrino Detection: Experimental Determination of Gamow-Teller Strengths via the 98Mo and 115In (p, n) Reactions.* **al, J. Rapaport et.** 21, s.l. : Physical Review Letters, May 27, 1985, Vol. 54, pp. 2325-2328.

37. *LENS as a Probe of Sterile Neutrino Mediated Oscillations.* **C. Grieb, J. M. Link, M. L. Pitt, R. S. Raghavan, D. Rountree, R. B. Vogelaar.** s.l. : arXiv.org, 2007. arXiv:0705.2769v1.

38. *The luminosity constraint on solar neutrino fluxes.* **Bahcall, J. N.** 2, s.l. : Physical Review C, January 9, 2002, Vol. 65, pp. 025801 p1-5. http://link.aps.org/doi/10.1103/PhysRevC.65.025801. 0556-2813.

39. *On the photon diffusion time scale for the sun.* **Mitalas, R. and Sills, K.** s.l. : The Astrophysical Journal, 1992, Vol. 401.

40. Sun-Earth Day. [Online] Nasa, 2007. http://sunearthday.nasa.gov/2007/locations/ttt_sunlight.php.

41. *Dark energy from mass varying.* **Rob Fardon, Ann E Nelson, and Neal Weiner.** s.l. : Journal of Cosmology and Astroparticle Physics, 2004. http://stacks.iop.org/1475-7516/2004/i=10/a=005.

42. *Mass varying neutrinos in the Sun.* **Cirelli M, Gonzalez-Garcia MC, Pena-Garay C.** 1-2, s.l. : NUCLEAR PHYSICS B, July 18, 2005, Vol. 719, pp. 219-233.

43. *Solar mass-varying neutrino oscillations.* **Barger V, Huber P, Marfatia D.** 21, s.l. : PHYSICAL REVIEW LETTERS, November 18, 2005, Vol. 95. 211802.

44. *Precision study of ground state capture in the N-14(p, gamma)O-15 reaction.* **Marta, M. et al. (for the LUNA Collaboration).** 2, s.l. : PHYSICAL REVIEW C, August 2008, Vol. 78. 022802.

45. *Standard Solar Composition.* **Sauval, N. Grevesse and A.J.** s.l. : Journal Space Science Reviews, May 1998, Vol. 85, pp. 161-174.

46. **Asplund M, Grevesse N, Sauval AJ.** The solar chemical composition. *ASTRONOMICAL SOCIETY OF THE PACIFIC CONFERENCE SERIES.* SAN FRANCISCO : ASTRONOMICAL SOC PACIFIC, 2005, Vol. 336, pp. 25-38.

47. *Helioseismological implications of recent solar abundance determinations.* **Bahcall JN, Basu S, Pinsonneault M, Serenelli AM.** 2, s.l. : ASTROPHYSICAL JOURNAL, January 10, 2005, Vol. 618, pp. 1049-1056.

48. **W. C. Haxton, A. M. Serenelli.** *CN-Cycle Solar Neutrinos and Sun's Primordial Core Metalicity.* s.l. : arxiv.org, May 14, 2008. arXiv:0805.2013v1.

49. **Chen, Marl.** SNO+: SNO with Liquid Scintillator. [Online] http://www.int.washington.edu/talks/WorkShops/dusel_wkshp/People/Chen_M/Chen_DUL.pdf.

50. *Present Status of KamLAND.* **Collaboration), Suzuki A (KamLAND.** s.l. : Nuclear Physics B, 1999, Vol. 77.
51. *INDIUM-LOADED LIQUID SCINTILLATOR FOR LOW-ENERGY SOLAR-NEUTRINO SPECTROSCOPY.* **PFEIFFER L, MILLS AP, RAGHAVAN RS, CHANDROSS EA.** 1, s.l. : PHYSICAL REVIEW LETTERS, 1978 , Vol. 41, pp. 63-66.
52. Thete13 Daya Bay. [Online] http://dayawane.ihep.ac.cn/twiki/bin/view/Public/.
53. *The Palo Verde reactor neutrino experiment - A test for long baseline neutrino oscillations.* **al, Boehm F et.** s.l. : Progress in Particle and Nuclear Physics, 1998, Vol. 40.
54. Double CHOOZ. [Online] http://doublechooz.in2p3.fr/Status_and_News/status_and_news.php.
55. **Chandross, Edwin Arthur (Murray Hill, NJ), Raghavan and Ramaswamy Srinivasa (Berkeley Heights, NJ).** *Method of solvating a metal in an aromatic organic liquid . 6,809,210* USA, October 26, 2004 .
56. —. *Compositions comprising a solvated metal. 7,332,627* USA, February 19, 2008.
57. *pp-Solar Neutrino Spectroscopy: Return of the Indium Detector .* **Raghavan, R.S.** 2001. arXiv:hep-ex/0106054v1.
58. *LENS Indium-loaded Liquid Scintillator for Solar Neutrino Spectroscopy.* **Chang, Z et. al. (LENS Chemistry Group).** 2006. Neutrino 2006 Poster Session.
59. *Gadolinium-loaded liquid scintillator for high-precision measurements of antineutrino oscillations and the mixing angle theta13.* **M. Yeh, A. Garnov, R. L. Hahn.** s.l. : Nuclear Instuments and Methods in Physics Research, 2007, Vol. 578.
60. *Experimental scintillator purification tests with silica gel chromatography.* **Niedermeier L, Grieb C, Oberauer L, Korschinek G, von Fellitzsch F.** 2, s.l. : NUCLEAR INSTRUMENTS & METHODS IN PHYSICS RESEARCH SECTION A-ACCELERATORS SPECTROMETERS DETECTORS AND ASSOCIATED EQUIPMENT, 2006, Vol. 258.
61. *Study of phenylxylylethane (PXE) as scintillator for low energy neutrino experiments.* **Back, H.O. et al (Borexino Collaboration).** s.l. : Elsevier, 2008, Nuclear Instruments & Methods In Physics Research A, Vol. 585, pp. 48-60.

62. **C. Kraus, SNO+ Collaboration, et al.** *PROGRESS IN PARTICLE AND NUCLEAR PHYSICS.* 2006. pp. 150-152. Vol. 57.

63. *SNO with liquid scintillator: SNO+.* **C. Kraus, for the SNO+ collaboration.** s.l. : Progress in Particle and Nuclear Physics, 2006, Vol. 57, pp. 150-152.

64. **S.D. Rountree, R.S.Raghavan, Y. MinFang, L. Hu.** LENS Scintillation Group Meeting at BNL. March 2010.

65. **Ridley, Jason.** Improvement of the Optical and Mechanical Properties of Silica Nanoparticle Ionic Self-Assembled Multilayer Anti-Reflection Coatings on Glass and Polycarbonate Substrates. *VT Dissertation.* s.l. : Virginia Tech, 2010.

66. *Work on Indium Backgounds in LENS.* **Raghavan, C. and R.S.** 2005.

67. **Vogelaar, Robert Bruce.** Kimballton Underground Research Facility. [Online] http://www.phys.vt.edu/~kimballton/.

68. Chemical Lime. [Online] http://www.chemicallime.com/Frame_Home.htm.

69. DUSEL. [Online] http://www.dusel.org/.

70. **Doss, Catherine.** *Science experiments will go forward at Kimballton mine.* Blacksburg, Va : s.n., July 28, 2005. Virginia Tech News. http://www.phys.vt.edu/news/dusel072805.html.

71. *Double-electron capture on Sn-112 to the excited 1871 keV state in Cd-112: A possible alternative to double-beta decay.* **Kidd MF, Esterline JH, Tornow W.** 3, s.l. : PHYSICAL REVIEW C, 2008, Vol. 78.

72. *New results for double-beta decay of Mo-100 to excited final states of Ru-100 using the TUNL-ITEP apparatus.* **Kidd MF, Esterline JH, Tornow W et. al.** s.l. : NUCLEAR PHYSICS A, 2009, Vol. 821, pp. 251-261.

73. Low Background Physics at the Kimballton Underground Research Facility (KURF). [Online] http://www.physics.unc.edu/research/nuclear/particle_astro/kimballton.php.

74. *Collaborative Research: Mini-LENS-- OPERATION OF A PROTOTYPE LOW-ENERGY SOLAR NEUTRINO SPECTROMETER UNDERGROUND.* **R.S. Raghavan, J. Blackmon, M. Yeh and the LENS Collaboration.** s.l. : NSF Fall 2009 proposal, 2009.

75. **G. Alimonti, et al.** The Borexino detector at the Laboratori Nazionali del Gran Sasso, arXiv:0806.2400v1. *www.arxiv.org.* [Online] June 6, 2008.

76. **Raghavan, R.S.** *480nm bump in InLAB.* [interv.] S.D. Rountree. 2007.

77. *A Suggestion on the Detection of the Neutrino.* **Wang, Kan Chang.** 1-2, s.l. : The American Physical Society, 1942, Vol. 61. DOI:10.1103/PhysRev.61.97.
78. *Kimballton Underground Research Facility (poster).* **Vogelaar, R. Bruce.**